

# 博士学位論文

論文題目 Articulated Tube Mechanism to Enable

Variable Stiffness by Positive-Pressurization

---

---

提出者 東北大学大学院情報科学研究科

応用情報科学専攻

学籍番号 C1ID4003

氏名 恩田 一生

TOHOKU UNIVERSITY

Graduate School of Information Sciences

Articulated Tube Mechanism to Enable Variable Stiffness  
by Positive-Pressurization

(—加圧により柔剛切替を可能とする多関節線状メカニズムに関する研究—)

A dissertation submitted for the degree of Doctor of Philosophy  
(Information Science)

Department of Applied Information Sciences

by

Issei Onda

January 9, 2024

# Articulated Tube Mechanism to Enable Variable Stiffness by Positive-Pressurization

Issei Onda

## Abstract

This study embarks on the development of a novel variable stiffness mechanism for addressing a pivotal challenge in soft robotics. Such mechanisms, crucial in replicating the flexibility and adaptability of living organisms, allow robots to transition between states of varying stiffness. This capability is vital in tasks requiring stability, and adaptability, particularly in the disaster field and medical applications.

Soft robotics, the field at the core of this research, focuses on robots made from flexible materials, such as elastomers and compliant polymers. The defining characteristic of soft robots is their ability to mimic biological systems, offering high degrees of freedom and safe interaction with humans and delicate objects. These robots excel in unstructured environments, adapting their shape and movements to complex and unpredictable surroundings. However, their inherent flexibility often leads to challenges in maintaining stability and bearing loads, which is a significant drawback, particularly in applications requiring precise control.

The introduction of variable stiffness mechanisms offers a promising solution to these challenges. By enabling soft robots to alter their stiffness on demand, these mechanisms provide the necessary stability and load-bearing capacity without sacrificing the inherent advantages of soft robotics. This approach allows to maintain flexibility and adaptability when needed, and to become rigid for tasks requiring precision and load support. It bridges the gap between the flexibility of soft robotics and the stability and control traditionally found in rigid robotics.

In the field of variable stiffness mechanisms, conventional research has focused on two primary methodologies. The first involves controlling deformation through opposing rigid components, which can be further classified into mechanical and friction-based methods. The second approach deals with modulating the rigidity of the components themselves, known as the material method.

Mechanical and friction-based methods are generally driven by either electric or fluidic actuators. Mechanical methods leverage geometric constraints and include designs such as latches, ratchets, dog clutches, cam-based mechanisms, and hydraulic locks. These are advantageous for their high locking force and lower operational energy, but are constrained by their discrete locking positions and limited force adjustability. Friction methods, conversely, encompass electromagnetic locks, piezoelectric locks, statically balanced locks, overrunning locks, nonbackdrivable gears, self-amplifying locks, capstans, and various particle, layer, or segment-based locks. While offering continuous locking positions and adjustable locking force, these methods usually provide a lower locking force and demand higher energy consumption compared to mechanical methods.

The material method in variable stiffness involves altering the physical properties of the materials used, utilizing techniques such as phase change, glass transition, functional fluid approaches, area's moment of inertia. In these approaches, to alter the rigidity of the components

themselves, it is necessary to modify the stimuli based on the physical properties of the materials used.

This research adopts a novel approach, employing a variable stiffness mechanism that alternates between flexible and high-stiffness states using positive pressure through friction and air. This design aims to achieve high locking force, adjustability, and a wide range of deformation, suitable for collaborative tasks in sensitive environments.

The proposed structure transforms the expansion force during pressurization into a friction-based locking force, effectively controlling the expansion deformation of a pressurized chamber. This design involves placing components strategically to limit expansion deformation, particularly of rubber tubes, and employing these components to generate locking force upon expansion. The research includes a comprehensive evaluation of the locking force for both radially expandable and axial contraction types of the mechanism through theoretical modeling, finite element analysis, and empirical measurements.

The study is detailed across several chapters:

In Chapter II, the study explores a radially expandable type mechanism featuring ball-type joints combined with rubber tubes. The focus here is on the ease of assembly, preventing dislocation during pressurization, and achieving joint holding torque through friction. Experiments were conducted to assess the holding torque of this mechanism, using theoretical modeling, finite element analysis, and empirical measurements. The results indicated a consistent performance within a 30% margin of error between theoretical and empirical values.

Chapter III evaluates a radially expandable type mechanism, merging ball joints and rubber tubes with a lever for clamping a wire. This chapter assesses the locking performance theoretically and empirically, with a particular emphasis on the anisotropy of the holding torque attributed to wire arrangement. Comparative analyses of the holding torque with and without the lever were performed, demonstrating that the friction-based holding torque between the ball joints and the lever-wire system aligns within a 20% margin of error between theoretical and empirical values.

Chapter IV delves into an axially contraction type mechanism combining bowl-type joints with McKibben-type artificial rubber muscles. The chapter quantitatively evaluates the shape-locking and shape-restoration performances. The holding torque evaluation, based on theoretical models and empirical measurements, showed a discrepancy within a 20% margin of error. Additionally, the recoverable angles under varied pressurization flow rates were measured, confirming the feasibility of controlling the restoration angle through flow rate adjustments.

The study further extends to the application of these mechanisms in a snake-like robot for alternately propulsion in confined spaces. This robot, leveraging the radially expandable type mechanism, demonstrates the advantages of alternately propulsion, which minimizes friction and enables efficient navigation in tight environments. The propulsion procedure involves alternating stiffening and flexing of the robot segments, allowing it to navigate by pushing. The prototype's design, featuring a hollow multi-layered structure, optimizes this alternate propulsion method, showcasing its practical utility in experimental setups.

This study presents a significant advancement in soft robotics by introducing a variable stiffness mechanism that is highly scalable, adaptable, and capable of high locking force. The mechanism's potential in enhancing soft robot capabilities in diverse applications, particularly in medical and caregiving settings, is evident, marking a promising direction for future innovations in the field.

# TABLE OF CONTENTS

<b>CHAPTER I INTRODUCTION .....</b>	<b>2</b>
<b>Section I.1 Research background of variable stiffness mechanism in soft robotics. 2</b>	
<b>Section I.2 Previous research of variable stiffness mechanism. ....</b>	<b>4</b>
Subsection I.2.1 Previous methods to switch between flexible and high stiffness modes by arranging components opposite each other. ....	4
Subsection I.2.2 Previous methods to switch between flexible and high stiffness modes by adjusting the stiffness of components. ....	11
Subsection I.2.3 Comparison of locking methods between arranging components in an opposite manner and adjusting the stiffness based on performance. ....	14
<b>Section I.3 Proposed principle: variable stiffness mechanism structured with oppositely arranged components, controlling locking via friction and positive-pressure. 16</b>	
<b>Section I.4 Research purpose of this study. ....</b>	<b>16</b>
<b>Section I.5 Structure of the thesis. ....</b>	<b>21</b>
<b>CHAPTER II TUBE MECHANISM WITH 3-AXIS ROTARY JOINTS STRUCTURE TO ACHIEVE VARIABLE STIFFNESS USING POSITIVE PRESSURE. ....</b>	<b>26</b>
<b>Section II.1 Abstract of Chapter II. ....</b>	<b>26</b>
<b>Section II.2 The basic principle of the proposed variable stiffness mechanism with single rubber tube and 3-axis rotary ball joints. ....</b>	<b>27</b>
Subsection II.2.1 The design method of pressure driven variable stiffness mechanism. ....	27
Subsection II.2.2 Theoretical model of the expandable hemisphere that can be fitted to the shell. 29	
Subsection II.2.3 Theoretical model of expandable hemisphere that does not dislocate from the shell when pressurized. ....	33
Subsection II.2.4 Theoretical model of holding torque in the pitch and roll directions. ....	34
<b>Section II.3 Mechanism design of the proposed variable stiffness mechanism with single rubber tube and 3-axis rotary ball joints. ....</b>	<b>36</b>
Subsection II.3.1 Design method of 3-axis rotary ball joint. ....	36

Subsection II.3.2	Design method of the prototype of the proposed mechanism.....	37
<b>Section II.4</b>	<b>Simulation and experiment of the proposed variable stiffness mechanism with single rubber tube and 3-axis rotary ball joints. ....</b>	<b>39</b>
Subsection II.4.1	Simulation of holding torque using finite element analysis.....	39
Subsection II.4.2	Measuring the holding torque in the pitch and roll directions.....	41
<b>Section II.5</b>	<b>Discussion of Chapter II.....</b>	<b>44</b>
<b>Section II.6</b>	<b>Conclusion of Chapter II. ....</b>	<b>45</b>
<b>CHAPTER III</b>	<b>TUBE MECHANISM TO ACHIEVE POSITIVE-PRESSURIZATION VARIABLE STIFFNESS MECHANISM BY LEVER AND WIRE.....</b>	<b>47</b>
<b>Section III.1</b>	<b>Abstract of Chapter III.....</b>	<b>47</b>
<b>Section III.2</b>	<b>Basic principle of variable stiffness mechanism by leverage through positive-pressurization.....</b>	<b>48</b>
Subsection III.2.1	Ball joint and rubber tube with lever and wire.....	48
Subsection III.2.2	Theoretical model of holding torque by frictional force between lever and wires, between ball joints. ....	52
Subsection III.2.3	Bending angle of the ball joints and shell scale for preventing joint dislocation. 55	
<b>Section III.3</b>	<b>Mechanical design of variable stiffness mechanism by leverage through positive-pressurization.....</b>	<b>56</b>
Subsection III.3.1	Design method of the ball joint and lever for measuring the holding torque.	56
Subsection III.3.2	Assembly method of the prototype. ....	58
<b>Section III.4</b>	<b>Experiment of variable stiffness mechanism by leverage through positive-pressurization.....</b>	<b>59</b>
Subsection III.4.1	Measurement of the cramping force and calculation of the coefficient static friction between wires and levers. ....	59
Subsection III.4.2	Measurement of the holding torque in the pitch direction with and without wires. 62	
<b>Section III.5</b>	<b>Discussion of Chapter III. ....</b>	<b>66</b>
<b>Section III.6</b>	<b>Conclusion of Chapter III.....</b>	<b>67</b>

<b>CHAPTER IV ARTICULATED TUBE MECHANISM WITH VARIABLE STIFFNESS AND SHAPE RESTORATION USING A PNEUMATIC ACTUATOR .....</b>	<b>70</b>
<b>Section IV.1 Abstract of Chapter IV.....</b>	<b>70</b>
<b>Section IV.2 Basic principle of variable stiffness and shape restoration. ....</b>	<b>71</b>
Subsection IV.2.1 Driven method by McKibben pneumatic artificial muscles. ....	71
Subsection IV.2.2 Theoretical model of holding torque in the pitch direction. ....	73
<b>Section IV.3 Mechanism design of prototype.....</b>	<b>75</b>
<b>Section IV.4 Experiment for evaluating the performance of prototype. ....</b>	<b>78</b>
Subsection IV.4.1 Measurement of holding torque in the pitch direction. ....	78
Subsection IV.4.2 Measurement of the restoring angle and force using the pneumatic artificial muscle.	83
<b>Section IV.5 Discussion of Chapter IV. ....</b>	<b>87</b>
<b>Section IV.6 Conclusion of Chapter IV.....</b>	<b>88</b>
<b>CHAPTER V PNEUMATIC DRIVEN HOLLOW VARIABLE STIFFNESS MECHANISM AIMING ALTERNATELY INSERTION OF TELESCOPIC GUIDE TUBES.....</b>	<b>91</b>
<b>Section V.1 Abstract of Chapter V.....</b>	<b>91</b>
<b>Section V.2 Application examples of snake-like robots with the variable stiffness mechanism using positive pressure. ....</b>	<b>93</b>
<b>Section V.3 Basic principle of propulsion method with the variable stiffness mechanism.</b>	<b>96</b>
<b>Section V.4 Mechanical design of prototype with the variable stiffness mechanism using positive pressure.....</b>	<b>98</b>
<b>Section V.5 Experiment for evaluating of basic principle.....</b>	<b>101</b>
Subsection V.5.1 Required pulling force to insert the tube in the other bent tube.....	101
Subsection V.5.2 Test on a Curved Narrow Environment. ....	105
<b>Section V.6 Discussion of Chapter V.....</b>	<b>107</b>
<b>Section V.7 Conclusion of Chapter V. ....</b>	<b>108</b>

CHAPTER VI CONCLUSION AND FUTURE ASPECTS .....	110
Section VI.1 Overall discussions of proposed mechanism about the holding torque via theoretical comparison. ....	110
Section VI.2 Comparison of the previous and proposed methods in terms of the ratio between maximum and minimum stiffness.....	113
Section VI.3 Conclusion of the thesis.....	114
Section VI.4 Future aspects. ....	116
ACKNOWLEDGEMENT.....	I
REFERENCES .....	II
RESEARCH ACHIEVEMENTS.....	XII
LIST OF PUBLICATIONS.....	XV



## LIST OF FIGURES

Fig. 1 Behavior of the robotic gripper in flexible and high stiffness modes: In the flexible mode, the gripper deforms to transfer to the shape of the object. In the high stiffness mode, it maintains the shape of the object while being grasped..... 3

Fig. 2 Methods to switch between flexible and high stiffness modes: (a) By arranging components opposite each other. (b) By adjusting the stiffness of components.  $EI$  is flexural rigidity..... 4

Fig. 3 Types of mechanical locking methods with (a) latch with one locking position, (b) latch with multiple locking positions, (c) ratchet, (d) dog clutch, (e) cam-based with cam follower, (f) cam-based with mutilated gears, (g) cam-based with geneva and (h) hydraulic lock. .... 5

Fig. 4 Types of friction-based locking devices with (a) an electromagnetic brake, (b) a piezo-actuated brake, (c) a statically balanced brake, (d) an overrunning clutch, (e) a nonbackdrivable gear, (f) a self-engaging brake, (g) a self-engaging pinion-gear mechanism, (h) a capstan, (i) particles ,(j) layers and (k) segments... 6

Fig. 5 Operation of the energy transfer ratchet mechanism in the prosthetic knee [26]. .... 8

Fig. 6 Split collars for mechanical locking using a dog clutch [28]. .... 8

Fig. 7 Clutchable series-elastic actuator knee using electromagnetic brake [42]. 8

Fig. 8 Articulated robotic probe with frictional locking mechanism by pulling wire using motor [83]. .... 9

Fig. 9 Design of shape-lockers and distal disks using piezo wire clamp mechanism by friction [47]. .... 9

Fig. 10 Rigid-flexible outer sheath model with mechanical locking by the gear rack of the slider and air pressure [22]. .... 10

Fig. 11 Tool holding articulated arm with frictional locking using air cylinder [86].  
..... 10

Fig. 12 Pressure-driven manipulator becomes high stiffness owing to the friction between the rubber chamber and rigid walls [87]. .... 10

Fig. 13 Soft robotic spine with tunable stiffness based on joint and particle jamming [70]. .... 11

Fig. 14 Tubular snake-like manipulator prototype with tunable stiffness based on

layer jamming [78].	11
Fig. 15 Material locking mechanism with low melting point alloys [90] / polymers [96]. Stiffness is changed by thermal stimulation.	13
Fig. 16 Material locking mechanism with shape memory alloys [98] / polymers [104]. Stiffness is changed by thermal stimulation.	13
Fig. 17 Magnetorheological [107] and electrorheological [110] variable stiffness mechanism.	13
Fig. 18 Variable stiffness mechanism through the alteration of the area's moment of inertia. (i) Cross-section type[112] and (ii) Structural interactions change type[142].	14
Fig. 19 Classification of variable stiffness mechanism by friction using pneumatic pressure. They can be roughly classified into two groups negative-pressure and positive-pressure methods. The common points are that the variable stiffness function is maintained by changing the structure and arrangement of the chamber and components.	18
Fig. 20 Method of forming multi-joint structures using spherical surface joints and rubber tubes. The arrangement of these joints is categorized into two types: an interlinked structure where the joints are physically connected, and a partitioned structure where the joints are physically separated. The vertical entries represent the direction of the force as radial and axial, while the horizontal entries classify the direction of force as positive (expansive) and negative (contractive).	19
Fig. 21 Comparison of the previous methods in terms of the ratio between maximum and minimum stiffness.	21
Fig. 22 Structure of this thesis.	24
Fig. 23 Prototype of the proposed mechanism and prototype specifications. The joints and levers are made of acrylic resin and are manufactured using a 3D printer (AGILISTA, Keyence, Japan).	26
Fig. 24 3-axis rotary ball joint with slits design of the proposed method.	28
Fig. 25 Principle of the proposed method for variable stiffness. The radial expandable hemispheres don't contact to shell when no pressure. The expandable hemisphere is deformed by pressurizing the enclosed rubber tube, and contact pressure is obtained between the expandable hemisphere and shell.	29
Fig. 26 Fitting of expandable hemisphere on shell.	30

Fig. 27 Stepped cantilever under concentrated load. ....	30
Fig. 28 Moment of inertia of area $I_2$ .....	30
Fig. 29 Moment of inertia of area $I_1$ .....	31
Fig. 30 Expansion force at the contact point A'.....	34
Fig. 31 Normal force on differential area of joint shell. ....	35
Fig. 32 Parts and assembly of prototype for the proposed method. (a) 3-axis rotary ball joint based on Subsection II.3.1 and Table I. (b) Rubber tube is made of Ecoflex 00-50. (c)-(d) Air plugs for gluing the ends of the rubber tube. (e) Experimental unit for evaluating whether the expandable hemisphere fits into the shell, whether the expandable hemisphere dislocates from the shell during pressurization, and the joint holding torque. (f) Assembly method of the experimental unit. ....	38
Fig. 33 3D experimental setup in FEM simulations for evaluating the holding torque. To obtain holding torque in pitch direction, rotate female joint around the CP in the $x$ -axis. To output holding torque in the roll direction, rotate female joint around the CP in $y$ -axis.....	40
Fig. 34 Experimental setup for measuring the holding torque in the pitch direction. This setup offset the moments due to the weight of the arm from the measured value. Holder and connector are made of resin containing glass (Rigid 10K) and are manufactured using stereolithography (Formlabs, Form 3, USA).....	42
Fig. 35 Experimental setup for measuring the holding torque in the roll direction. Wire connector is made of machined duralumin (A2017). ....	42
Fig. 36 Results of theoretical, FEM and measured values of holding torque in pitch and roll directions. The error bar indicates the standard deviation of the measured value. ....	43
Fig. 37 (a) Prototype of the proposed mechanism and cross-sectional view of levers and wires. (b) Wires are cramped by rotated lever when positive pressure is applied. The joints and levers are made of acrylic resin and are manufactured using a 3D printer (AGILISTA, Keyence, Japan). The wires are made of stainless steel (SC-75, Osaka Coat Rope, Japan).....	48
Fig. 38 Assembled all components of the proposed mechanism.....	49
Fig. 39 Design of the male ball joint of the proposed method. ....	50
Fig. 40 Design of the female ball joint of the proposed method. ....	50
Fig. 41 Arrangement of the lever and wire on the ball joint. ....	51

Fig. 42 Principle of the proposed method for variable stiffness. The wires are cramped by rotated lever when positive pressure is applied. ....	52
Fig. 43 Theoretical model of holding torque with four levers when the positive pressure is applied. ....	53
Fig. 44 Holding torque due to the extension force applied to the contact surface of the segment by the rubber tube. ....	53
Fig. 45 Shell scale and ball joint bending angle, which are crucial for preventing joint dislocation. ....	55
Fig. 46 Male and female joints of the proposed mechanism. The diameter of these joints is 40 mm. The inner radius of joints is 8.0 mm. ....	56
Fig. 47 Levers for wire cramping. The outer radius of the spherical surface where the lever contacts the rubber tube is 7.0 mm. ....	56
Fig. 48 Rubber tube and plugs of the proposed mechanism. ....	57
Fig. 49 Components and assembly of prototype for the proposed method. ....	58
Fig. 50 Experimental setup for measuring the clamping force under positive pressurization. The holder and arm are made of resin containing glass (Rigid 10K) and are manufactured using stereolithography (Formlabs, Form 3, United States). ....	60
Fig. 51 Raw data of the last measured cramping force at each internal pressure. The first peak of the measured tensile force is the maximum static frictional force. ....	60
Fig. 52 Raw data of the last measured cramping force at each internal pressure. ....	61
Fig. 53 Experimental setup for measuring the holding torque in the bending direction. This setup offset the moments due to the weight of the arm from the measured value. The holder and connector are made of resin containing glass (Rigid 10K) and are manufactured using stereolithography (Formlabs, Form 3, United States). ....	63
Fig. 54 Raw data of the last measured pulling forces with the wire in the bending direction and the pulling force without the wire when 0.2 MPa was applied. The frictional force at the circle point is the maximum static friction force for calculating the holding torque under each condition. ....	64
Fig. 55 Results of the theoretical and the measured values of holding torque in the	

bending directions. The error bar indicates the standard deviation of the measured value. This graph validates that the holding torque increases with the presence of wires at each internal pressure. ....	65
Fig. 56 Prototype of the proposed variable stiffness mechanism consisting of a pneumatic artificial muscle enclosed in a link structure. ....	71
Fig. 57 Classification of friction-based variable stiffness mechanisms: (a) Wire method in the axial direction. (b) Positive-pressurization method in radial direction. (c) Positive-pressurization method in axial direction. ....	72
Fig. 58 Principle of pneumatic artificial muscles. ....	72
Fig. 59 Internal workings of the proposed mechanisms. ....	72
Fig. 60 Holding torque due to the contraction force applied to the contact surface of the segment by the pneumatic artificial muscle. ....	75
Fig. 61 Prototype of the proposed method. (a) Assembly method of the linear structure. (b) Fabricated hollow segment. (c) Maximum radius of the curvature of the prototype. ....	76
Fig. 62 Results of the shape-restoring actuation when the flow rate is increased using the prototype. ....	77
Fig. 63 Results of the shape-restoring actuation when the flow rate is reduced using the prototype. ....	77
Fig. 64 Experimental device for measuring holding torque in the pitch direction. (a) Experimental setup. (b) Method of measurement for holding torque. (c) Experimental setup about segment. (d) Pneumatic artificial muscle. (e) Split collar for adjusting inner segment diameter. ....	79
Fig. 65 Cross-sectional view of the experimental device for measuring holding torque in the pitch direction. ....	80
Fig. 66 Comparison of the theoretical and measured values of holding torque in the pitch direction. The error bar indicates the maximum and minimum of the measured values, and the average of five trials is shown. ....	81
Fig. 67 Results of the measured values of contraction force. The error bar indicates the maximum and minimum of the measured values, and the average of five trials is shown. ....	82
Fig. 68 Experimental device for measuring the restoration angle and force using the pneumatic artificial muscle. ....	84

Fig. 69 Shape-restoring actuation. Here, $\theta$ is the restoring angle, which is defined from the rotation central axis to the position the arm moved by pressurization. (a) The restoring angle decreased when the valve opening is increased. (b) The restoring angle increased when the valve opening is decreased.....	85
Fig. 70 Results of the measured values of restoring angle $\theta$ .....	86
Fig. 71 Results of the measured values of restoring force.....	86
Fig. 72 Applications of the proposed variable stiffness mechanism via friction and positive-pressurization.....	92
Fig. 73 Previous snake-like robots have been proposed with the aim of propelling through the rubble, such as the wheeled [123], the continuous track [125], modular robots [127] and the vibrating cilia [128].....	94
Fig. 74 Semicircular duplex manipulator.....	95
Fig. 75 Pre-bent telescopic tube.....	96
Fig. 76 Robotic catheter navigation.....	96
Fig. 77 Basic configuration of the proposed robot.....	98
Fig. 78 Steps for sliding motion.....	98
Fig. 79 Cross-sectional view and air infiltration path of the prototype internal/external slider. ....	99
Fig. 80 Cross-sectional model of the tip-side end. ....	100
Fig. 81 Cross-sectional model of the root-side end. ....	100
Fig. 82 Joint and cap used in the active curved part of the inner tube. ....	101
Fig. 83 Experimental device when the inner tube is in a flexible state and the outer tube is in a highly rigid state.....	103
Fig. 84 Experimental device when the outer tube is in a flexible state and the inner tube is in a highly rigid state.....	103
Fig. 85 The guide rail of each radius of curvature.....	104
Fig. 86 Methods for retaining the tube by using the guide rail. ....	104
Fig. 87 Relationship between the radius of curvature and required pushing force. ....	105
Fig. 88 Test on a curved narrow environment. 1,3,5 : the inner tube is in a flexible state and the outer tube is in a highly rigid state. 2,4,6 : the outer tube is in a flexible state and the inner tube is in a highly rigid state. ....	106
Fig. 89 Theoretical comparison of holding torque in proposed mechanisms across	

chapters. ....	111
Fig. 90 Comparison of the previous and proposed methods in terms of the ratio between maximum and minimum stiffness. In Chapters II, III, and IV, the ratios are determined by dividing the peak actual torque value by the actual torque value measured at 0 MPa. ....	114
Fig. 91 The application of the mechanism proposed in Chapter III for above-water and underwater operations using a snake-like form. The application of the mechanism introduced in Chapter IV for underactuated soft grippers without restoring cable. ....	117

## LIST OF TABLES

TABLE I Comparison of previous locking methods based on performance with ratio between the maximum and minimum stiffness, maximum locking values, switching time, energy consumption at the moment of switching.....	15
TABLE II Comparison of previous locking methods based on performance with energy consumption after switching, lockable positions (continuous or discrete or initial), adjustable locking force, presence or absence of a total lock activation feature operated by a single actuator.....	15
TABLE III Parameters for designing 3-axis rotary ball joint. ....	37
TABLE IV Magnification of holding torque in pitch and roll direction at each internal pressure on fem simulation. ....	43
TABLE V Magnification of holding torque in pitch and roll direction at each internal pressure on measurement. ....	43
TABLE VI Error values of holding torque in pitch and roll directions between measured and fem values. ....	43
TABLE VII Error values of holding torque in pitch and roll directions between measured and theoretical values.....	43
TABLE VIII Parameters of ball joints, levers and rubber tube. ....	57
TABLE IX Static friction coefficient values for each internal pressure .....	61
TABLE X Magnification factors between the maximum and minimum holding torque for each internal pressure measurement .....	65
TABLE XI Errors between the theoretical and measured values of the maximum and minimum holding torques with wires and the holding torques without wires .....	65
TABLE XII Specification of the prototype. ....	76
TABLE XIII Theoretical value of the holding torque for each internal pressure	81
TABLE XIV Error values of the holding torque in the bending direction between measured and theoretical values for each internal pressures and inner diameters. ....	82
TABLE XV Specification of the prototype.....	100
TABLE XVI Experimental conditions for measuring required pushing force....	105



# Chapter I

## Introduction

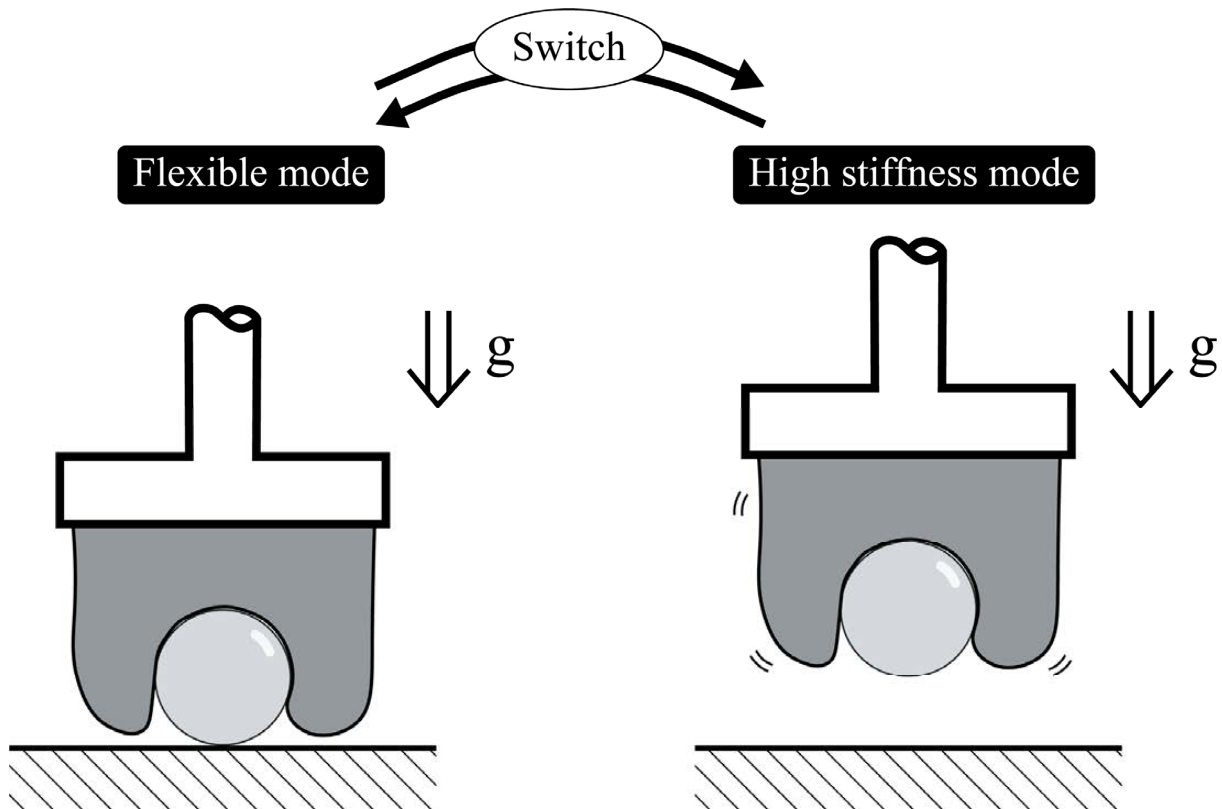
# Chapter I Introduction

## Section I.1 Research background of variable stiffness mechanism in soft robotics.

In recent years, soft robots formed from soft materials like rubber, capable of passive or active bending and twisting deformations, have garnered attention due to their flexibility, which allows them to adapt to their environment and move with the dexterity of living organisms [1]-[3]. These soft robots, devoid of hard parts or structures, pose no risk of harm or destruction to humans or the surrounding environment. Consequently, their application in collaborative tasks with humans, particularly in medical and caregiving settings, is highly anticipated.

However, these soft robots face a challenge: when pushing an object or when an object is placed on them, they cannot support the weight without undergoing deformation. Additionally, the unpredictability of this deformation may compromise stability during support tasks. These are especially problematic in scenarios requiring precise control, as they can increase the difficulty of tasks and operations.

One proposed solution to this problem is the implementation of a mode-switching mechanism that alternates between a flexible mode, which allows deformation, and a high-stiffness mode, which restricts it [4]-[6]. This approach would permit deformation when the robot is not supporting an object, and prevent it when support is needed. For instance, applying this mode-switching functionality to endoscopes or robotic grippers could enhance their utility. An endoscope [7]-[9] could be made flexible for insertion and high stiffness for tasks like removing foreign objects, thereby maintaining its posture during the procedure. Similarly, a gripper [10]-[12] could conform to the shape of an object in its flexible state and then maintain that shape to grasp the object firmly in its high-stiffness state (Fig.1).



**Fig. 1 Behavior of the robotic gripper in flexible and high stiffness modes: In the flexible mode, the gripper deforms to transfer to the shape of the object. In the high stiffness mode, it maintains the shape of the object while being grasped.**

To enable the switching between these flexible and high-stiffness modes, there are methods involving either constraining the movement of multiple rigid components that are oppositely positioned in the robot, or by altering the rigidity of the components themselves [4][6] (Fig.2).

When configuring a robot with components arranged in opposing positions, it is essential to control the relative posture between these components. To allow deformation of the entire structure of the robot, constraints can be turned off; conversely, to suppress deformation, these constraints can be activated (Fig.2(a)).

On the other hand, to change the rigidity of the components themselves, it's necessary to modify parameters that affect rigidity, such as the Young's modulus or the second moment of area. To facilitate deformation, the rigidity of the components can be reduced; to prevent deformation, their rigidity can be increased (Fig.2(b)).

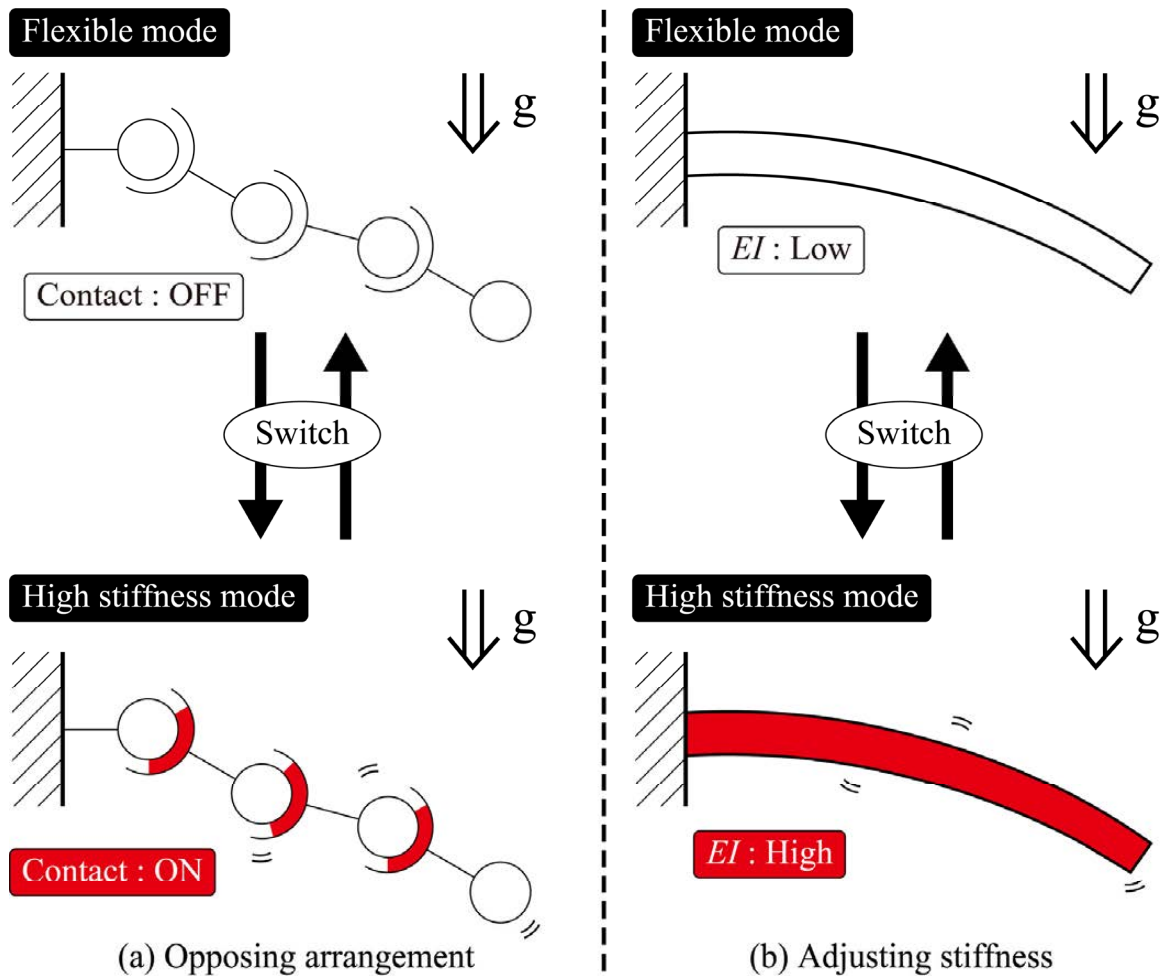


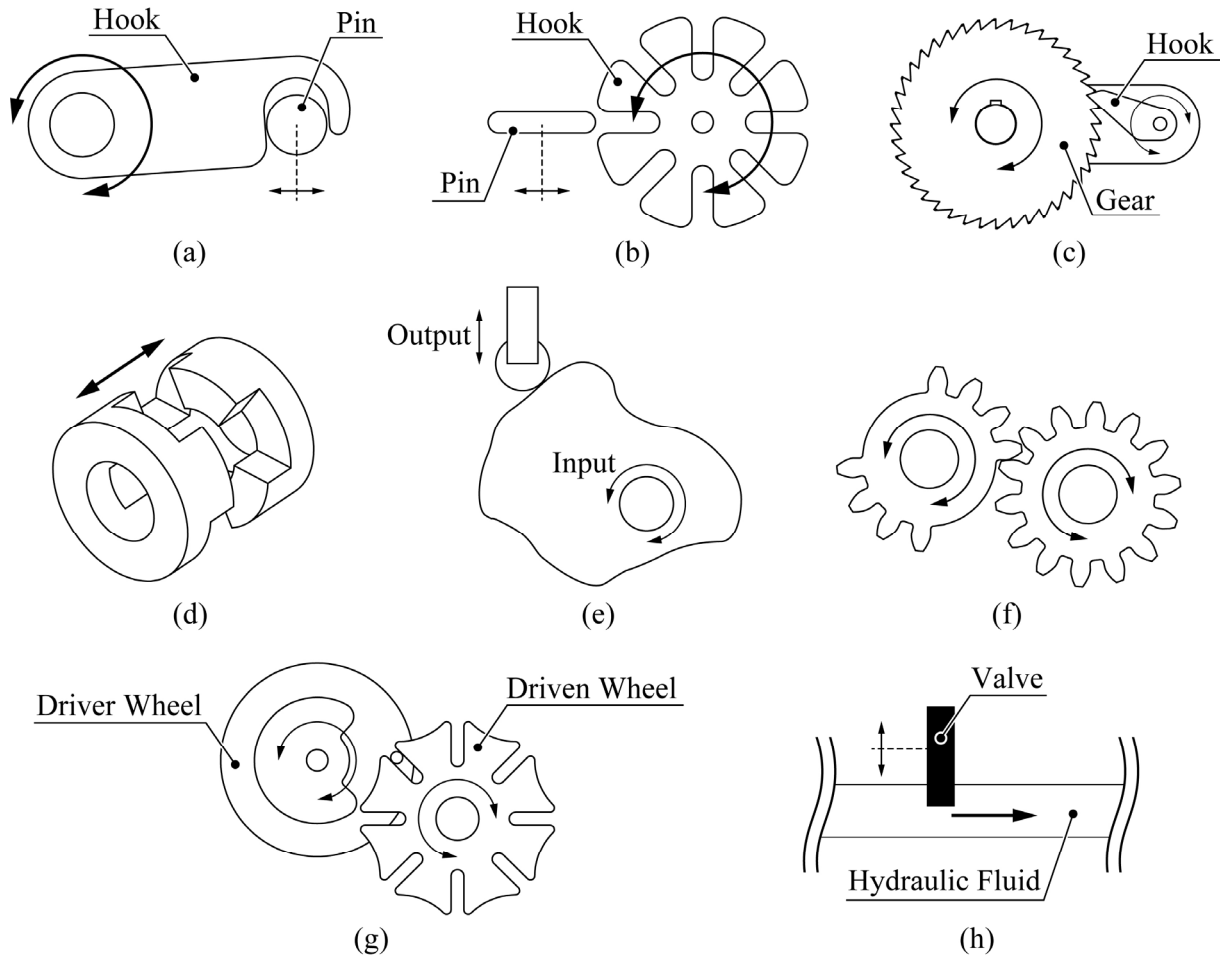
Fig. 2 Methods to switch between flexible and high stiffness modes: (a) By arranging components opposite each other. (b) By adjusting the stiffness of components.  $EI$  is flexural rigidity.

## Section I.2 Previous research of variable stiffness mechanism.

This chapter discusses previous research on variable stiffness mechanisms that consist of structures with multiple components arranged in opposing positions to control the robot's deformation, and mechanisms that achieve deformation control by altering the rigidity of the components themselves.

### Subsection I.2.1 Previous methods to switch between flexible and high stiffness modes by arranging components opposite each other.

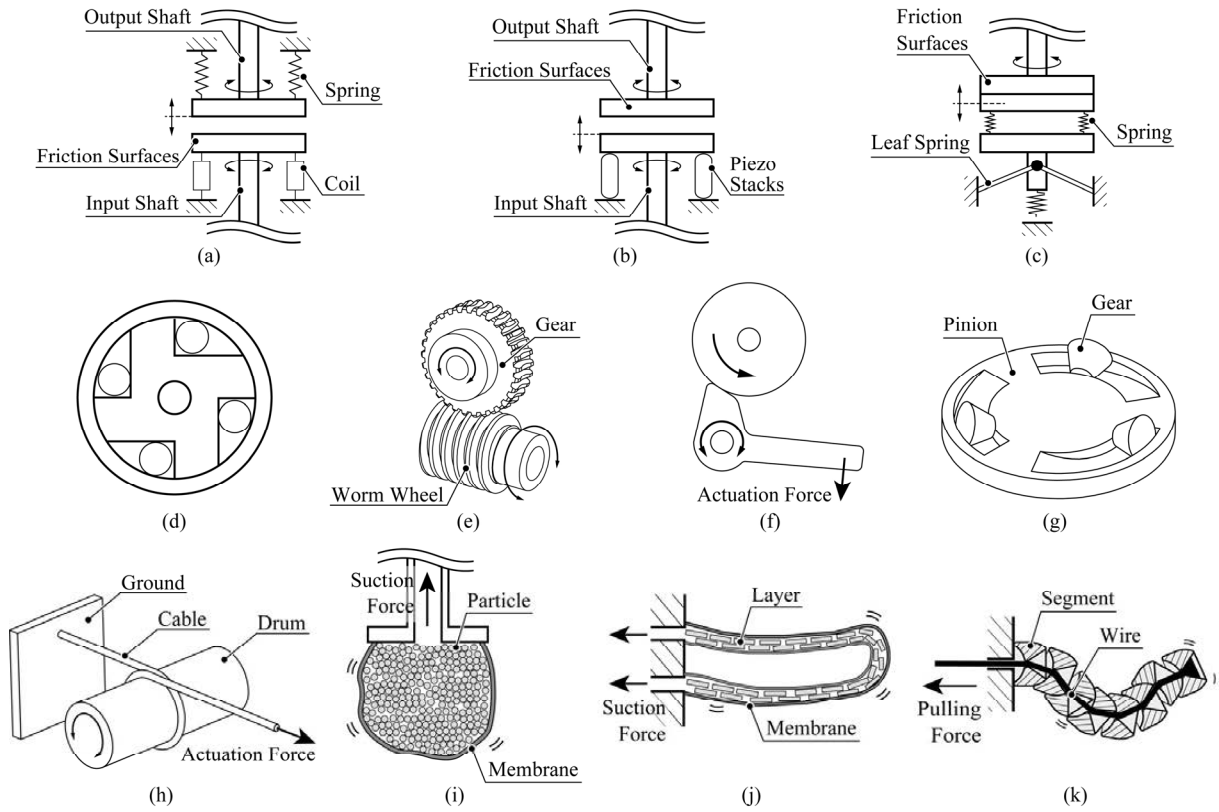
Variable stiffness mechanisms that feature structures with components arranged in opposing positions can primarily be categorized into two types: mechanical methods, which utilize geometric constraints, and friction methods,



**Fig. 3** Types of mechanical locking methods with (a) latch with one locking position, (b) latch with multiple locking positions, (c) ratchet, (d) dog clutch, (e) cam-based with cam follower, (f) cam-based with mutilated gears, (g) cam-based with geneva and (h) hydraulic lock.

which employ constraints based on sliding. These methods exhibit trade-offs in aspects such as the magnitude of locking force, the presence or absence of lock force adjustment capabilities, and the number of locking points.

The mechanical method of variable stiffness mechanisms locks based on the shape and position of components. As it relies on geometric constraints, this method can lock even without friction. Components used in this method include latches, where locking occurs through the interference of one or multiple hooks with a pawl [13]-[22][114][128][133][134], ratchets, which lock in primarily one direction through the interference between a round gear and a pawl [23]-[26], dog clutches, which lock when the male and female parts fit together [27]-[30], cam-based mechanisms that lock through interference between multiple cams [31]-[34], and hydraulic locks, which lock by closing valves in a hydraulic circuit, thereby



**Fig. 4** Types of friction-based locking devices with (a) an electromagnetic brake, (b) a piezo-actuated brake, (c) a statically balanced brake, (d) an overrunning clutch, (e) a nonbackdrivable gear, (f) a self-engaging brake, (g) a self-engaging pinion-gear mechanism, (h) a capstan, (i) particles, (j) layers and (k) segments.

obstructing the flow of fluid [35]-[38] (Fig.3).

In the mechanical method, due to its reliance on geometric constraints, a high locking force is achievable. Additionally, as there is no need to actuate the hook after stopping rotational or translational motion, this method consumes less operational energy. However, it also has the characteristic of having discrete locking positions, making it difficult to adjust the locking force.

The friction method controls the restraining force through the normal force between components and the coefficient of friction. Components used in this method include electromagnetic (EM) locks, which control the interference of two friction surfaces using electromagnets [39]-[42], piezoelectric locks that use piezoelectric actuators to control the interference of two friction surfaces [43]-[47], statically balanced locks, which control the interference of two friction surfaces using springs [48], overrunning locks that work based on the relative rotational speed of two concentric rings with interposed cylinders or balls [49]-[53], nonbackdrivable gears such as worm gears for locking [54]-[59], self-amplifying

locks that amplify braking force through leverage [60][61], capstans that amplify the locking force while locking through drums and cables [62]-[67], and particle [10][68]-[72], layer [73]-[78][135], or segments [79]-[87][136] based locks, which employ the frictional force between two or more objects (Fig.4).

In the friction method, which employs sliding to control locking, it is possible to adjust the locking force, and the locking positions are continuous, contrasting with the mechanical method. However, the locking force is less than that of the mechanical method, and this approach often results in higher energy consumption as it requires continuous operational energy to maintain contact between components.

To control the interaction caused by interference between components, it is common to employ either an electric method using motors or piezoelectric elements, or a fluidic method using air, water, or hydraulic fluid as the working medium. The reason these methods are applied is that, in both mechanical and friction methods, controlling the lock typically requires changing the relative position of the components through translational or rotational motion. Electric and fluidic actuators can easily produce such translational or rotational movements, making them suitable for use in both mechanical and friction methods, especially when the volume of the locking device can be disregarded.

In the case of electric methods, mechanical methods employ components such as ratchets [26] (Fig.5) and dog clutches [28] (Fig.6), while friction methods use brakes [42] (Fig.7), joints [83] (Fig.8), and clutches [47] (Fig.9) for switching locks. These methods provide high locking force and shorter lock on/off switching times. However, they may lead to an increase in the number of actuators required depending on the volume of the locking device and the number of locking points, which can make it challenging to reduce the weight of the device.

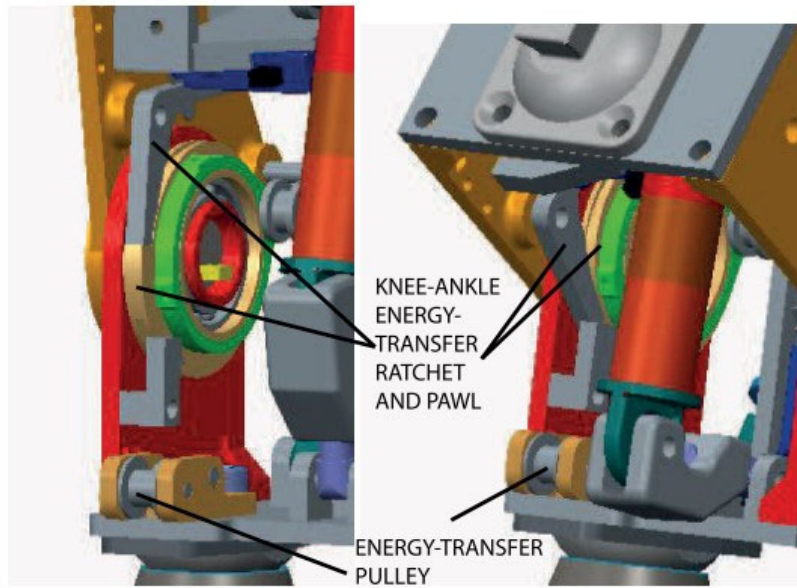


Fig. 5 Operation of the energy transfer ratchet mechanism in the prosthetic knee [26].

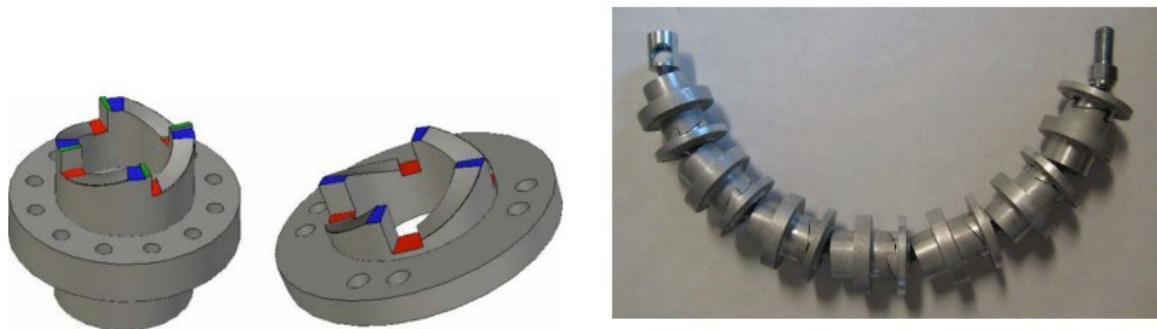
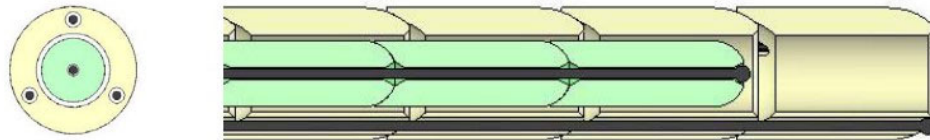


Fig. 6 Split collars for mechanical locking using a dog clutch [28].

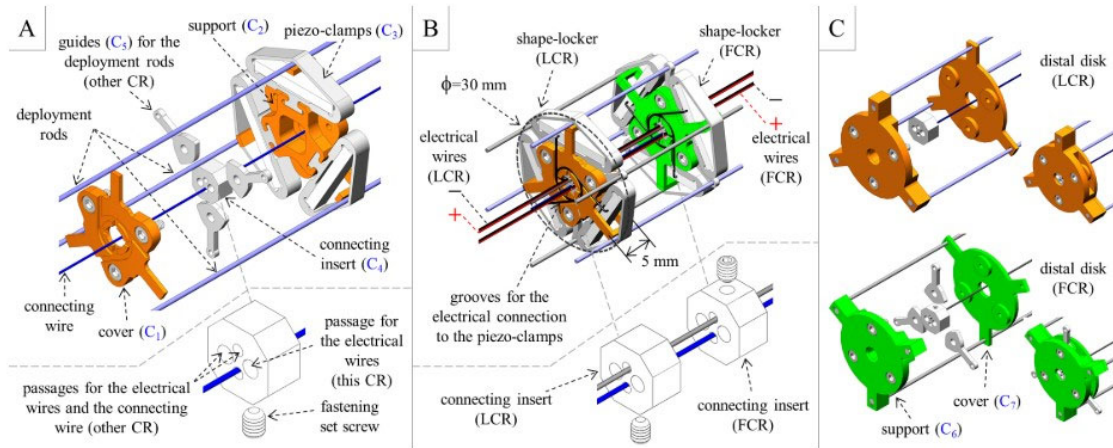


Fig. 7 Clutchable series-elastic actuator knee using electromagnetic brake [42].





**Fig. 8** Articulated robotic probe with frictional locking mechanism by pulling wire using motor [83].



**Fig. 9** Design of shape-lockers and distal disks using piezo wire clamp mechanism by friction [47].

In contrast, fluidic methods can achieve equivalent locking force and lock on/off switching times as electric methods, with the added potential for easier lightening of the lock device compared to electric methods. In fluidic actuation, mechanical methods employ components like latches [22] (Fig.10), while friction methods use cylinders [86] (Fig.11), rubber tubes [87] (Fig.12), particles [70] (Fig.13), or layers [78] (Fig.14) for switching locks. To achieve high locking force, it suffices to set a high supply pressure. Although the lock on/off switching times may be longer compared to electric methods, they can be shortened depending on the supply pressure. Additionally, when using a fixed volume of fluid, the device can be made lighter by employing low-density gasses and, depending on the design of the flow paths, it is possible to control all locking elements with a single actuator regardless of the number of locking points, further facilitating weight reduction.

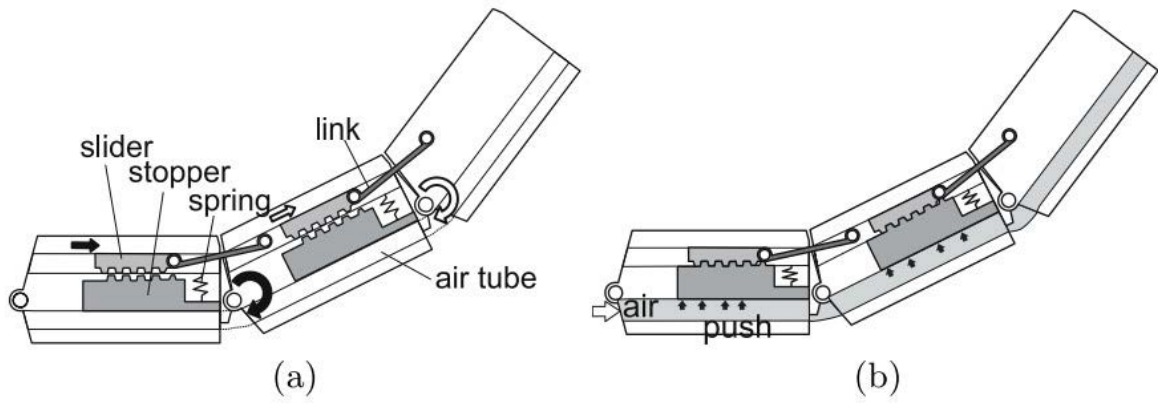


Fig. 10 Rigid-flexible outer sheath model with mechanical locking by the gear rack of the slider and air pressure [22].

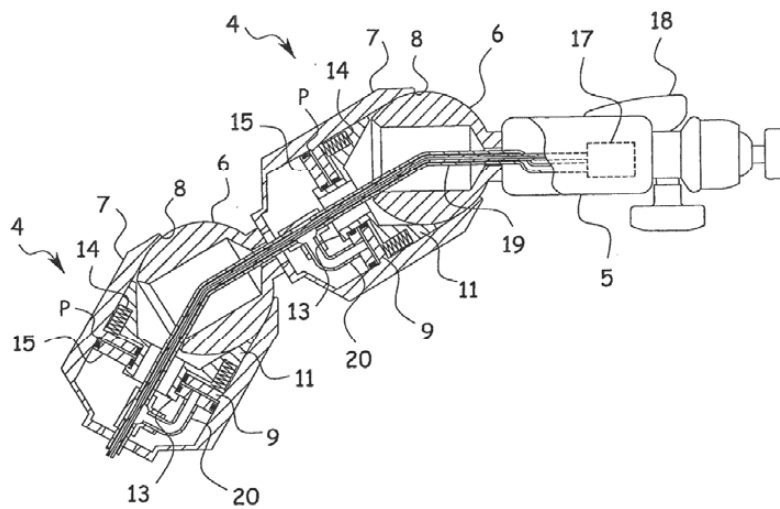


Fig. 11 Tool holding articulated arm with frictional locking using air cylinder [86].

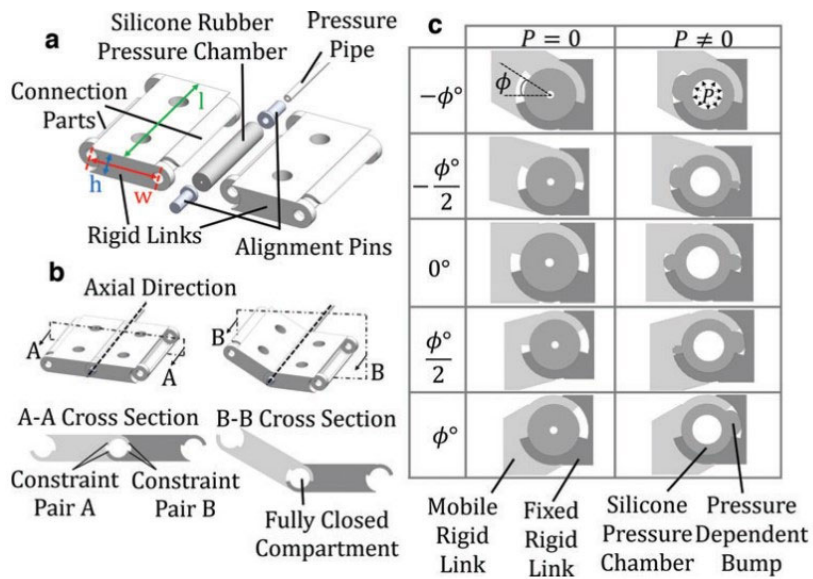


Fig. 12 Pressure-driven manipulator becomes high stiffness owing to the friction between the rubber chamber and rigid walls [87].

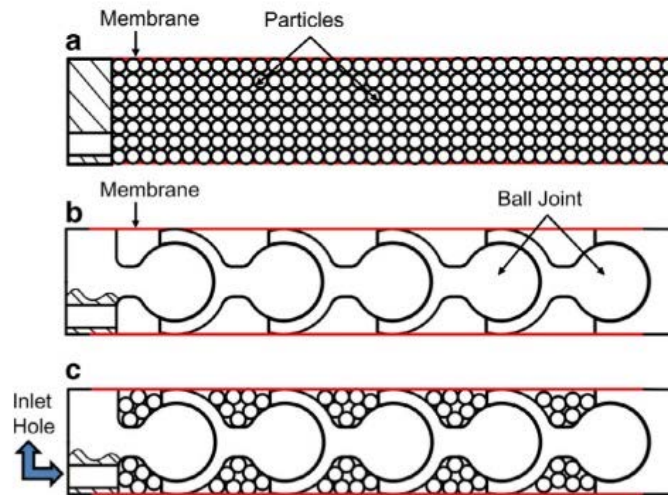


Fig. 13 Soft robotic spine with tunable stiffness based on joint and particle jamming [70].

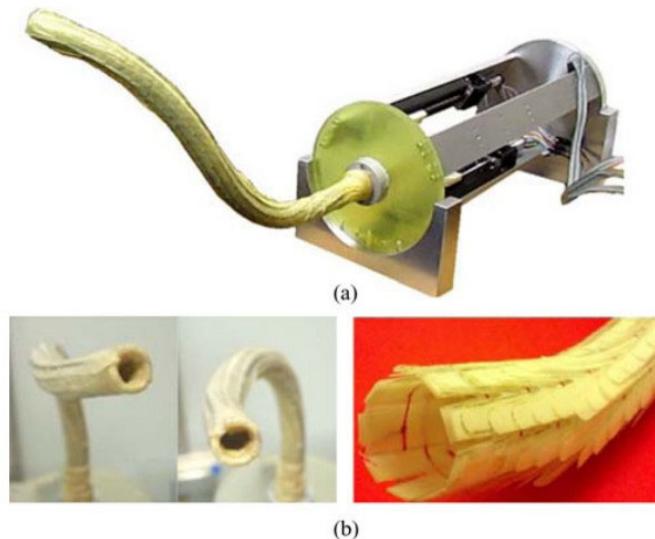


Fig. 14 Tubular snake-like manipulator prototype with tunable stiffness based on layer jamming [78].

### Subsection I.2.2 Previous methods to switch between flexible and high stiffness modes by adjusting the stiffness of components.

In variable stiffness mechanisms that alter the rigidity of the components themselves to control the robot's deformation, the primary method is the material method, where the constraining force is determined by the stiffness of the materials used in the components. Existing research includes phase change approaches utilizing low melting point alloys [88]-[92][137] / polymers [93]-[97] (Fig.15), glass transition approaches using shape memory alloys [98]-[102][138] / polymers [103]-[106][139] (Fig.16), functional fluid approaches employing MR

materials [107]-[109] and ER materials [109]-[111][140][141](Fig.17), and approaches that vary stiffness by deforming the cross-sectional area and structural interactions, such as the area's moment of inertia [112][113][142] (Fig.18).

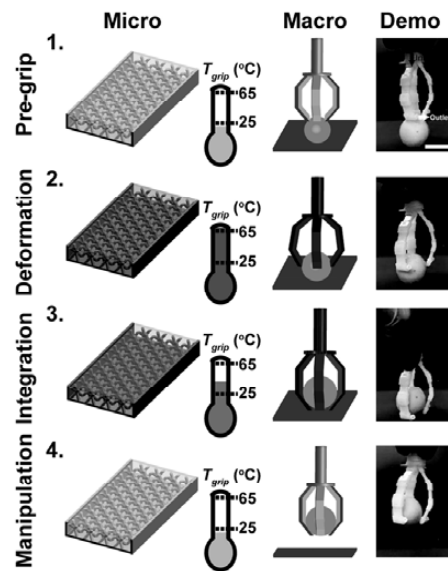
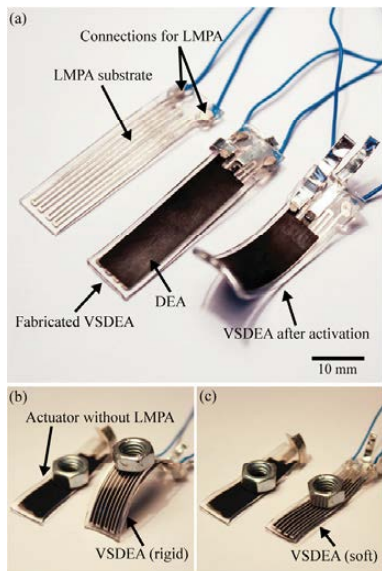
In these approaches, to alter the rigidity of the components themselves, it is necessary to modify the stimuli based on the physical properties of the materials used. This may involve applying heat, electric/magnetic fields, or inducing deformation (such as bending or curving). Additionally, increasing the area moment of inertia through structural interaction is also a viable method.

When utilizing heat, the phase transitions and glass transitions of the material are exploited. This results in high locking force at low temperatures, and an increased capacity for deformation at higher temperatures. However, a tendency for prolonged switching times is observed, with the transition occasionally taking several minutes.

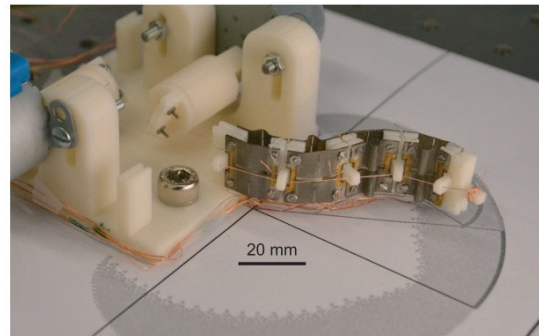
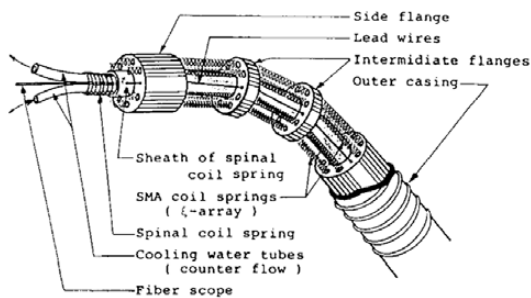
In the context of magnetic and electric fields, functional materials such as MR (Magnetorheological) and ER (Electrorheological) particles are utilized. This approach allows for lockable positions with continuous, and the switching time for locking is relatively short. However, as these functional materials primarily alter resistance through viscosity, there tends to be a lower locking force.

The trade-off between locking force and the duration of lock on/off switching times in the area's moment of inertia approach depends on the deformations. This can allow for high locking force and reduced switching times by using thin sheets, However, in this method, no shape-locking is possible, and the initial configuration is the only stable one.

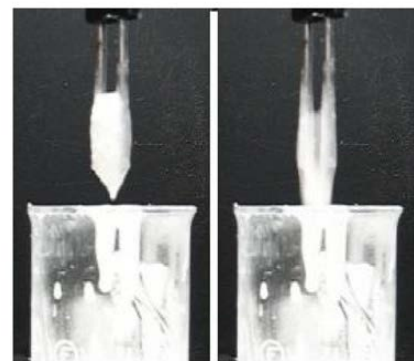
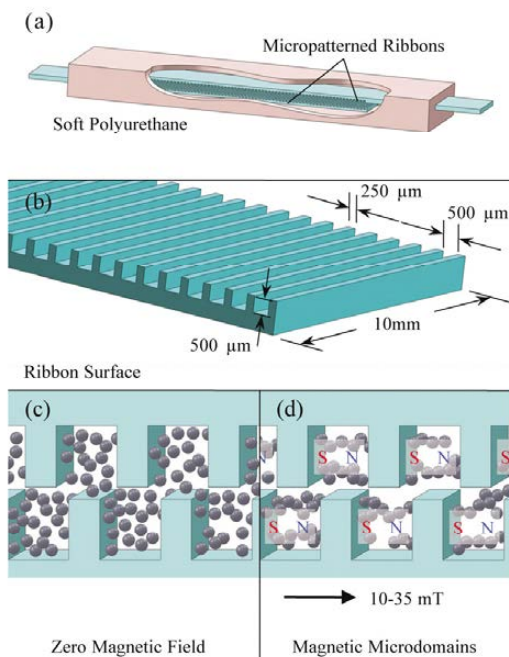
The area moment of inertia method, facilitated through structural interaction, employs a mechanism where the layers remain separated under flexible conditions and bond together in a state of high rigidity, functioning collectively as a single large beam characterized by a substantial area moment of inertia. An increase in the number of layers correlates with enhanced locking strength. Nonetheless, the rigidity achieved is anisotropic relative to the deformation direction, limiting lockable positions with continuous control to 1-axis direction.



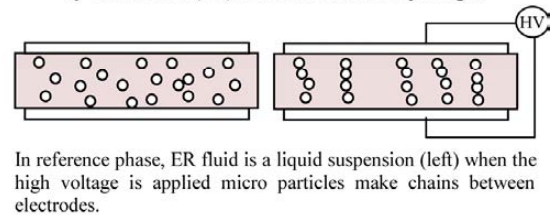
**Fig. 15** Material locking mechanism with low melting point alloys [90] / polymers [96]. Stiffness is changed by thermal stimulation.



**Fig. 16** Material locking mechanism with shape memory alloys [98] / polymers [104]. Stiffness is changed by thermal stimulation.

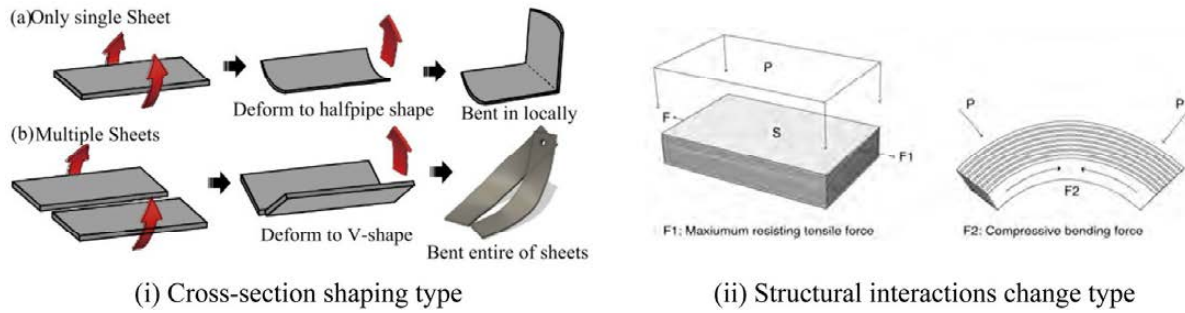


Electro-rheological fluid is transferred to the gel phase, by electric field (left) and returned to the liquid right.



In reference phase, ER fluid is a liquid suspension (left) when the high voltage is applied micro particles make chains between electrodes.

**Fig. 17** Magnetorheological [107] and electrorheological [110] variable stiffness mechanism.



**Fig. 18 Variable stiffness mechanism through the alteration of the area's moment of inertia. (i) Cross-section type[112] and (ii) Structural interactions change type[142].**

### Subsection I.2.3 Comparison of locking methods between arranging components in an opposite manner and adjusting the stiffness based on performance.

This subsection presents a comparison of the performance of the conventional methods previously discussed, as shown in Table I and II. These tables detail, for each type of locking mechanism, the ratio between the maximum and minimum stiffness, maximum locking values, switching time, energy consumption at the moment of switching, lockable positions (continuous or discrete or initial), adjustable locking force, presence or absence of a total lock activation feature operated by a single actuator.

In Table I, one of the parameters, the ratio of high-stiffness mode to flexible mode, is calculated by dividing the maximum lock force by the minimum lock force. A larger ratio indicates a greater locking force in the high-stiffness mode, allowing for a comparative assessment of locking performance using this ratio.

Additionally, Table I includes the lock switching time. It should be noted that the energy consumed at the moment of locking can increase with longer lock switching times. For instance, phase change and glass transition methods that utilize heat tend to have longer heating and cooling durations, potentially leading to increased energy consumption.

Table II presents the energy consumption associated with each method following switching. This comparison is based on the necessity of continuing actuator operation post-actuation. For the mechanical, phase change, and glass transition methods, post-actuation operation of the actuator is not required. Conversely, the friction, functional material, and area's moment of inertia methods necessitate sustained actuator operation to maintain their locking states.

Also, Table II presents the lockable positions, where a continuous design allows for a greater number of lockable postures, whereas a discrete design results in fewer locking points. The term 'Initial' refers to a mismatch between the locking force in the initial and deformed shapes. For example, in the second moment of area method, where the cross-sectional shape is altered, there can be discrepancies between the desired locking force and the amount of displacement due to the varying stiffness with displacement.

Moreover, Table II explains the presence of locking force adjustment functionality and the ability to operate all locks with a single actuator. Possessing the capability to adjust locking force helps to avoid applying excessive force, thus

**TABLE I**  
**COMPARISON OF PREVIOUS LOCKING METHODS BASED ON PERFORMANCE WITH RATIO BETWEEN THE MAXIMUM AND MINIMUM STIFFNESS, MAXIMUM LOCKING VALUES, SWITCHING TIME, ENERGY CONSUMPTION AT THE MOMENT OF SWITCHING.**

	Ratio between the maximum and minimum stiffness	Maximum Locking Values	Switching Time for Lock On/Off	Energy consumption at the moment of switching
Mechanical ( Electric ) [28][128]	Until breaks [28][128]	100 kg [28], 6.8Nm [128]	Short	Low
Mechanical ( Fluid ) Negative[133][134]/Positive[22][114]	2.5-6 times [133][134] / Until breaks [22][114]	29.55 Ncm [133], 3 N [134] / 400 mNm [22], No data [114]	Medium	Medium
Friction ( Electric ) [47][135]	No data [47], 7 times [135]	1.5 N/mm [47] / 6 N [135]	Short	Low
Friction ( Fluid ) Negative[70][78]/Positive[87][136]	13.5-56 times[70][78] / 1.8-4 times[87][136]	280Nmm [70], 2.7Nmm [78] / 170Nmm [87], 0.24N/mm [136]	Medium	Medium
Phase Transition LMPA[88][137]/LMPP[93][95]	25-10 <sup>4</sup> times[88][137]/ 14-86 times [93][95]	371.2Ncm <sup>2</sup> [88], 40MPa [137]/ 2828MPa [93],190MPa [95]	Long	High
Glass Transition SMA[98][138]/SMP[104][139]	8-10 times [138]/ 2-10 times [104][139]	No data [98], 2 N [138] / 1000 Nmm/rad [104], 6500 N/m [139]	Long	High
Rheological Materials MR[107][108]/ER[140][141]	8.8-31.5 times [107][108]/ 10 times [140][141]	106 kPa [107], 31.5 Nm [108] / No data[140], 300kPa [141]	Short	Low
Area's Moment of Inertia [112][142]	8.7-34.5 times [112][142]	81 mN/mm [112] / 0.69Nm [142]	Short [112] / Medium [142]	Low[112] / Medium [142]

**TABLE II**  
**COMPARISON OF PREVIOUS LOCKING METHODS BASED ON PERFORMANCE WITH ENERGY CONSUMPTION AFTER SWITCHING, LOCKABLE POSITIONS (CONTINUOUS OR DISCRETE OR INITIAL), ADJUSTABLE LOCKING FORCE, PRESENCE OR ABSENCE OF A TOTAL LOCK ACTIVATION FEATURE OPERATED BY A SINGLE ACTUATOR.**

	Energy consumption after switching	Lockable Positions :Continuous/Discrete/Initial	Adjustable Locking Force	Presence or absence of a total lock activation feature operated by a single actuator
Mechanical ( Electric ) [28][128]	Low	Discrete	No	No
Mechanical ( Fluid ) Negative[133][134]/Positive[22][114]	Low	Discrete	No	Yes
Friction ( Electric ) [47][135]	High	Continuous	Yes	No
Friction ( Fluid ) Negative[70][78]/Positive[87][136]	High	Continuous	Yes	Yes
Phase Transition LMPA[88][137]/LMPP[93][95]	Low	Continuous	Yes	Yes
Glass Transition SMA[98][138]/SMP[104][139]	Low	Continuous	Yes	Yes
Rheological Materials MR[107][108]/ER[140][141]	High	Continuous	Yes	No
Area's Moment of Inertia [112][142]	High	Initial[112] / Continuous(1-axis direction) [142]	Yes	No [112] / Yes [142]

reducing the likelihood of damage and failure. Additionally, reducing the number of actuators relative to the number of locking points can prevent the structure from becoming overly complex.

### **Section I.3 Proposed principle: variable stiffness mechanism structured with oppositely arranged components, controlling locking via friction and positive-pressure.**

This study focuses on developing a variable stiffness mechanism capable of high ratio of high-rigidity mode to flexible mode and a lockable position with continuous, and reducing lock on/off switching times, enabling adjustment of locking force and the ability to operate all locks with a single actuator.

As derived from Table I and II, a locking mechanism is adopted that combines a friction method with components arranged in opposing positions, where the locking points can be arbitrarily determined, and a fluidic method using air, a fluid with minimal environmental impact in case of leakage. The use of positive pressure, which can be increased based on the pressure resistance of tubes and joints, enables the realization of high locking force. The friction method, employing flat surfaces, is highly suitable for achieving a lockable position with continuous, as it allows for arbitrary locking positions. The use of air, combined with the friction mechanism, enables the adjustment of locking force. Moreover, shortening the lock on/off switching times can potentially be achieved by increasing the pressure. Utilizing fluidic actuation allows for the distribution of the working fluid throughout the entire structure depending on the flow path design; for instance, in planar structures, a single actuator may suffice if the flow paths are interconnected.

In addition to these performance achievements, the fluidic method allows for energy transmission over long distances or to fine structures, and is characterized by minimal energy attenuation, such as sliding resistance, in the process of transmitting force throughout the structure.

### **Section I.4 Research purpose of this study.**

The objective of this research is to develop a design methodology for a positive-



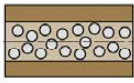
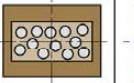



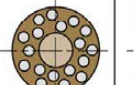


pressurized variable stiffness mechanism that can arbitrarily switch between flexible and high-stiffness using friction and air pressure. To achieve this objective, the following four areas are addressed:

**(1) Investigation of structures that can output frictional shape-holding torques by expansion forces during positive-pressurization.**

To construct a variable stiffness mechanism through positive-pressurization, it is necessary to materialize a structure that can suppress the expansion deformation of the pressurized chamber while outputting the frictional shape-holding force unlike negative-pressurization. Rubber tubes, suitable for achieving high degrees of deformation freedom, typically undergo expansion deformation when pressurized, making it difficult to maintain arbitrary shapes. Therefore, it is essential to position components ahead of the expanding direction of the rubber tube to suppress its deformation (Fig.19).

The desired attributes of a component engineered to mitigate the expansion deformation of a rubber tube while outputting the friction-based holding force include a hollow structure for the tube's passage, the strength to suppress the tube's expansion force, and a high degree of freedom in responding to deformation. To control the rubber tube's expansion, it should be situated inside the component, which in turn must have the strength of components to endure significant forces generated by pneumatic pressure. Furthermore, for the component to lock in various shapes, its design necessitates multiple degrees of freedom.

This research focuses on the spherical surface joint as a structural solution to fulfill these requirements. In this study, I have adopted a structure that involves the oppositional arrangement of spherical surface joints with rubber tubes enclosed within multiple joints. This structure allows for locking in arbitrary shapes when pressurized and enables high holding force and force adjustment depending on the supply pressure. Unlike the negative pressure method that fills components inside a rubber membrane bag, this proposed method encloses the rubber tube, thus eliminating contact with sharp objects like blades, aiming for improved durability. Also, the system is limited to applying a maximum negative pressure of 0.1 MPa, while it is capable of supplying an internal pressure exceeding 0.1 MPa for positive-pressurization.

Chamber shapes	Negative Pressure		Positive Pressure	
Rectangle	 Particle type	 Layer type	 1 axis rotary joint type	
Axial Symmetry	 Particle type	 Layer type	 3 axis rotary joint type	

**Fig. 19 Classification of variable stiffness mechanism by friction using pneumatic pressure. They can be roughly classified into two groups negative-pressure and positive-pressure methods. The common points are that the variable stiffness function is maintained by changing the structure and arrangement of the chamber and components.**

Fig. 20 illustrates the method of forming multi-joint structures using spherical surface joints and rubber tubes. When employing spherical surface joints, it is possible to create multi-joint structures. The arrangement of these joints can be categorized into two types: an interlinked structure where the joints are physically connected, and a partitioned structure where the joints are physically separated. These joint structures are further classified based on the direction of the expansion force during positive-pressurization. In Fig. 20, the vertical entries represent the direction of the force as radial and axial, while the horizontal entries classify the direction of force as positive (expansive) and negative (contractive).

In the radial direction, the combination of expansive force, which is a positive force, and an interlinked structure is found to be suitable. In this scenario, enclosing the rubber tube inside the joint is considered a positive direction, as it leads to rubber tube expansion. Conversely, placing the rubber tube outside the joint, which causes the joint to compress, is deemed a negative direction. The positive direction allows for locking under positive-pressurization. However, in the negative direction, where the rubber tube is placed externally, it is impractical as it necessitates an additional component around the tube to suppress its expansion.

In the axial direction, the combination of extension force, which is a positive force, with an interlinked structure is appropriate, as is the combination of contractive force, a negative force, with both interlinked and partitioned structures. For axial extension force considered positive, an interlinked structure can achieve a holding

force. However, in a partitioned structure, the joints would separate, making locking unfeasible. In contrast, for axial contractive force by using the pneumatic artificial muscle, perceived as negative, both interlinked and partitioned structures can achieve holding force as the joints come into contact.

**Interlinked Spherical Dyad Joint**

Positive or negative direction of force Direction of force	Positive direction	Negative direction
Radial direction		
Axial direction		

**Partitioned Spherical Dyad Joint**

Positive or negative direction of force Direction of force	Positive direction	Negative direction
Radial direction		
Axial direction		

Fig. 20 Method of forming multi-joint structures using spherical surface joints and rubber tubes. The arrangement of these joints is categorized into two types: an interlinked structure where the joints are physically connected, and a partitioned structure where the joints are physically separated. The vertical entries represent the direction of the force as radial and axial, while the horizontal entries classify the direction of force as positive (expansive) and negative (contractive).

**(2) Theoretical development, analysis, and empirical measurement of holding torque during positive-pressurization in the proposed mechanism.**

To evaluate the holding performance of the proposed radially expandable type and axially contraction type mechanisms, theoretical development, finite element analysis, and empirical measurements of the holding torque are conducted. Since the holding torque of the proposed mechanism varies depending on the material and shape of the joints and rubber tubes, theoretical development is undertaken to calculate the holding torque based on the design values of the joints. Furthermore, finite element analysis, including the highly non-linear rubber tubes, and empirical measurements using the designed and realized joints are conducted to determine the holding torque.

**(3) Development of a hollow multi-layered structure variable stiffness snake-like form capable of alternate propulsion in narrow spaces.**

As one of the applications and expansions of the proposed mechanism, a prototype of a variable stiffness snake-like form with a hollow multi-layered structure is realized. The effectiveness of the principle of alternate propulsion is verified through push force measurement experiments using the internal and external snake-like actual device. The positive-pressurization method is suitable for this mechanism since it allows for an increased driving pressure in accordance with the pressure resistance of the joints and chambers, and the process of converting expansion force into frictional force results in minimal attenuation of holding force regardless of the tube structure's volume, thus facilitating energy transmission even in elongated structures like a snake. The effectiveness of the conceived principle is verified through propulsion tests using the actual prototype of the variable stiffness snake-like form.

**(4) Comparisons of the previous and proposed methods in terms of the locking performance via theoretical and empirical measurements.**

First, comparing the holding torque obtained from each model will clarify the locking performance of the proposed mechanism. For evaluating the locking performance of proposed mechanism, this study performs a theoretical comparison under conditions where internal pressure, joint radius, rubber tube radius, friction coefficient, and angle of shell range to the tip of male joint are standardized.

Also, this research indicates the comparison of the previous and proposed methods in terms of the ratio between maximum and minimum stiffness. Fig. 21 illustrates the comparative ratio of the flexible mode to the high-stiffness mode for each previous method outlined in Tables I and II. The locking performance of the proposed mechanism is analyzed by calculating its flexible-to-high-rigidity mode ratio and comparing this ratio against those of the previous methods. Additionally, this investigation will include a detailed discussion on strategies to optimize these ratios.

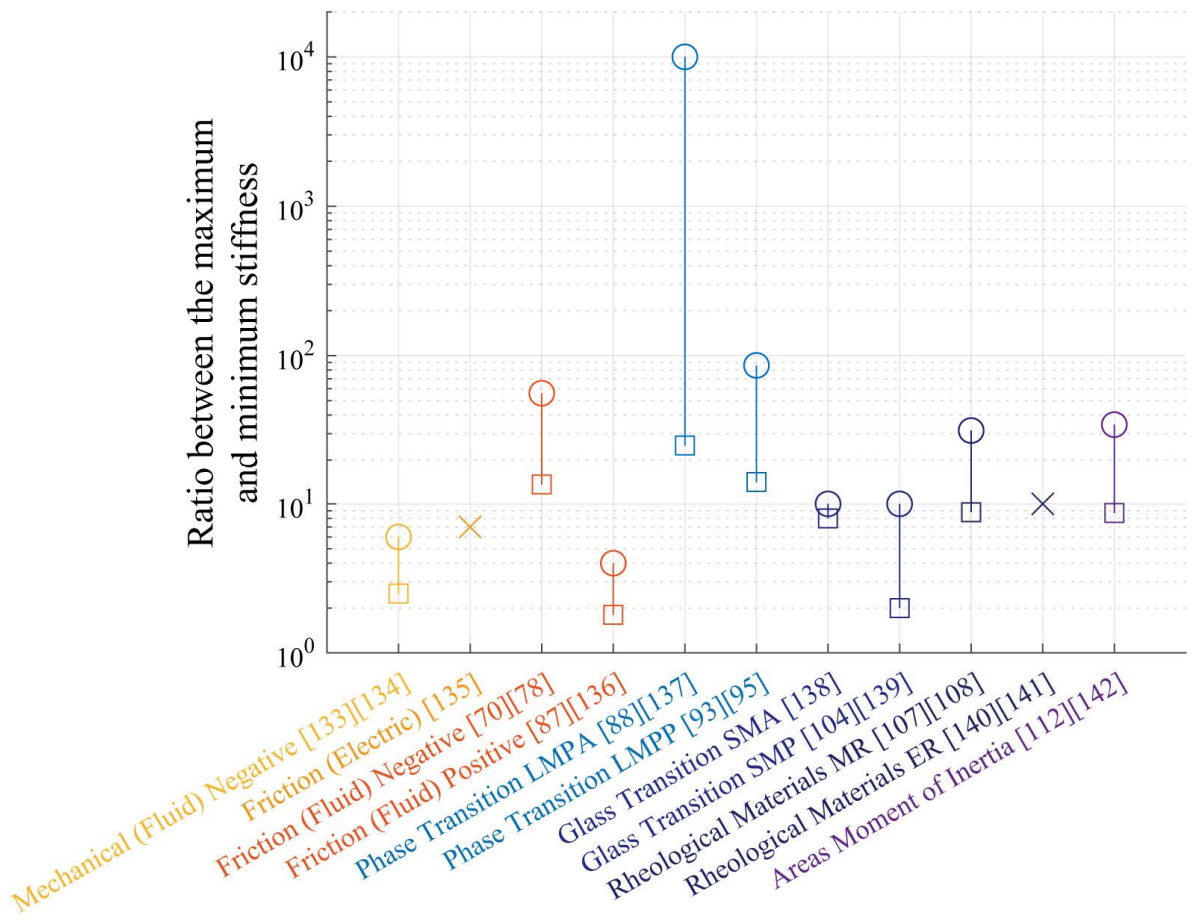


Fig. 21 Comparison of the previous methods in terms of the ratio between maximum and minimum stiffness.

## Section I.5 Structure of the thesis.

Fig. 22 schematizes the structure of this thesis.

This study discusses the three proposed mechanisms according to Fig.20. Chapters III and IV mechanisms enhance the fundamental, radially expandable type mechanism of Chapter II. Also, this study introduces one application mechanism (Chapter V) using the proposed mechanism of Chapter II. The details

of each section are explained as follows.

Chapter II evaluates the locking performance of a radially expandable type mechanism combining ball joints with slits and rubber tubes. The assembly feasibility of multi-joint structures, dislocation prevention during pressurization, and joint holding force are the focus, with ball joints designed and fabricated based on theoretical principles. The radially expandable type joints, being ball joint-shaped and enclosing rubber tubes, facilitate the assembly of link structures and prevent joint dislocation due to tube elongation under pressure. The joint holding torque is clarified through theoretical models, finite element analysis, and empirical measurements.

Chapter III conducts an evaluation of the locking performance of a radially expandable type mechanism, which combines ball joints and rubber tubes, levers clamping wires. The ball joint in this mechanism is characterized by its absence of slits, demonstrates enhanced joint strength and a markedly reduced risk of dislocation. The holding performance of this mechanism, which maintains shape through frictional holding forces between ball joints and between levers and wires, is assessed both theoretically and empirically. The proposed mechanism's anisotropic holding torque in the bending direction, due to the use of wires, is investigated to determine its maximum and minimum holding torques. Moreover, a comparison of holding torques with and without levers clarifies the impact of wire clamping alone on holding torque.

Chapter IV assesses the shape holding and shape-restoration performance of an axially contraction type mechanism combining bowl joints with McKibben-type pneumatic artificial muscles. In this mechanism, the control of locking is governed by contraction forces, fundamentally resolving the issue of dislocation caused by the extension of the chamber during positive-pressurization. The joint holding torque in the axially contraction type is evaluated based on theoretical models and empirical measurements, elucidating the relationship between internal pressure and joint radius. Regarding shape-restoration effects, the shape-restoration angles under varying flow rates are measured to establish the relationship between flow rate changes and shape-restoration angles.

Chapter V evaluates the propulsion performance of a hollow multi-layered

structure variable stiffness snake-like form capable of alternate propulsion. Using a prototype of the variable stiffness snake-like form developed in this research, sliding resistance between prototypes during alternate propulsion is measured to verify its effectiveness. The procedure for alternate propulsion involves initially bending the tip of the internal prototype in the direction of propulsion when connected to an actively bending mechanism. Then, the internal prototype is high-stiffened, and the external prototype, in a flexible state, is pushed along the shape of the internal prototype to its tip. Subsequently, the external prototype is high-stiffened, and the internal prototype is pushed out in its flexible state, repeating this action. This confirms the ability to push the flexible prototype without losing the shape of the propelled prototype against the resistance during alternate propulsion.

Finally, Chapter VI presents the Comparisons of the previous and proposed methods in terms of the locking performance via theoretical and empirical measurements, conclusion and future aspects of the study.

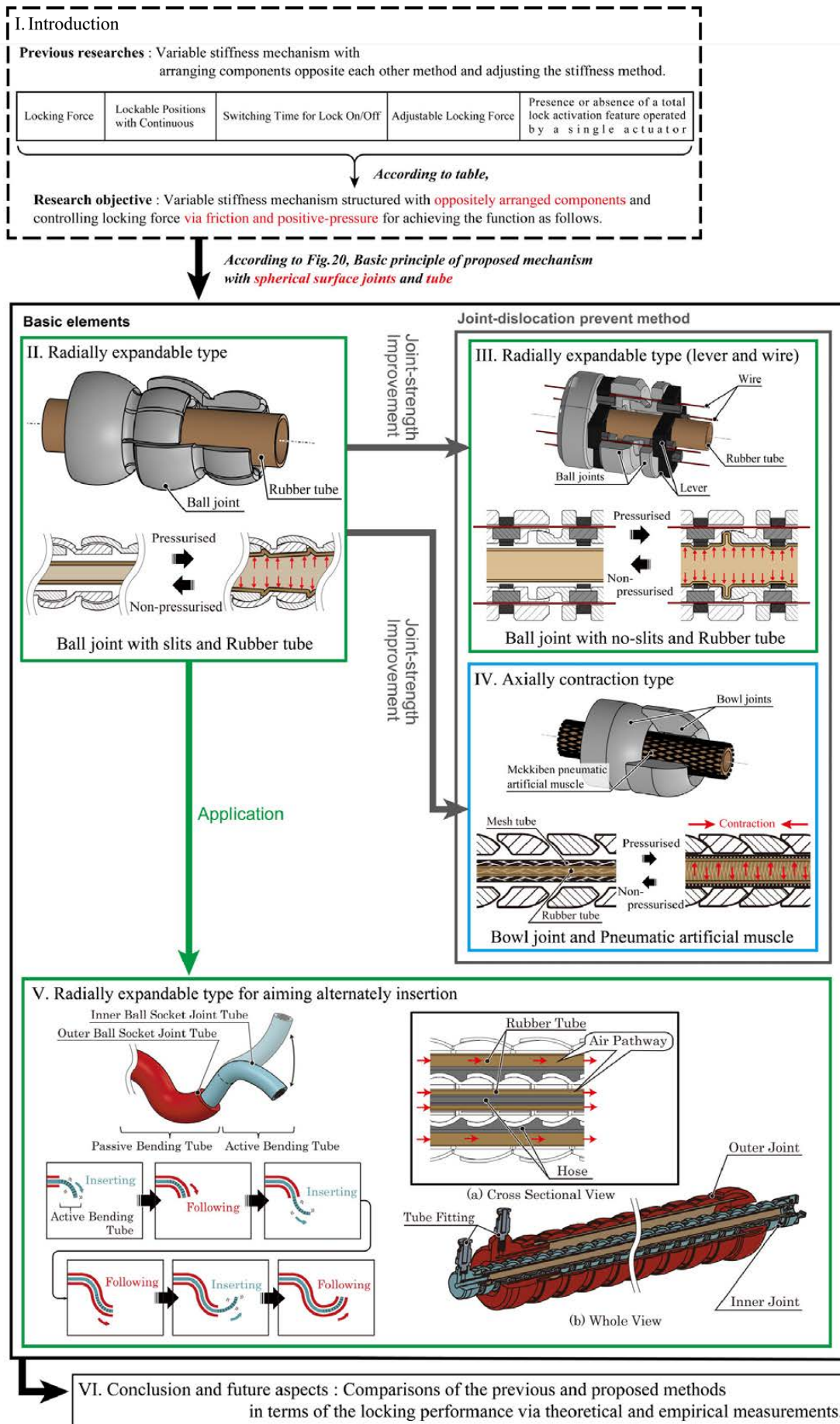


Fig. 22 Structure of this thesis.



## Chapter II

Tube Mechanism with 3-axis Rotary  
Joints Structure to Achieve Variable  
Stiffness Using Positive Pressure

# Chapter II Tube Mechanism with 3-axis Rotary Joints Structure to Achieve Variable Stiffness Using Positive Pressure

## Section II.1 Abstract of Chapter II.

In this chapter, variable stiffness mechanism via frictional force using positive-pressurization consists of single rubber tube enclosed inside a 3-axis rotary ball joints with slits is discussed. The prototype of proposed mechanism has an articulated structure based on a linked joint that can deform freely when internal pressure is not applied and achieves to lock joint angles when internal pressure is applied (Fig. 23).

This method facilitates variable stiffness functions by expanding force in an enclosed chamber. For the joint shape in proposed method, although it is necessary to provide an expandable hemisphere in the ball joint type, only a hollow male-female joint structure is required. Although the number of joints increases with the total length of the structure, the only components required to form an articulated structure were the joints, chambers, and fittings to keep the chambers sealed. In addition, the proposed mechanism does not have any sliding resistance.

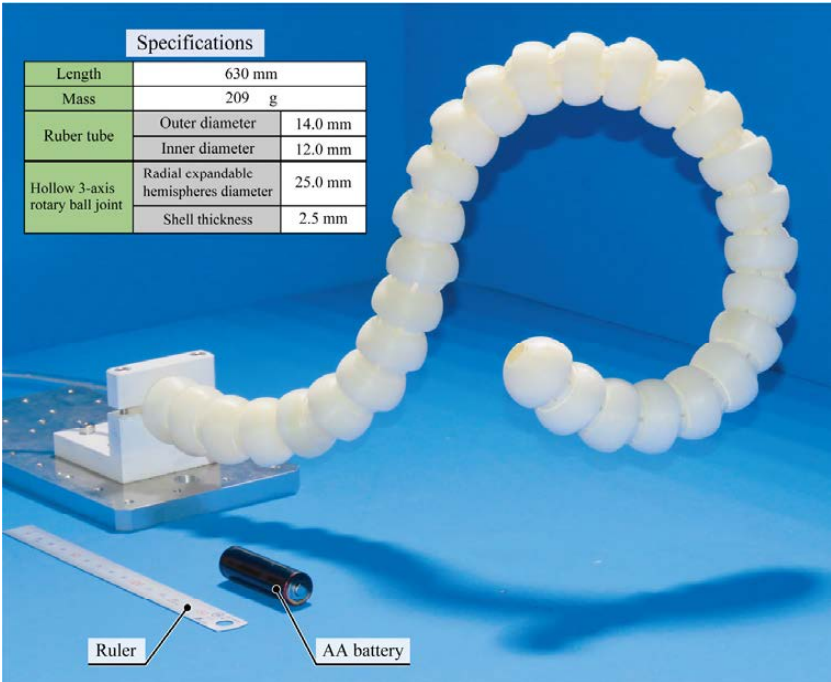


Fig. 23 Prototype of the proposed mechanism and prototype specifications. The joints and levers are made of acrylic resin and are manufactured using a 3D printer (AGILISTA, Keyence, Japan).

This chapter explains the design method of the proposed mechanism's joints based on the interaction of a theoretical model, finite element modeling with non-linear analysis, and actual measurements. The theoretical and experimental values of the performance, assemblability, and limitations of critical parameters were evaluated, such as whether the expandable hemisphere fits into the shell, whether the expandable hemisphere dislocates from the shell during pressurization, and the joint holding torque.

Using a theoretical model of the torque required to lock the joint angle, I simulated the holding torque using finite element modeling analysis and measured the holding torque in the pitch and roll direction when internal pressure was applied. Based on the interaction of the theoretical model, measurement, and FEM analysis, I evaluated the theoretical, measured, and FEM value of the holding torque by performing pairwise numerical comparisons.

## **Section II.2 The basic principle of the proposed variable stiffness mechanism with single rubber tube and 3-axis rotary ball joints.**

### **Subsection II.2.1 The design method of pressure driven variable stiffness mechanism.**

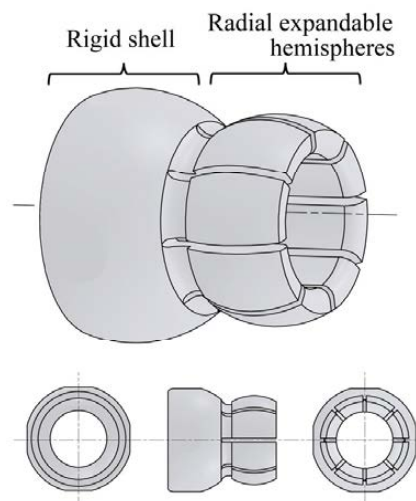
Previous research has been conducted on positive-pressurization methods, such as rescue manipulator [114], tubular jammed beam [115], and tool holding articulated arm [86], pressure-driven manipulator [87]. Rescue manipulator [114] uses a semicircular duplex mechanism to propel itself in an arbitrary direction. However, the robot consists of numerous parts and has a complex structure. Tubular jammed beams [115] and multiple tubes have been placed inside a thin-walled pipe and expanded to increase the stiffness through contact between the tubes. The principles and structures are simple; however, when the tube is expanded, its shape becomes straightened. Tool holding articulated arm [86] becomes highly rigid by contacting the ball joint, presser, and housing pushed by the spring when no pressure is applied. When pressure is applied, the arm becomes flexible as it does not contact these parts. However, this arm has a complicated structure and sliding resistance because it contains an air cylinder. Pressure-

driven manipulator [87] comprises a link structure that connects single-axis rotary joints, and the structure becomes highly rigid owing to the friction between the rubber chamber and rigid walls. However, this mechanism includes only one degree of freedom for the joints and uses multiple chambers.

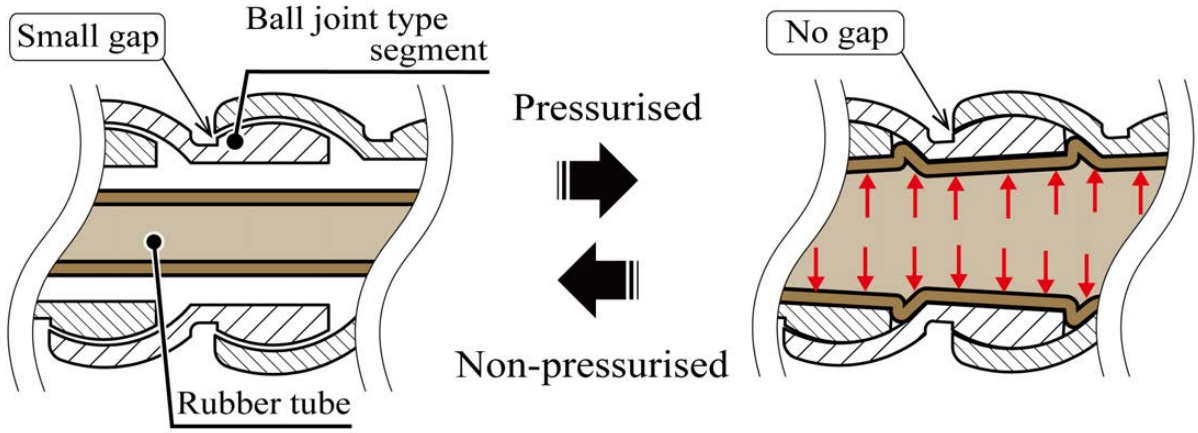
In this study, I devised a variable stiffness mechanism via frictional force using positive pressure with a 3-axis rotary joint and a single chamber. The proposed mechanism has an articulated structure based on a linked 3-axis rotary joint that can deform freely when internal pressure is not applied and achieves high stiffness when internal pressure is applied. For the joint shape in proposed method, only a hollow male-female joint structure is required. Although the number of joints increases with the total length of the structure, the only components required to form an articulated structure were the joints, chambers, and fittings to keep the chambers sealed.

The 3-axis rotary ball joint of the proposed mechanism is shown in Fig. 24 The ball joints have a hemispherical rigid shell and a radial expandable hemisphere with slits in the longitudinal direction. This shape simplifies the structure when the ball joint is assembled. The shell cannot be deformed, thereby preventing the rubber tube from being damaged by sharp external objects.

Fig. 25 shows the working principle of the proposed mechanism. This mechanism has a linked structure with 3-axis rotary ball joints and an enclosed rubber tube that passes through the structure. The expandable hemisphere is deformed by pressurizing the enclosed rubber tube, and contact pressure is obtained between the expandable hemisphere and shell.



**Fig. 24 3-axis rotary ball joint with slits design of the proposed method.**



**Fig. 25** Principle of the proposed method for variable stiffness. The radial expandable hemispheres don't contact to shell when no pressure. The expandable hemisphere is deformed by pressurizing the enclosed rubber tube, and contact pressure is obtained between the expandable hemisphere and shell.

## Subsection II.2.2 Theoretical model of the expandable hemisphere that can be fitted to the shell.

Here, I explain the model of the expandable hemisphere and shell. Fig. 25(i) shows a cross-sectional view of the expandable hemisphere before fitting it into the shell. Here,  $L$  is the total length of the expandable hemisphere,  $a$  is the length of the base of the expandable hemisphere,  $b$  is the length of the contact area between the expandable hemisphere and the shell,  $r_0$  is the outer radius of the expandable hemisphere at  $a \leq x \leq L$ ,  $r_0'$  is the inner radius of the expandable hemisphere;  $\theta_2$  ( $0 \leq \theta_2 \leq \pi/2$ ) is the angle to contact point A, and  $\theta_1$  is the range from the central axis to the tip of the expandable hemisphere.

When the shell is fitted onto the expandable hemisphere, I assume that the shell is a rigid body and that the shell and expandable hemisphere come into contact at point A, as shown in Fig. 26. As the shell slides further, the expandable hemisphere is deformed, and the edge of the shell reaches point A'. Because the cross-sectional shape of the contact area between the expandable hemisphere and the shell is axisymmetric, the angle to point A' is  $\theta_2$ , as shown in Fig. 25(ii).

I consider a stepped cantilever deflected by a concentrated load  $F$  applied to point A (Fig. 27). For the expandable hemisphere to fit into the shell, the deflection  $\delta$  at  $x = a + b/2$  must be larger than  $r_0(1 - \sin\theta_2)$ . The distance to point A is  $a + (b/2) + r_0 \cos\theta_2 = t$ , moment of inertia of area  $0 \leq x \leq a$  is  $I_1$ , and moment of inertia of area  $a \leq x \leq L$  is  $I_2$ .

Because the moment of inertia of area  $I_2$  is non-uniform, I must consider it as a function of  $x$ . To obtain  $I_2$ , I consider the cross-section of the stepped cantilever at an arbitrary point  $x = a + (b/2) + r_0 \cos \theta$ , as shown in Fig. 28. The range of  $\theta$  is  $\theta_1 \leq \theta \leq \pi/2$ . Here,  $r$  is the radius to the differential area,  $\alpha$  is the angle to the differential area on the  $y-z$  plane,  $\alpha_1$  is the angle to the edge of the cantilever on the  $y-z$  plane,  $h_2$  is the distance to the neutral axis, and  $y_2$  is the distance from the neutral axis to the differential area, and can be represented as follows.

$$y_2 = r \sin \alpha - h_2 . \tag{1}$$

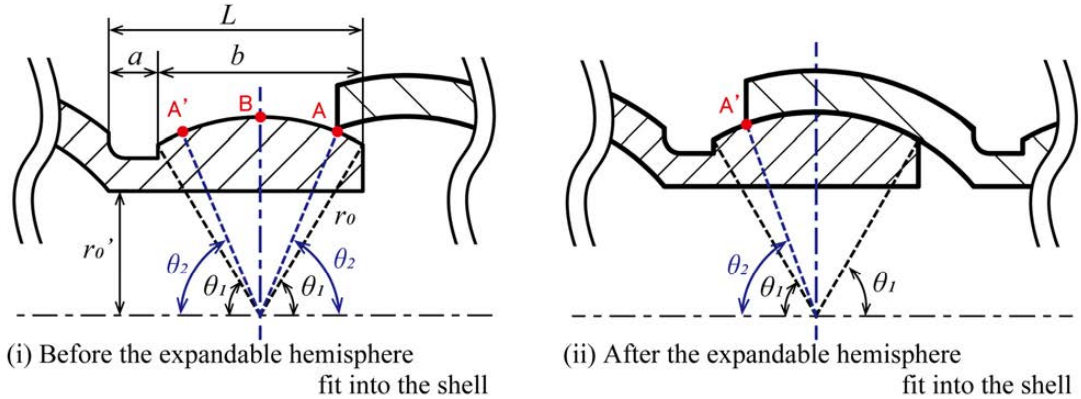


Fig. 26 Fitting of expandable hemisphere on shell.

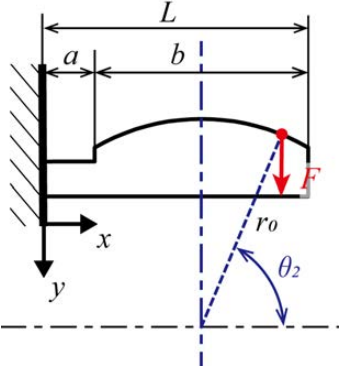


Fig. 27 Stepped cantilever under concentrated load.

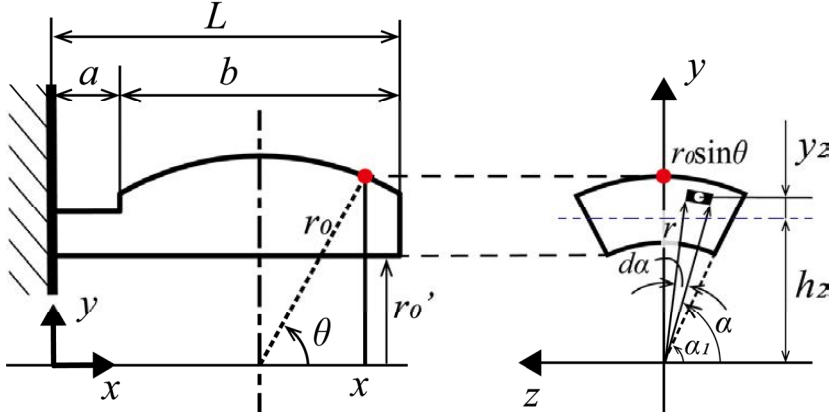


Fig. 28 Moment of inertia of area  $I_2$ .

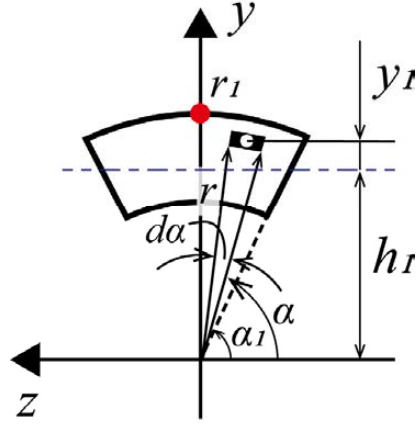


Fig. 29 Moment of inertia of area  $I_1$ .

To obtain the moment of inertia of area  $I_2$  at an arbitrary point,  $\theta$  is converted to  $x$  as follows.

$$\theta = \cos^{-1} \left( \frac{x - a - \frac{b}{2}}{r_0} \right). \quad (2)$$

Next, the moment of inertia of the area  $I_{z2}$  about the  $z$ -axis is calculated as follows:

$$I_{z2} = 2 \int_{\alpha_1}^{\frac{\pi}{2}} \int_{r_0'}^{r_0 \sin \theta} (r \sin \alpha)^2 \cdot r \cdot d\alpha \cdot dr. \quad (3)$$

Additionally, the cross-sectional area  $A_2$  at  $a \leq x \leq L$  is as follows.

$$A_2 = \pi(r_0^2 \sin^2 \theta - r_0'^2) \frac{\pi - 2\alpha_1}{2\pi}. \quad (4)$$

The distance  $h_2$  to the neutral axis is obtained as follows.

$$2 \int_{\alpha_1}^{\frac{\pi}{2}} \int_{r_0'}^{r_0 \sin \theta} (r \sin \alpha - h_2) \cdot r \cdot d\alpha \cdot dr = 0. \quad (5)$$

From these equations, the moment of inertia of area  $I_2$  about the neutral axis is expressed by the parallel-axis theorem, as follows:

$$I_2 = I_{z2} - h_2^2 A_2. \quad (6)$$

Similarly, the moment of inertia of area  $0 \leq x \leq a$  is  $I_1$  shown in Fig. 28 is as follows.

$$y_1 = r \sin \alpha - h_1, \quad (7)$$

$$I_{z1} = 2 \int_{\alpha_1}^{\frac{\pi}{2}} \int_{r_0'}^{r_1} (r \sin \alpha)^2 \cdot r \cdot d\alpha \cdot dr, \quad (8)$$

$$A_1 = \pi(r_1^2 - r_0'^2) \frac{\pi - 2\alpha_1}{2\pi}, \quad (9)$$

$$2 \int_{\alpha_1}^{\frac{\pi}{2}} \int_{r_0'}^{r_1} (r \sin \alpha - h_1) \cdot r \cdot d\alpha \cdot dr = 0 , \quad (10)$$

$$I_1 = I_{z1} - h_1^2 A_1 . \quad (11)$$

where  $y_l$  is the distance from the neutral axis to the differential area,  $r_l$  is the outer radius of the expandable hemisphere at  $0 \leq x \leq a$ ,  $I_{zl}$  is the moment of inertia of the area,  $A_l$  is the cross-sectional area at  $0 \leq x \leq a$ , and  $h_l$  is the distance to the neutral for  $0 \leq x \leq a$  and  $a \leq x \leq t$ , respectively, are expressed below.

$$\frac{d^2 y}{dx^2} = \frac{F}{EI_1} (t - x) \quad (0 \leq x \leq a) , \quad (12)$$

$$\frac{d^2 y}{dx^2} = \frac{F}{EI_2} (t - x) \quad (a \leq x \leq t) , \quad (13)$$

where  $E$  is Young's modulus. Here, the 5th order Taylor expansion is calculated around  $x=a$  to reduce the computational cost of the differential equation of deflection for  $a \leq x \leq t$ .  $x=a$  is used as an expansion point because of the boundary of the stepped beam, and the deformation at this point must be accurately estimated. The accuracy of the approximate deformation of the beam near  $x = L$  is not critical.

Additionally, the boundary condition is as follows.

$$y = 0 \quad (x = 0) , \quad (14)$$

$$\frac{dy}{dx} = 0 \quad (x = 0) , \quad (15)$$

$$\frac{dy}{dx}|_{x=a-0} = \frac{dy}{dx}|_{x=a+0} , \quad (16)$$

$$y|_{x=a-0} = y|_{x=a+0} . \quad (17)$$

From the boundary conditions,  $F$  can be calculated when the deflection is  $\delta = r_0(1 - \sin\theta_2)$  at  $x = a + (b/2)$ . Consequently, the bending stress  $\sigma$  owing to the maximum bending moment  $M_{max} (x = 0)$  at  $F$  is obtained. Bending stress  $\sigma$  is expressed as follows:

$$\sigma = \frac{M_{max}}{I_1} (r_1 - h_1) = \frac{Ft}{I_1} (r_1 - h_1) . \quad (18)$$

From (18), it can be inferred that the expandable hemisphere can fit into the shell without breaking if the maximum bending allowable stress  $\sigma'$  is not exceeded.



Specifically,  $\theta_2$  ( $0 \leq \theta_2 \leq \pi/2$ ) should be greater than a specific threshold value for the shell to fit without breaking the expandable hemisphere.

### **Subsection II.2.3 Theoretical model of expandable hemisphere that does not dislocate from the shell when pressurized.**

Here, the mechanism of the expandable hemisphere dislocates from the shell is explained. When pressurized with the expandable hemisphere fitted in the shell, expansion forces are generated in the radial and axial directions of the rubber tube at the contact point A' in Fig. 30. If the expandable hemisphere has no stiffness, the following conditions must be fulfilled to prevent the shell from dislocating owing to the expansion force:

$$\mu(PS\sin\theta_2 + T \cos \theta_2) + PS \cos \theta_2 > T \sin \theta_2 , \quad (19)$$

$$\mu(PS\sin\theta_2 + PS' \cos \theta_2) + PS \cos \theta_2 > PS' \sin \theta_2 . \quad (20)$$

where,  $\mu$  is the static friction coefficient,  $P$  is the internal pressure,  $T$  is the expansion force in the axial direction,  $\theta_2$  is the range of the shell covering the expandable hemisphere,  $S$  is the pressure area in the radial direction, and  $S'$  is the pressure area in the axial direction. The pressure areas  $S$  and  $S'$  are expressed as follows:

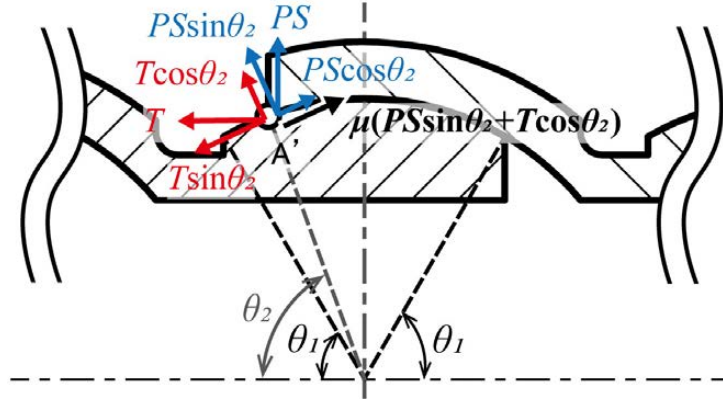
$$S = 2\pi r_0' L , \quad (21)$$

$$S' = r_0^2 \sin^2 \theta_1 \pi . \quad (22)$$

$r_0'$  is the inner radius of the expandable hemisphere,  $L$  is the total length of the expandable hemisphere,  $r_0$  is the outer radius of the expandable hemisphere at  $a \leq x \leq L$ ,  $\theta_1$  is the range from the central axis to the tip of the expandable hemisphere. The force in the radial direction is determined by the pressure area of the radial expandable hemisphere, including the slits. The axial direction force is determined by the pressure area of the air plug and the inner sphere of the shell.

If the expansion in the radial and axial directions of the rubber tube and the deformation in the expandable hemisphere are minimized, it can be assumed that there is no internal pressure loss owing to these deformations.

From (20), if the frictional and radial tangential forces are larger than the tangential force in the axial direction, the expandable hemisphere will not



**Fig. 30 Expansion force at the contact point A'.**

dislocate.

However, because (20) does not consider the stiffness of the expandable hemisphere, it can be inferred that the limit values of the internal pressure and the range of the shell when the expandable hemisphere does not dislocate are greater than the theoretical values. Therefore, in addition to the theoretical model, I use the FEM and prototype to discuss the prevention of expandable hemisphere dislocation from the shell considering the stiffness in subsection II.3.1, II.3.2 and II.4.1.

## **Subsection II.2.4 Theoretical model of holding torque in the pitch and roll directions.**

I constructed a model to calculate the theoretical values of holding torque in the pitch and roll directions. The normal directional force on the differential area of the shell is calculated (Fig. 31). The distance from the center of rotation of the joint to the differential area is  $r_0$ . The angle around the  $z$ -axis is  $\theta$ , while that around the  $x$ -axis is  $\beta$ .

The holding torques in the pitch and roll directions are  $\tau_1$  and  $\tau_2$ , respectively; the distances to the rotation center of these torques are different. The radius  $r_z$  to the differential area on the circumference of radius  $r_0 \sin \theta$  and the radius  $r_x$  to the differential area on the circumference of radius  $r_0$  in Fig. 30 are as follows:

$$r_z = r_0 \sqrt{\sin^2 \theta \sin^2 \beta + \cos^2 \theta}. \quad (23)$$

$$r_x = r_0 \sin \theta. \quad (24)$$

(23) and (24) indicate the distance to the rotation center of the holding torque in the pitch and roll directions, respectively.

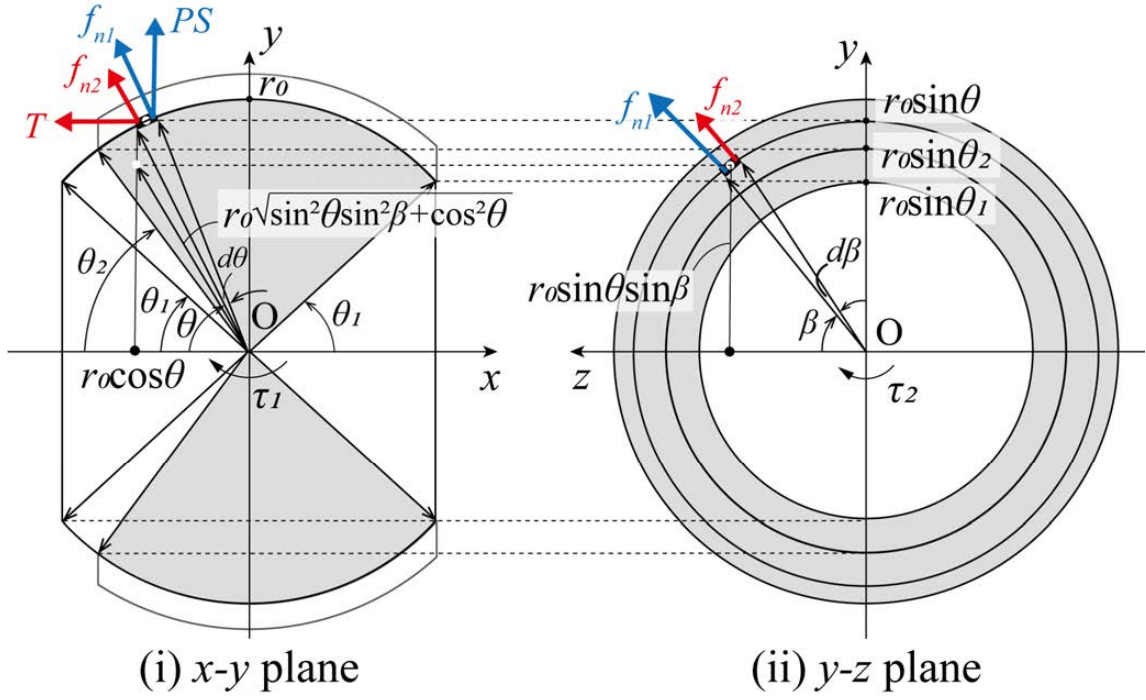


Fig. 31 Normal force on differential area of joint shell.

$f_{n1}$  and  $f_{n2}$  are the normal forces obtained from the radial and axial forces in a differential area, respectively. At this time, the tangential force caused by the expansion of the rubber tube cancels out; thus, it does not affect the holding torque.

The expansion force in the radial direction of the rubber tube is assumed to be transmitted in the vertical upward direction. The expansion force of the rubber tube in the radial direction is transmitted to the shell on a spherical surface within the range of  $\theta_2 \leq \theta \leq \pi - \theta_1$  and  $0 \leq \beta \leq \pi/2$ . The expansion force in the axial direction is transmitted to the shell within the range of  $\theta_2 \leq \theta \leq \pi/2$  and  $0 \leq \beta \leq \pi/2$ .

The expansion force in the radial direction  $f_{n1}$  and the expansion force in the axial direction  $f_{n2}$  are obtained as follows.

$$f_{n1} = PS \sin \theta , \quad (25)$$

$$f_{n2} = T \cos \theta = PS' \cos \theta . \quad (26)$$

From (25) and (26), the stresses  $\sigma_1$  and  $\sigma_2$ , which are forces per unit area in the radial and axial directions, are as follows.

$$\sigma_1 = \frac{f_{n1}}{4 \int_0^{\pi/2} \int_{\theta_2}^{\pi - \theta_1} r_0 d\theta \cdot r_0 \sin \theta d\beta} , \quad (27)$$

$$\sigma_2 = \frac{f_{n2}}{4 \int_0^{\pi/2} \int_{\theta_2}^{\pi} r_0 d\theta \cdot r_0 \sin \theta d\beta} . \quad (28)$$

From (23) to (28), the holding torques  $\tau_l$  in the pitch direction and  $\tau_2$  in the roll direction are expressed by

$$\begin{aligned} \tau_1 = 4 \int_0^{\frac{\pi}{2}} \int_{\theta_2}^{\pi-\theta_1} \mu \sigma_1 \cdot r_0 \sqrt{\sin^2 \theta \sin^2 \beta + \cos^2 \theta} \cdot r_0 d\theta \cdot r_0 \sin \theta d\beta \\ + 4 \int_0^{\frac{\pi}{2}} \int_{\theta_2}^{\frac{\pi}{2}} \mu \sigma_2 r_0 \sqrt{\sin^2 \theta \sin^2 \beta + \cos^2 \theta} \cdot r_0 d\theta \cdot r_0 \sin \theta d\beta. \end{aligned} \quad (29)$$

$$\begin{aligned} \tau_2 = 4 \int_0^{\frac{\pi}{2}} \int_{\theta_2}^{\pi-\theta_1} \mu \sigma_1 \cdot r_0 \sin \theta \cdot r_0 d\theta \cdot r_0 \sin \theta d\beta \\ + 4 \int_0^{\frac{\pi}{2}} \int_{\theta_2}^{\frac{\pi}{2}} \mu \sigma_2 \cdot r_0 \sin \theta \cdot r_0 d\theta \cdot r_0 \sin \theta d\beta. \end{aligned} \quad (30)$$

In particular, (29) and (30) indicate that the holding torque in the roll direction is approximately 1.41 times larger than that in the pitch direction.

## Section II.3 Mechanism design of the proposed variable stiffness mechanism with single rubber tube and 3-axis rotary ball joints.

### Subsection II.3.1 Design method of 3-axis rotary ball joint.

In this subsection, based on the theoretical models presented in Subsections II.2.2 and II.2.3, I discuss the design of a joint that can be assembled, and that is not dislocated when a positive pressure is applied. In this paper, the joints were machined using MC nylon (MC901) because of its high dimensional stability, high mechanical strength, abrasion resistance, and high toughness.

First, based on the theoretical model discussed in Subsection II.2.2, I determined the shell range  $\theta_2$  for designing a joint that could be assembled. Table III lists all the parameters necessary to design the joint. The result of calculating the shell range  $\theta_2$  using the parameters shown in Table I and the numerical analysis software ‘‘MATLAB’’ is as follows.

$$\theta_2 = 64.22 \text{ [deg]}. \quad (31)$$

Here,  $\theta_2$  must be larger than the value in (31) to design a joint that can be assembled. Therefore, I set  $\theta_2$  to 65 degrees, considering the reliability of the assembly and because the movable range of the joint and the maximum angle of  $\theta_2$

**TABLE III**  
**PARAMETERS FOR DESIGNING 3-AXIS ROTARY BALL JOINT.**

Total length of the expandable hemisphere	$L$ [mm]	15.5
Length of the base of the expandable hemisphere	$a$ [mm]	3.0
Length of the contact area	$b$ [mm]	12.5
Outer radius of the expandable hemisphere	$r_o$ [mm]	12.5
Inner radius of the expandable hemisphere	$r_o'$ [mm]	8.0
Range from the central axis to the tip of the expandable hemisphere	$\theta_1$	$\pi/3$
Angle to the edge of the cantilever on the yz plane	$\alpha_1$	$3\pi/8$
Outer radius of the expandable hemisphere at $0 \leq x \leq a$	$r_1$ [mm]	10.0
Young's modulus	$E$ [MPa]	3530
Maximum bending allowable stress	$\sigma'$ [MPa]	110
Coefficient of static friction	$\mu$	0.1735
Pressure area in the radial direction	$S'$ [mm <sup>2</sup> ]	779.1
Pressure area in the axis direction	$S'$ [mm <sup>2</sup> ]	368.2

are  $\pi/2$ .

Additionally, I substituted the determined  $\theta_2$  into (20) in II.2.3 and examined whether the expandable hemisphere dislocates from the shell at internal pressures of 0.1 MPa, 0.2 MPa, and 0.3 MPa. I confirmed that the left side of (20) was greater than its right side at all internal pressures. Therefore, the shell range  $\theta_2$  in this paper is 65 degrees.

### **Subsection II.3.2 Design method of the prototype of the proposed mechanism.**

This subsection explains the assembly method of the prototype for the proposed mechanism. This prototype is used for evaluating whether the expandable hemisphere fits into the shell, whether the expandable hemisphere dislocates from the shell during pressurization, and the joint holding torque.

Fig. 32(a) shows the 3-axis rotary ball joint based on Subsection II.3.1 and Table I. The shell thicknesses of the joints in this paper are 2.5 mm. Eight expandable hemispheres are required to unify the arrangement of the expandable hemispheres in both the pitch and yaw directions. The gap between the expandable hemispheres is 1 mm, which is the same thickness of the rubber tube used. Additionally, the gap between the expandable hemisphere and the shell is 0.1 mm.



(a) 3-axis ball joint



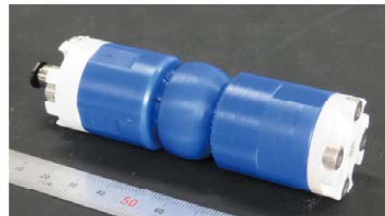
(b) Rubber tube



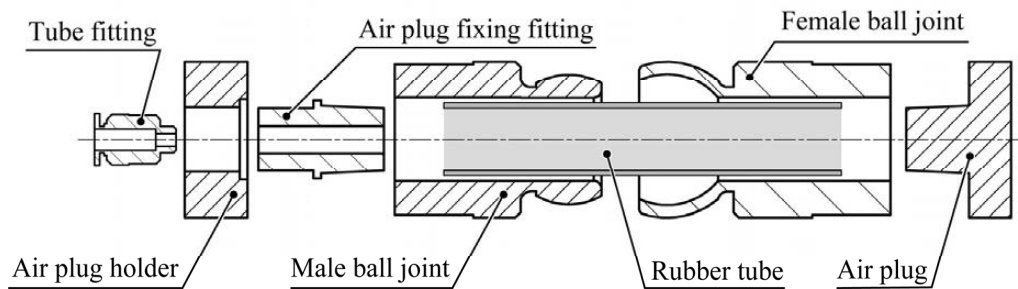
(c) Air plug (tip side)



(d) Air plug (root side)



(e) Experimental unit



(f) Assembly method of the experimental unit

**Fig. 32** Parts and assembly of prototype for the proposed method. (a) 3-axis rotary ball joint based on Subsection II.3.1 and Table I. (b) Rubber tube is made of Ecoflex 00-50. (c)-(d) Air plugs for gluing the ends of the rubber tube. (e) Experimental unit for evaluating whether the expandable hemisphere fits into the shell, whether the expandable hemisphere dislocates from the shell during pressurization, and the joint holding torque. (f) Assembly method of the experimental unit.

The rubber tube (Fig. 32(b)) has outer and inner diameters of 14 mm and 12 mm, respectively, and a thickness of 1 mm. This is because the inner diameter of the expandable hemisphere is 16 mm, and the pressure loss owing to the expansion of the rubber tube is ignored. The rubber tube is made of Ecoflex 00-50, the same material and fabrication as the rubber tube used in [87].

The air plug (Fig. 32(c) and (d)) for gluing the ends of the rubber tube consists of

a taper. The diameters of the tapered tip and tapered root are 12 mm and 13 mm, respectively, and the length of the tapered part is 12 mm. The plugs are made of resin-containing glass (Rigid 10 K) and manufactured using stereolithography (Formlabs, Form 3, USA). The plug on the root side is divided into two parts for ease of assembly.

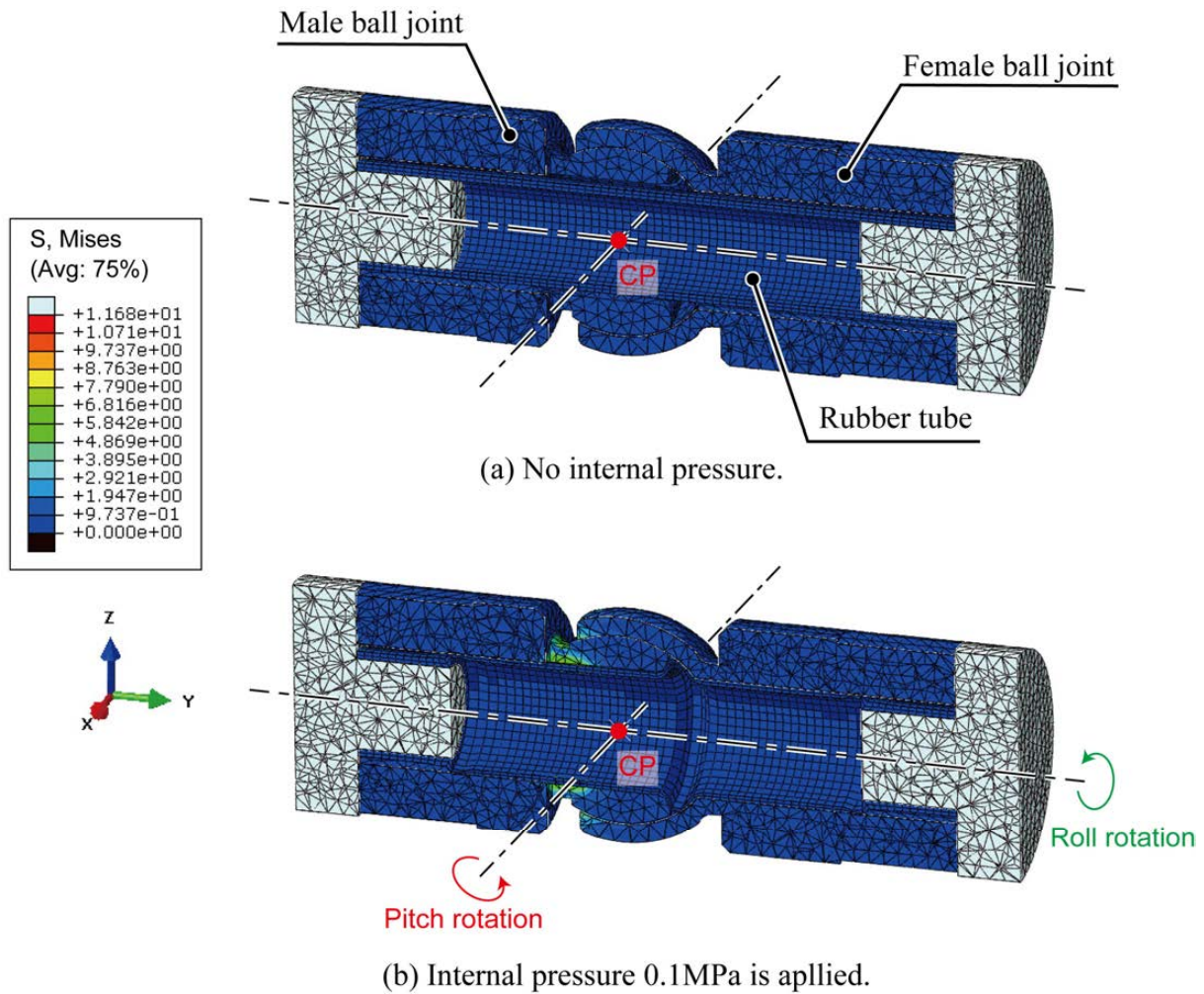
The assembly method for the experimental unit is shown in Fig. 32(e) and (f). The tip and root air plugs are glued to a rubber tube. A rubber tube with an air plug is inserted into the female joint, and the air plug is connected to the female joint. The male joint fits into the female joint. Finally, the root air plug is inserted into the holder and the tube fitting is fixed to the root air plug. The expandable hemisphere of the male joint was not broken when the experimental setup was assembled. In addition, the expandable hemisphere of the male joint was not dislocated from the shell of female joint when 0.2 MPa is applied.

## **Section II.4 Simulation and experiment of the proposed variable stiffness mechanism with single rubber tube and 3-axis rotary ball joints.**

### **Subsection II.4.1 Simulation of holding torque using finite element analysis.**

In this subsection, I performed a finite element analysis using Abaqus/CAE (Dassault Systems, France) to evaluate the holding torque obtained using the proposed mechanism, including the rubber tube. A 3D model was created using Abaqus to compare the theoretical model values with the actual measured values. The joint and rubber tubes were of the same scale as the model used in the experiment. However, the air plug used a model without a taper to constrain it using a rubber tube. The diameter of the constraining part of the air plug was 12 mm, which is the same as the inner diameter of the rubber tube.

I explain the definitions of the joints and rubber tubes in Abaqus. The material of the joint and air plug is MC nylon (MC901), and according to the datasheet, Young's modulus and Poisson's ratio are 3530 MPa and 0.4, respectively. The material of the rubber tube is Ecoflex 00-50, which is defined by the 3rd order of the Ogden hyper elastic model from the material parameters in [87].



**Fig. 33** 3D experimental setup in FEM simulations for evaluating the holding torque. To obtain holding torque in pitch direction, rotate female joint around the CP in the  $x$ -axis. To output holding torque in the roll direction, rotate female joint around the CP in  $y$ -axis.

The coefficient of static friction between MC nylon (MC901) is 0.1735, and the coefficient of static friction between MC nylon (MC901) and Ecoflex 00-50 is 1.431. These values are measured according to the ISO 15113:2005 (Rubber - Determination of frictional properties) standard (Procedure A).

Internal pressures of 0.1, 0.125, 0.15, 0.175, and 0.2 MPa are applied to the inner wall of the rubber tube and the air plug constraining the rubber tube, and then obtained the joint holding torque from the radial and axial forces. After confirming the prevention of expandable hemisphere dislocation from the shell, the female joint was rotated at a maximum angle of  $5^\circ$  in the pitch and roll directions, and the maximum value of the moment around the central point (CP) for rotation was the output (Fig. 33). The FEM values are shown in Subsection II.4.2 along with the theoretical and measured values.



## Subsection II.4.2 Measuring the holding torque in the pitch and roll directions.

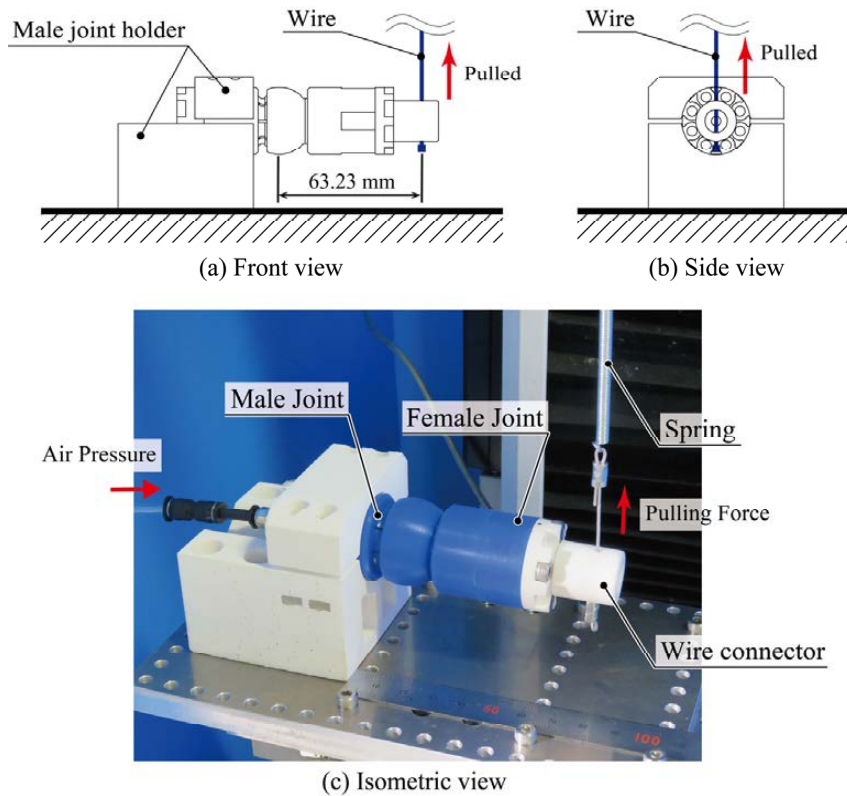
In this subsection, I present the measurements of the holding torque in the pitch and roll directions for comparison with theoretical and FEM values. Fig. 34 and Fig. 35 show the devices used to measure the holding torque in the pitch and roll directions, respectively.

I measured the tensional force in the pitch and roll directions when the wire connector was rotated to measure the maximum static friction force when using an experimental setup. In this experiment, the wire connector was pulled by a wire with a spring that was tied to a tensile testing machine (Model 3343, INSTRON, Japan) when internal pressure was applied. The pulling force at each internal pressure was measured five times, and the average values of the friction force were obtained accordingly. The holding torque was calculated by multiplying the obtained maximum static friction force value and the length from the center of rotation to the tip of the wire connector. The wires used in the experiments were made of stainless steel. A high-precision regulator (IR1020-01, ISE30A-01, SMC, Japan) was used to control the internal pressure.

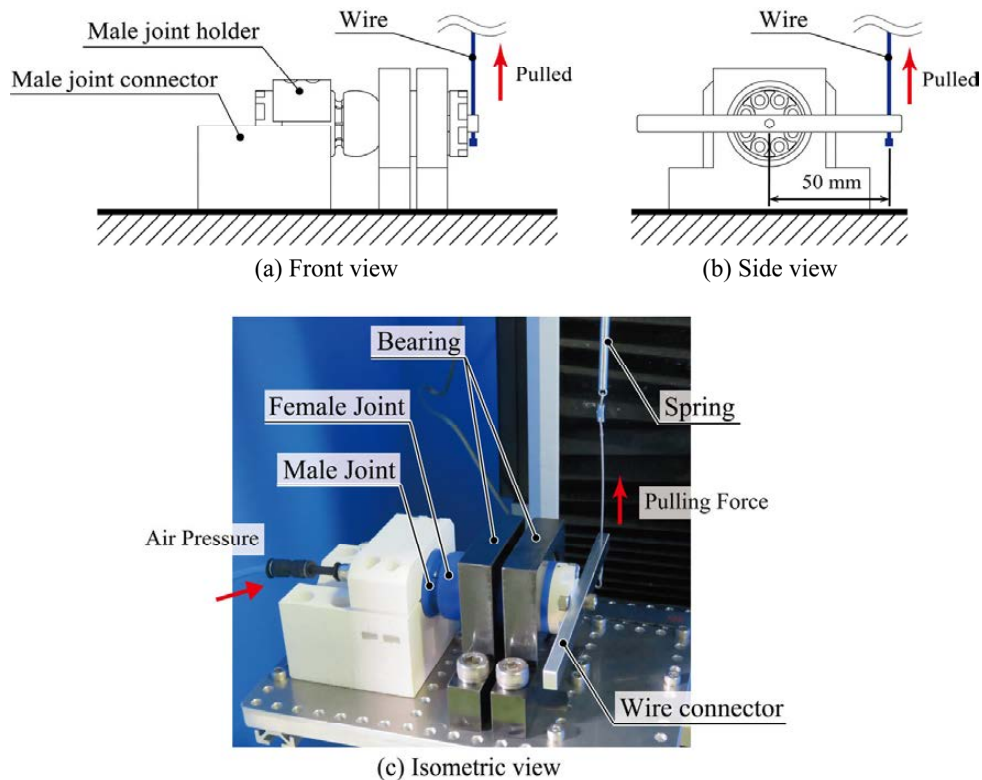
Experimental conditions:

- The applied pressures were 0.1, 0.125, 0.15, 0.175, and 0.2 MPa.
- The moment arm lengths were 63.23 mm in the pitch direction and 50 mm in the roll direction, as shown in Fig. 33 and Fig. 34, respectively.
- The pulling velocity was 30 mm/min.
- The product number of the spring used was 3.96 × 79.3 of the 200PC SPRING ASSORTMENT. The spring constant was determined to be 0.783.
- The maximum pulling extension was 10 mm to measure the maximum static friction force in the pitch and roll directions.

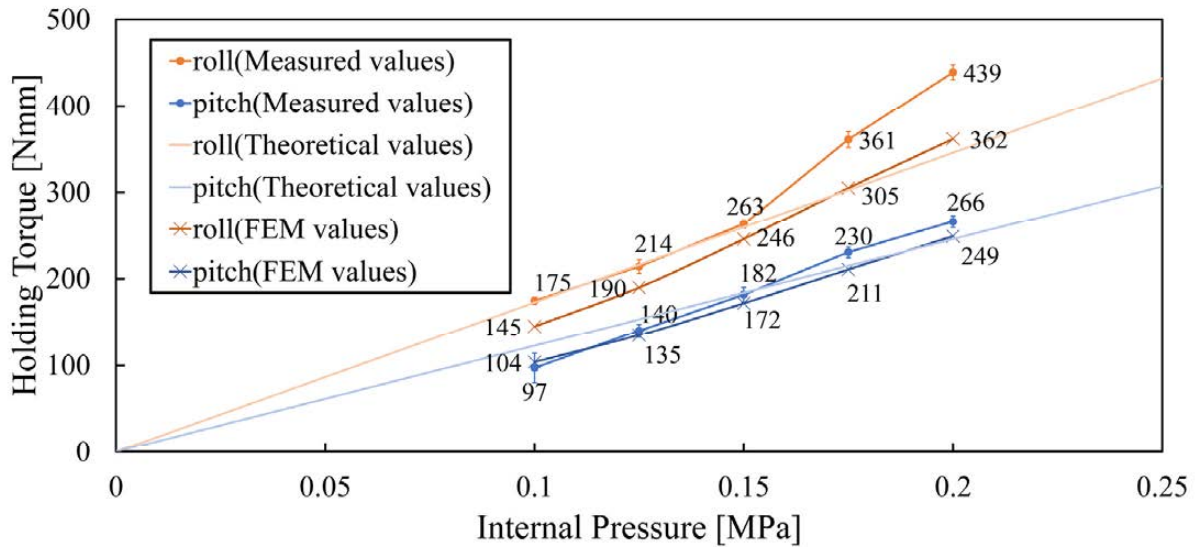
Fig. 36 shows the theoretical, FEM, and measured values of the holding torque in the pitch and roll directions for each internal pressure. Tables III and IV show the magnified FEM values between the pitch and roll directions and the magnification of the measurement values between the pitch and roll directions, respectively. Tables V and VI present the error values between the measured and FEM values as well as the measured and theoretical values, respectively.



**Fig. 34** Experimental setup for measuring the holding torque in the pitch direction. This setup offset the moments due to the weight of the arm from the measured value. Holder and connector are made of resin containing glass (Rigid 10K) and are manufactured using stereolithography (Formlabs, Form 3, USA).



**Fig. 35** Experimental setup for measuring the holding torque in the roll direction. Wire connector is made of machined duralumin (A2017).



**Fig. 36** Results of theoretical, FEM and measured values of holding torque in pitch and roll directions. The error bar indicates the standard deviation of the measured value.

**TABLE IV**

**MAGNIFICATION OF HOLDING TORQUE IN PITCH AND ROLL DIRECTION AT EACH INTERNAL PRESSURE ON FEM SIMULATION.**

Internal pressure [MPa]	0.1	0.125	0.15	0.175	0.2
Magnification of holding torque	1.40	1.41	1.43	1.45	1.45

**TABLE V**

**MAGNIFICATION OF HOLDING TORQUE IN PITCH AND ROLL DIRECTION AT EACH INTERNAL PRESSURE ON MEASUREMENT.**

Internal pressure [MPa]	0.1	0.125	0.15	0.175	0.2
Magnification of holding torque	1.80	1.53	1.45	1.57	1.65

**TABLE VI**

**ERROR VALUES OF HOLDING TORQUE IN PITCH AND ROLL DIRECTIONS BETWEEN MEASURED AND FEM VALUES.**

Internal pressure [MPa]	0.1	0.125	0.15	0.175	0.2
Error in the pitch direction [%]	6.5	3.8	5.7	9.4	6.8
Error in the roll direction [%]	20.3	12.6	7.1	18.4	21.4

**TABLE VII**

**ERROR VALUES OF HOLDING TORQUE IN PITCH AND ROLL DIRECTIONS BETWEEN MEASURED AND THEORETICAL VALUES.**

Internal pressure [MPa]	0.1	0.125	0.15	0.175	0.2
Error in the pitch direction [%]	21.0	8.6	1.2	7.3	8.3
Error in the roll direction [%]	1.2	0.97	1.4	19.3	27.0

In the theoretical model, the magnification between the holding torques in the pitch and roll directions is approximately 1.41 times, Table IV indicates that the FEM values of the holding torque in the roll direction are on average 1.43 times larger than those in the pitch direction. Table V indicates that the measured values of the holding torque in the roll direction are on average 1.60 times larger than those in the pitch direction.

Table VI shows that the average errors between the measured and FEM values were approximately 6.5 % and 16.0 % in the pitch and roll directions, respectively.

Table VII shows that the average errors between the measured and theoretical values were approximately 9.3 % and 10.0 % in the pitch and roll directions, respectively. Therefore, the results in Section II.4 show that the theoretical, measured, and FEM values are similar.

## **Section II.5      Discussion of Chapter II.**

The rubber tube inside the structure may become twisted owing to the rotation of the ball joint in the rolling direction in the absence of pressure. Therefore, it is necessary to suppress rotation in the roll direction through geometrical constraints, for example, by placing a pin on the surface of the joint or covering it with a rubber membrane. However, it should be ensured that the maximum radius of curvature in the pitch direction is not decreased.

As the positive-pressurized mechanism in this study encloses a rubber tube, it has an extension effect in addition to the effect on the holding torque during pressurization. The soft actuator utilized the extension action generated by pressurizing each of the multiple chambers. Hence, it may be possible to change the characteristics of the mechanism by varying the material, shape, number, and arrangement of the chambers to be enclosed and adding the function of active extension in addition to variable stiffness.

Contrary to the tubes and airbags, the proposed mechanism does not form a linear shape when pressurized. When a nonstretchable tube is pressurized, it approaches a linear state corresponding to the maximum volume. In contrast, in the proposed mechanism, the internal volume of the rubber tube is constant regardless of the joint angle; thus, the fluid pressure does not generate torque

around the joint angle. Although the fluid does not affect the rotation, the bending moment caused by the rubber tube material increases as the joint angle increases.

## **Section II.6 Conclusion of Chapter II.**

Chapter II presents a design method of variable stiffness mechanism with a ball joint with slits and rubber tubes that switches stiffness under positive pressure. The design method of the proposed mechanism's joints is constructed by the interaction of a theoretical model, finite element modeling with non-linear analysis, and actual measurements.

First, the theoretical and experimental values of the assemblability, and limitations of critical parameters were evaluated, such as whether the expandable hemisphere fits into the shell, whether the expandable hemisphere dislocates from the shell during pressurization. The design method of ball joints in this chapter allows that the expandable hemisphere of ball joints can fit into the shell without breaking the expandable hemisphere and the expandable hemisphere of male joint was not dislocated from the shell of female joint when 0.2 MPa is applied.

Moreover, using a theoretical model of the torque required to lock the joint angle, the holding torque is simulated by using the FEM and measured the holding torque in the pitch and roll directions when the actual pressure was applied. It was confirmed that the holding torque in the roll direction was approximately 1.41 times larger than that in the pitch direction for each value of internal pressure. This magnification can potentially be applied to other methods that use a 3-axis rotary joint. Furthermore, I also evaluated the FEM, theoretical and measured value of holding torque by numerical comparison.

In the future, I believe that this mechanism can be developed and applied in a wide range of fields. A potential application in the medical field is the use of guide endoscopes to design the structure of the proposed mechanism such that it is actively bendable (e.g., using the wire-driven method).

## Chapter III

# Tube Mechanism to Achieve Positive- Pressurization Variable Stiffness by Lever and Wire

# **Chapter III Tube Mechanism to Achieve Positive-Pressurization Variable Stiffness Mechanism by Lever and Wire**

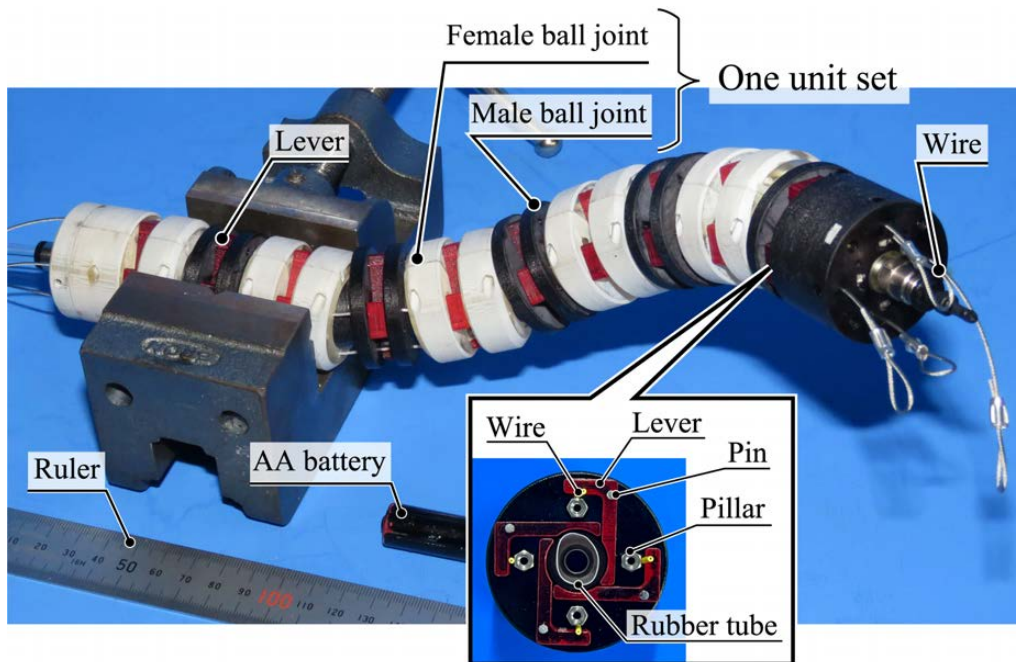
## **Section III.1 Abstract of Chapter III.**

In this chapter, as one of the methods using the friction force of a single rubber tube under positive pressurization, a novel mechanism with a linear structure is presented, in which a wire for structure locking is actuated by leverage through positive-pressurization.

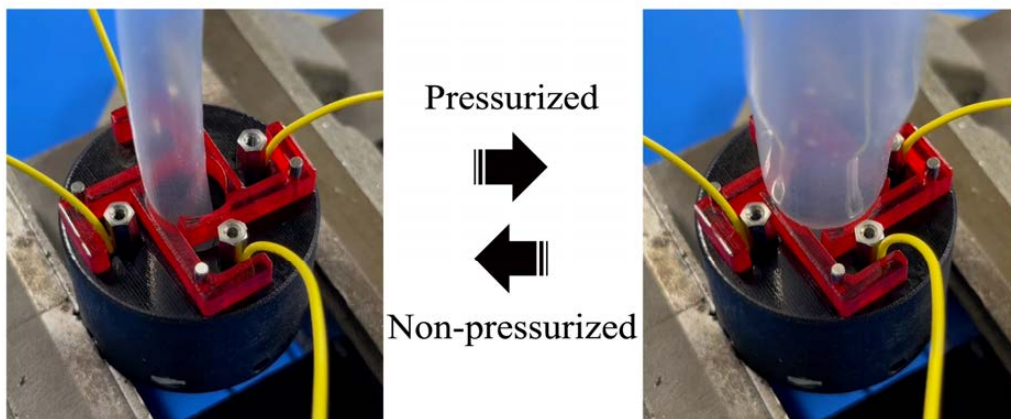
The proposed novel variable stiffness mechanism using a wire clamp with a lever achieves not only a high joint-locking-like layered structure [79][82], but also active bending [47][116]. Because the shape holding is performed using a lever, it is possible to achieve a high holding force because it depends not only on the performance of the actuator but also on the number of locking points in the joint structure (Fig. 37).

The purpose of this chapter is to investigate the effect of the wire-cramping force by comparing the holding torque with and without a lever. The holding performance of the proposed mechanism is evaluated by theoretical and experimental. In addition, as the proposed mechanism uses multiple wires, there is anisotropy in the holding torque in the bending direction; therefore, the maximum and minimum values of the holding torque were measured.

Using a theoretical model of the holding torque in the proposed mechanism, the holding torque was evaluated based on the measured holding torque in the bending directions when the actual pressure was applied. It was confirmed that the holding torque increases with the presence of wires at each internal pressure. Moreover, the results of this study show that the holding torque, both with and without wires, was evaluated through a combination of theoretical models and actual measurements.



(a) Prototype of proposed mechanism and cross-sectional view of levers and wire.



(b) Wires are cramped by rotated lever when positive pressure is applied.

Fig. 37 (a) Prototype of the proposed mechanism and cross-sectional view of levers and wires. (b) Wires are cramped by rotated lever when positive pressure is applied. The joints and levers are made of acrylic resin and are manufactured using a 3D printer (AGILISTA, Keyence, Japan). The wires are made of stainless steel (SC-75, Osaka Coat Rope, Japan).

## Section III.2 Basic principle of variable stiffness mechanism by leverage through positive-pressurization.

### Subsection III.2.1 Ball joint and rubber tube with lever and wire.

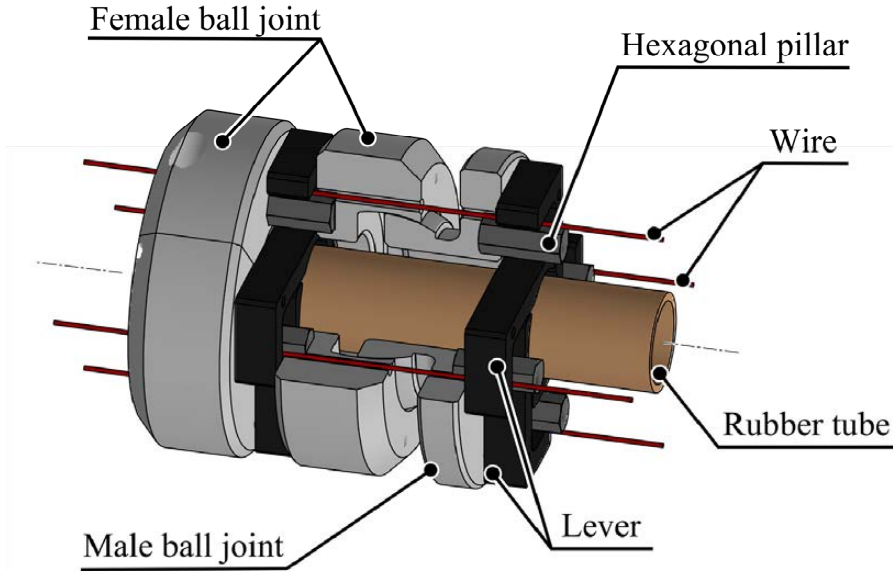
This subsection presents a solution to the issue described in Chapter 2, where the radially expanding joints were weak and at risk of bursting under positive-



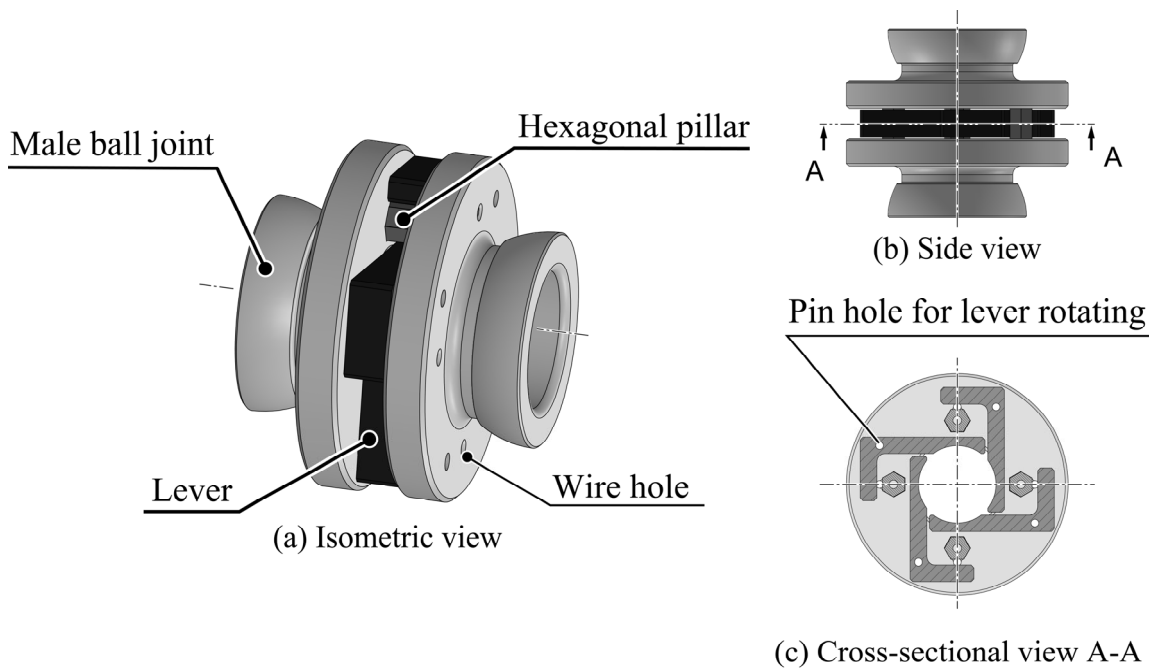
pressure. The low strength of these joints was attributed to the use of radial expandable hemispheres to generate joint-holding torque due to radial expansion forces.

To resolve this issue, a method is considered that constructs a structure capable of converting radial expansion forces into holding forces without relying on the deformation of the joint itself. Specifically, instead of relying on joint deformation for displacement, a locking mechanism is activated using translational or rotational displacements. This approach eliminates the need for a deforming section in the joint, thereby ensuring joint strength.

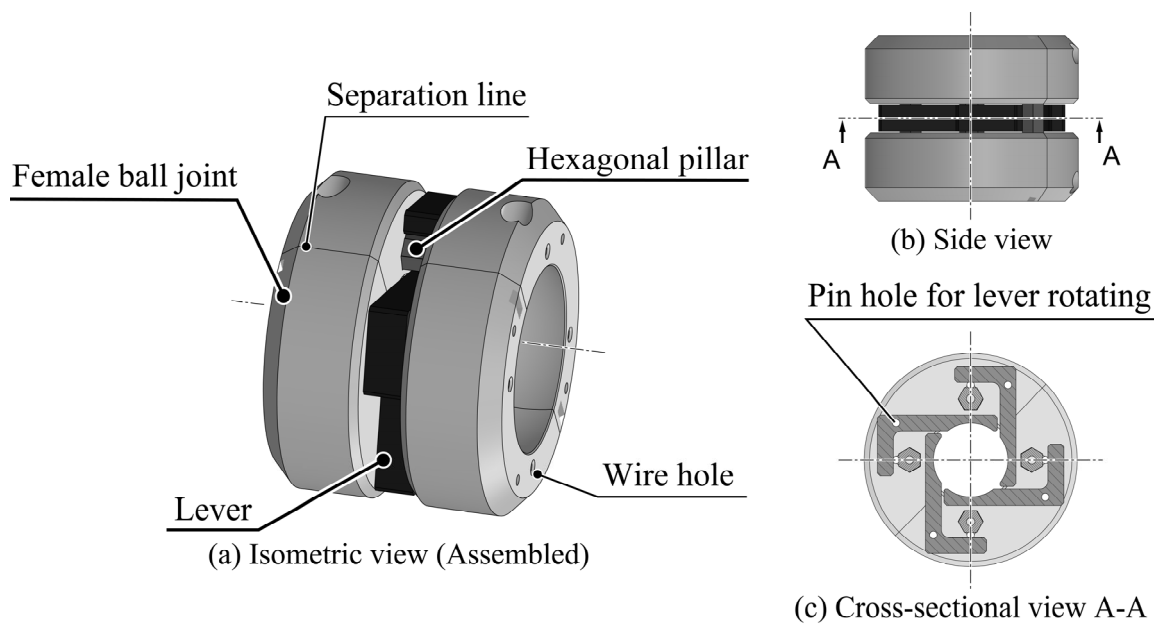
Based on this design principle, this subsection introduces a mechanism that generates holding force by rotating a lever, which can amplify the cramping force, using radial expansion force. The proposed mechanism is a radial expansion type of variable stiffness mechanism consisting of ball joints without slits, a single rubber tube, levers, and wires (Fig. 38). The main difference between the ball joint in the mechanism in this study and the one in Chapter II is that in this design, the male hemisphere and female shell are separated into two distinct joints (as depicted in Fig. 39 and Fig. 40). A rubber tube was enclosed within the joints. In addition, both the male and female ball joints were equipped with levers for wire clamping (as illustrated in Fig. 41 and Fig. 42).



**Fig. 38 Assembled all components of the proposed mechanism.**



**Fig. 39 Design of the male ball joint of the proposed method.**



**Fig. 40 Design of the female ball joint of the proposed method.**

In the proposed mechanism had no slit, whereas the joint in Fig. 39 consisted of two symmetrically aligned male components. These male joints were connected by hexagonal pillars. A lever was positioned between these male components, and a hole near the lever allowed the passage of the wire.

In Fig. 40, the joint features two symmetrically arranged female components that mirror the configuration of the male joint. These female joints are connected by hexagonal pillars. The levers have also been inserted between these female

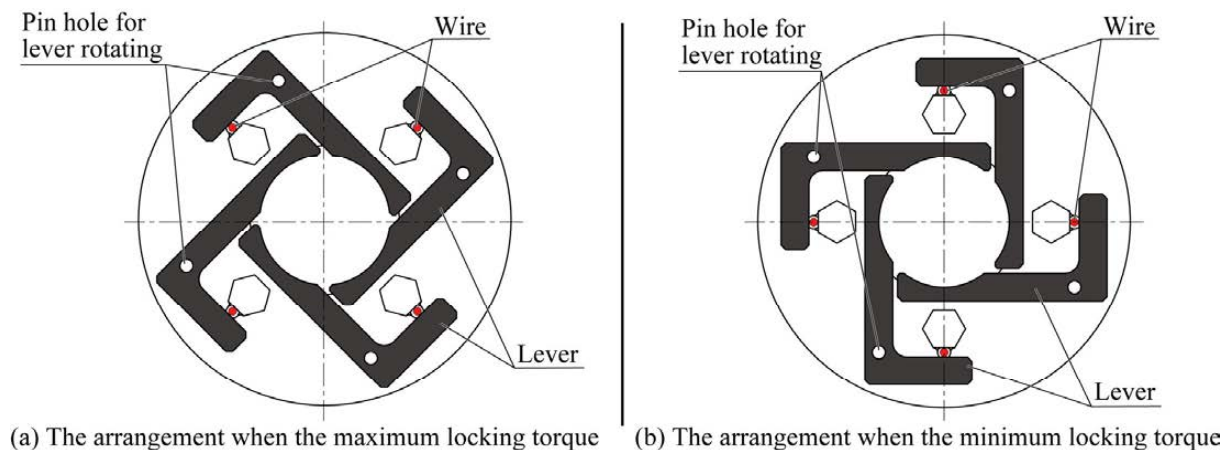
components, and a hole near the lever facilitated passage of the wire. The female joint is designed to be separable, which allows it to connect the male joint to the shell of the female joint. After a

male joint is connected to a female joint, the male joint can be encased in another female joint.

Fig. 41 illustrates the arrangement of the lever on the ball joint in the axial direction with maximum and minimum holding torques, whereas Fig. 42 outlines the fundamental principle of the proposed mechanism. A single rubber tube is enclosed within the ball joint, which includes the lever. Under positive pressure, the L-shaped lever rotated upon contact with the expanded rubber tube, allowing the joint to be locked by clamping the wires with the levers.

The shape-holding torque of the proposed mechanism is influenced by the number of wires and the lever length. The holding torque can be enhanced by increasing the number of wires and the length of the contact area with the rubber tube in relation to the length of the clamping area of the lever. However, it is important to note that due to the presence of multiple wires, the holding torque in the bending direction is anisotropic.

These wires can also be used to actively bend articulated structures. The holding torque varies with the number of wires. However, for applications involving active bending, it is ideal to use four wires; this can be achieved with two actuators. When no pressure was applied, it was advantageous that the wire and lever did not come into contact with each other, which prevented interference with the active bending motion.



**Fig. 41 Arrangement of the lever and wire on the ball joint.**

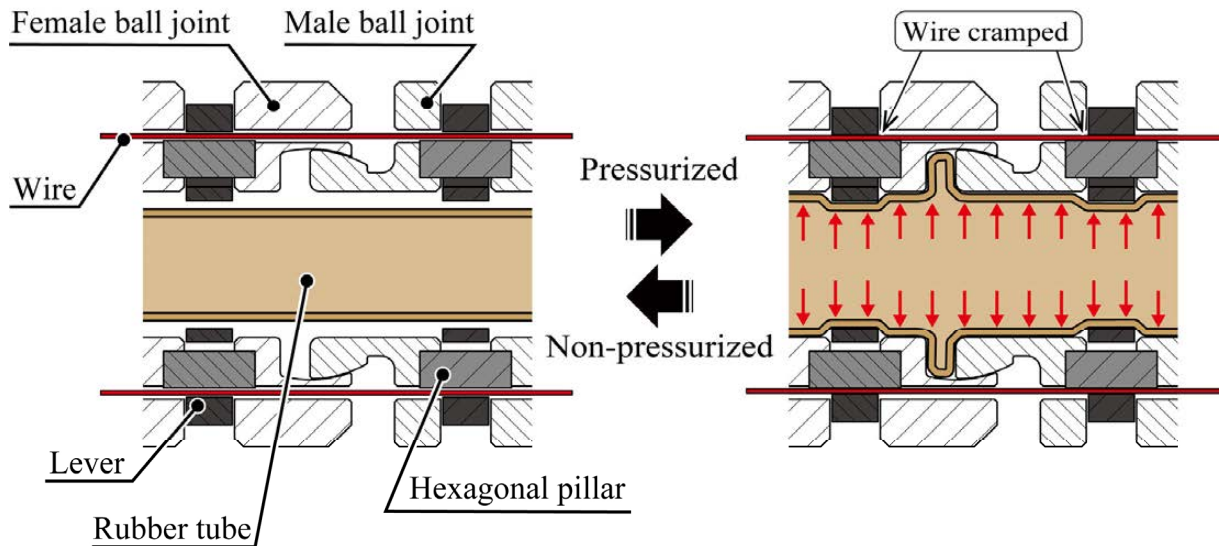


Fig. 42 Principle of the proposed method for variable stiffness. The wires are cramped by rotated lever when positive pressure is applied.

### Subsection III.2.2 Theoretical model of holding torque by frictional force between lever and wires, between ball joints.

A model was constructed to calculate the theoretical values of the holding torque in the bending direction. The purpose of this model is to estimate the effects of wire cramping and frictional force between the ball joints. The wire cramping was performed using the radial force of the rubber tube and the holding force between the ball joints was determined using the axial force of the rubber tube.

Fig. 43 shows the theoretical model of the holding torque with four levers when positive pressure is applied. In the Fig. 43,  $\tau$  is the holding torque in the bending direction. In addition, the clamping force on the left side of Fig. 43 does not affect the value of torque because the left side wire does not slip. First, the clamping force exerted by the levers is explained. Equation (32) shows the clamping force  $F_{radial}$  per lever,

$$F_{radial} = kPS_1/4, \quad (32)$$

$k$  is the magnification factor between the length of the contact area with the rubber tube and the clamping area of the lever,  $P$  is the internal pressure,  $S_1$  is the pressure area in the radial direction.

Equation (33) shows the  $k$ ,

$$k = \frac{l_1}{l_2}, \quad (33)$$

$l_1$  is the length of the contact area with the rubber tube and  $l_2$  is the length of the clamping area of the lever.

Equation (34) shows that the pressure acts in the radial direction.

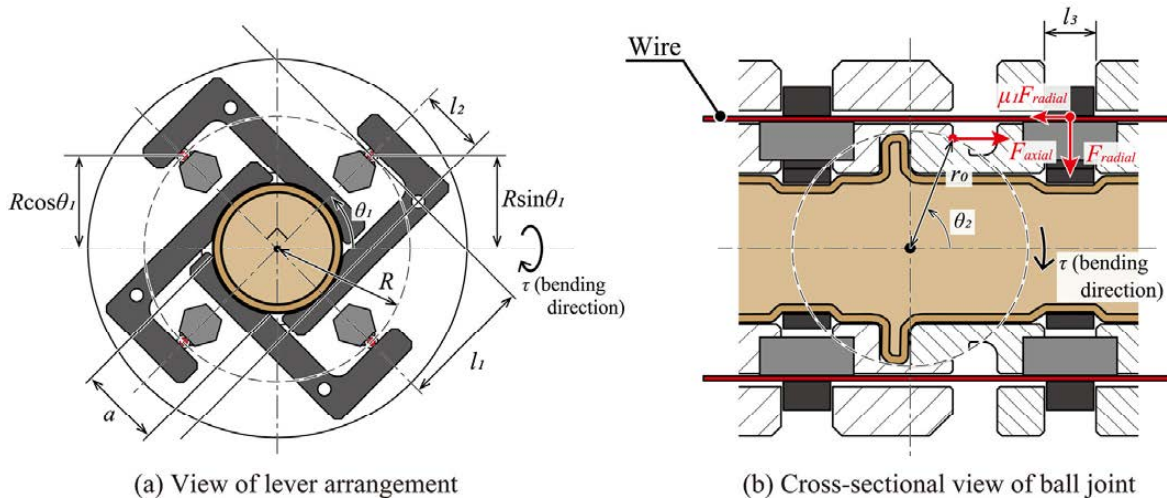
$$S_1 = 4al_3. \quad (34)$$

$a$  is the length of the lever that contacts the rubber tube,  $l_3$  is the length of the joint gap.

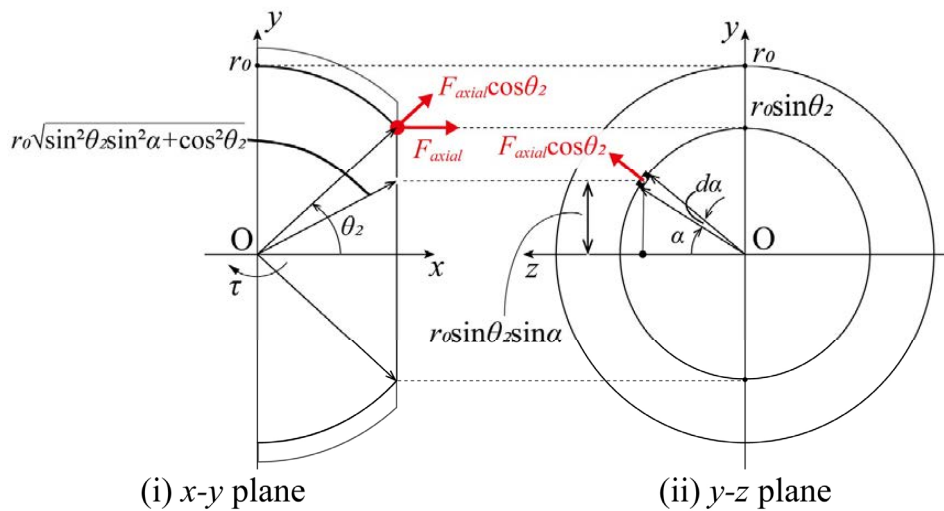
From equation (32) to (34), the holding torque of the lever clamp  $\tau_{lever\ clamp}$  is as follows,

$$\tau_{lever\ clamp} = 2\mu_1 F_{radial} R (\sin \theta_1 + \cos \theta_1) \quad (35)$$

$\mu_1$  is the static friction coefficient between levers and wires,  $R$  is the length from the center of the joint to the wire,  $\theta_1$  is the angle from center line of ball joint to the wire.



**Fig. 43 Theoretical model of holding torque with four levers when the positive pressure is applied.**



**Fig. 44 Holding torque due to the extension force applied to the contact surface of the segment by the rubber tube.**

Next, the extending force in the axial direction is indicated by pressurizing a rubber tube. Fig 44 shows the normal directional force via axial force on the differential area of the male ball joint. The distance from the center of rotation of the joint to the differential area is  $r_0$ . The angle from  $z$ -axis to the tip of male ball joint is  $\theta_2$ , while that around the  $x$ -axis is  $\alpha$ .

The radius  $r_z$  to the differential area on the circumference of radius  $r_0 \sin \theta_2$  in Fig. 44 is as follows:

$$r_z = r_0 \sqrt{\sin^2 \theta_2 \sin^2 \alpha + \cos^2 \theta_2}. \quad (36)$$

(36) indicates the distance to the center of rotation around the  $z$ -axis of the holding torque in the bending direction.

Equation (37) shows the extending force  $F_{axial}$ .

$$F_{axial} = PS_2, \quad (37)$$

$P$  is the internal pressure and  $S_2$  is the pressure area in the axial direction. Equation (38) indicates that the pressure areas in the axial direction.

$$S_2 = \pi r_0^2, \quad (38)$$

$r_0$  is the outer radius of the male joint. From (36) to (38), the expansion force in the axial direction  $f_{n2}$  is obtained as follows.

$$f_{n2} = F_{axial} \cos \theta_2. \quad (39)$$

From (39), the stresses  $\sigma_1$ , which is forces per unit area in the axial directions is as follows.

$$\sigma_2 = \frac{f_{n2}}{4 \int_0^{\frac{\pi}{2}} r_0 \sin \theta_2 d\alpha}. \quad (40)$$

The expansion force in the axial direction is transmitted to the bowl joint within the range of  $0 \leq \alpha \leq \pi/2$ . The reason for this range is that, in this study, it is assumed that the joints are in line contact with each other.

From (32) to (40), the holding torque of the proposed mechanism  $\tau$  is as follows,

$$\begin{aligned} \tau = & 2\mu_1 F_{radial} R (\sin \theta_1 + \cos \theta_1) \\ & + 4 \int_0^{\frac{\pi}{2}} \mu_2 \sigma_2 \cdot r_0 \sqrt{\sin^2 \theta_2 \sin^2 \alpha + \cos^2 \theta_2} \cdot r_0 \sin \theta_2 d\alpha. \end{aligned} \quad (41)$$

$\mu_2$  is the static friction coefficient between the ball joints.

The holding torque of the proposed mechanism change according to the value of

$\theta_l$ . The holding torque is maximum when  $\theta_l = \pi/4$ , and minimum when  $\theta_l = 0$  or  $\pi/2$ . From (41), the maximum holding torques  $\tau_{max}$  and the minimum holding torque  $\tau_{min}$  are expressed as follows:

$$\tau_{max} = 2\sqrt{2} \mu_1 F_{radial} R + 4 \int_0^{\frac{\pi}{2}} \mu_2 \sigma_2 \cdot r_0 \sqrt{\sin^2 \theta_2 \sin^2 \alpha + \cos^2 \theta_2} \cdot r_0 \sin \theta_2 d\alpha \quad (42)$$

$$\tau_{min} = 2\mu_1 F_{radial} R + 4 \int_0^{\frac{\pi}{2}} \mu_2 \sigma_2 \cdot r_0 \sqrt{\sin^2 \theta_2 \sin^2 \alpha + \cos^2 \theta_2} \cdot r_0 \sin \theta_2 d\alpha \quad (43)$$

Equations (42) and (43) indicate that the maximum holding torque via wire cramp is  $\sqrt{2}$  times larger than the minimum holding torque.

### Subsection III.2.3 Bending angle of the ball joints and shell scale for preventing joint dislocation.

In this subsection, the shell scale and the bending angles of the ball joints, which are critical for preventing joint dislocation are explained in detail (Fig. 45). In the proposed mechanism, it was imperative to design a joint that prevents dislocation of the joint during positive-pressurization. When formulating a joint design, joint dislocation can be prevented by considering the radius of the female joint relative to that of the male joint and the bending angle of the ball joints.

To prevent joint dislocation, the angle between the pivot point of the joint and the end of the shell  $\theta_2$  is smaller than  $\pi/2$ . If  $\theta_2$  exceeds  $\pi/2$ , it becomes impossible to prevent joint dislocation if a positive pressure is applied.

In addition, defining the bending angle of the joints as  $\theta_3$ , it is preferable if  $\theta_3$  is greater than  $\theta_2$ . Ensuring that  $\theta_3$  exceeds  $\theta_2$ , maintains that the rubber tube remains enclosed when the joint is maximally bent, preventing joint dislocation.

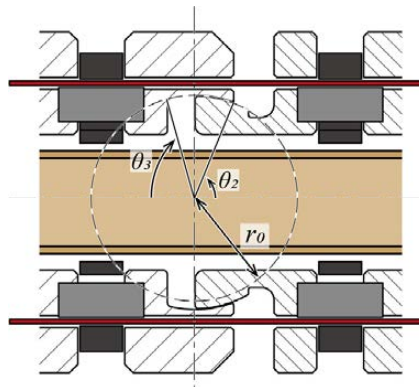


Fig. 45 Shell scale and ball joint bending angle, which are crucial for preventing joint dislocation.

### Section III.3 Mechanical design of variable stiffness mechanism by leverage through positive-pressurization.

#### Subsection III.3.1 Design method of the ball joint and lever for measuring the holding torque.

In this subsection, the designs of the ball joints, levers, rubber tubes, and air plugs are discussed. Figs. 46, 47, and 48 depict the prototypes of each component. Table VIII lists the parameters for these components, which were determined based on the theoretical model outlined in Subsection III.2.2 and Subsection III.2.3.

The male joint consists of a component with a spherical surface connected to the female joint and another component that secures the tip of the rubber tube (Fig. 46 (a) and (b)). These components were assembled by adhering them to hexagonal pillars. The wires were clamped with these hexagonal pillars and levers, and the tip of the rubber tube was secured with a set screw. The male joints were manufactured using a 3D printer (Markforged, Mark Two) with microcarbon fiber-filled nylon (Markforged, Onyx).

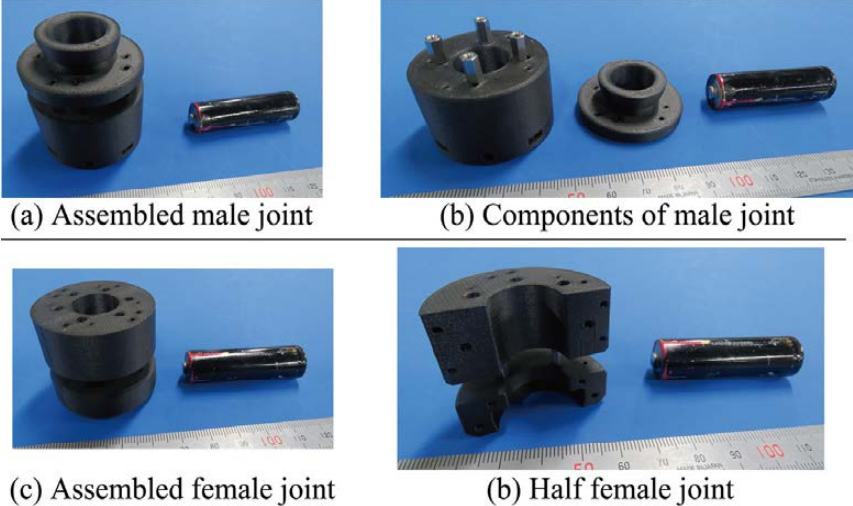


Fig. 46 Male and female joints of the proposed mechanism. The diameter of these joints is 40 mm. The inner radius of joints is 8.0 mm.



Fig. 47 Levers for wire cramping. The outer radius of the spherical surface where the lever contacts the rubber tube is 7.0 mm.





(a) Air plug



(b) Rubber tube

Fig. 48 Rubber tube and plugs of the proposed mechanism.

TABLE VIII  
Parameters of ball joints, levers and rubber tube.

Magnification factor between the length of the contact area with the rubber tube and the length of the lever's clamping area	$k$	2.0
Length of the contact area with the rubber tube	$l_1$ [mm]	14.0
Length of the lever's clamping area	$l_2$ [mm]	7.0
Length of the lever that contacts the rubber tube	$a$ [mm]	8.66
Length of the joint gap	$l_3$ [mm]	5.5
Outer radius of male joint	$r_o$ [mm]	12.5
Length from the center of joint to the wire	$R$ [mm]	14.0
Angle from the center of rotation of the joint to the end of the shell	$\theta_2$	$69\pi/180$
Bending angle of the joints	$\theta_3$	$75\pi/180$

The female joint consists of a component with a shell that connects to the male joint and another component that secures the base of the rubber tube (Fig. 45 (c) and (d)). These components were assembled in the same manner as the male joint by adhering them to a hexagonal pillar. The base of the rubber tube is fixed using a set of screws. The material was used for the female joints as for the male joints.

Fig. 47 shows the levers used to clamp the wires. The lever has a pin hole for rotating itself. The levers were machined using A5052 because of their high mechanical strength. When a positive-pressure of 0.2 MPa is applied, the deformation of the lever is minimal. The thickness of the lever is 5 mm.

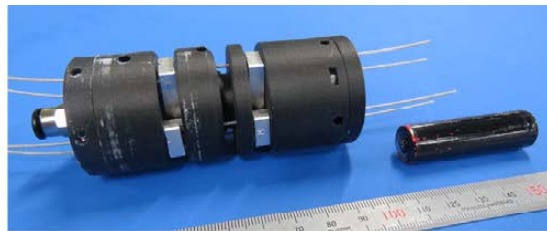
Fig. 48 (a) depicts the air plugs. The air plug was attached to the ends of a rubber tube with a tip diameter of 12 mm and a gluing section length of 12 mm. These plugs were fabricated from resin-containing glass (Rigid 10 K) using stereolithography (Form-labs, Form 3, United States).

Fig. 48 (b) show the rubber tubes assembled with the air plugs. The rubber tube with outer and inner diameters of 14 and 12 mm, respectively. The rubber tube

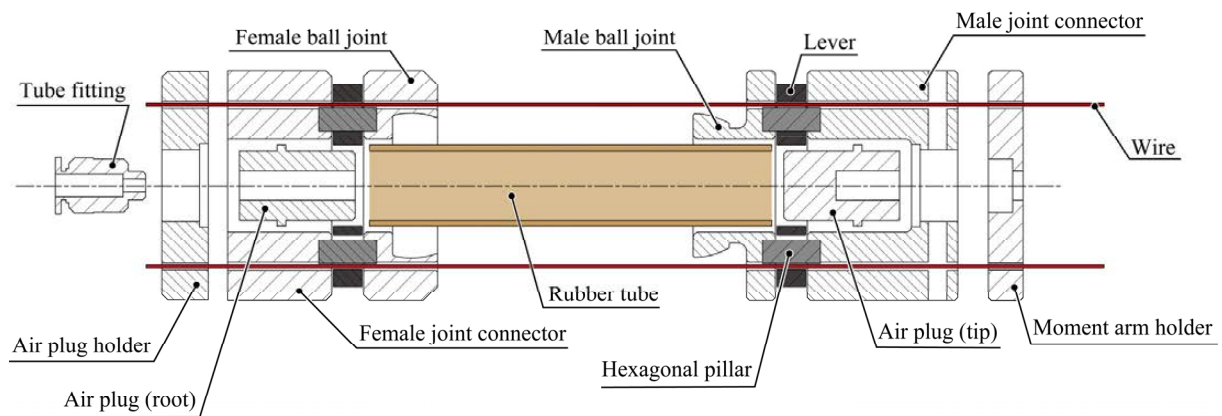
was composed of Ecoflex 00-50. The length of rubber tube is approximately 69.5 mm. The rubber tube is fabricated by using a mold.

### Subsection III.3.2 Assembly method of the prototype.

The assembly method for the experimental unit is illustrated in Fig. 49. First, the male and female joints were assembled by adhering them to the hexagonal pillars. The levers are inserted into the joints with pins. The air plugs at the tip and root are glued to a rubber tube. A single rubber tube with an air plug was inserted into the male joint and the tip of the rubber tube was fixed to the male joint using a set of screws. The separated female joint fits into the male joint, and the other female joint is covered on the male joint and rubber tube. The rubber tube root air plug was inserted into the base holder and the root air plug was attached to the female joint with a set of screws. The moment arm holder was fixed to the male joint. Finally, stainless-steel wires (SC-75, Osaka Coat Rope, Japan) were threaded through the holes in the joints.



(a) Experimental unit



(b) Assembly method of the experimental unit

**Fig. 49 Components and assembly of prototype for the proposed method.**

## Section III.4 Experiment of variable stiffness mechanism by leverage through positive-pressurization.

### Subsection III.4.1 Measurement of the cramping force and calculation of the coefficient static friction between wires and levers.

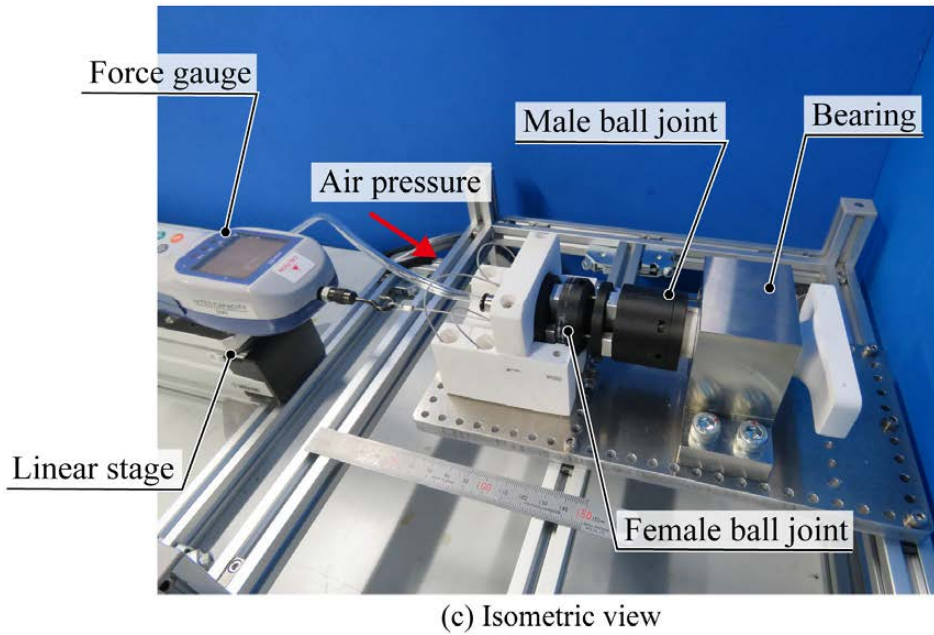
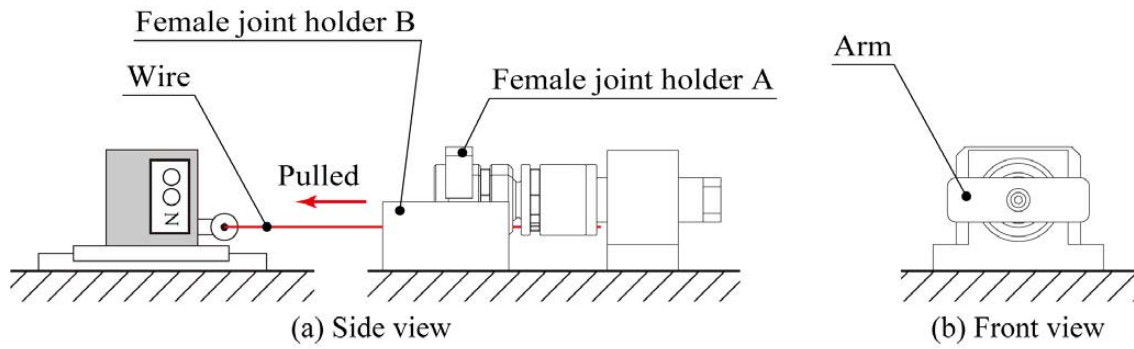
In this subsection, the measurements of the cramping force are presented, and the coefficient of static friction between the wires and levers is calculated. The purpose of this experiment is to experimentally determine the value of the static friction coefficient between levers and wires  $\mu_1$ .

To measure the clamping force under positive pressurization, an experimental setup, as shown in Fig. 50, was used. This setup involved pulling the wire clamped by a lever along the axial direction. In this experiment, the wire attached to the prototype fixed on the device was connected to a force gauge (RZ-5, Aikoh Engineering, Japan) mounted on a single-axis translation stage (RS306B, Misumi, Japan). When positive pressure was applied, the force gauge was moved at a constant speed to pull a single wire and measure the maximum static frictional force. It was important that the male joint, which passed through the bearing, did not rotate during wire pulling. An accurate pressure regulator (IR1020-01, ISE30A-01, SMC, Japan) was used to control the internal pressure.

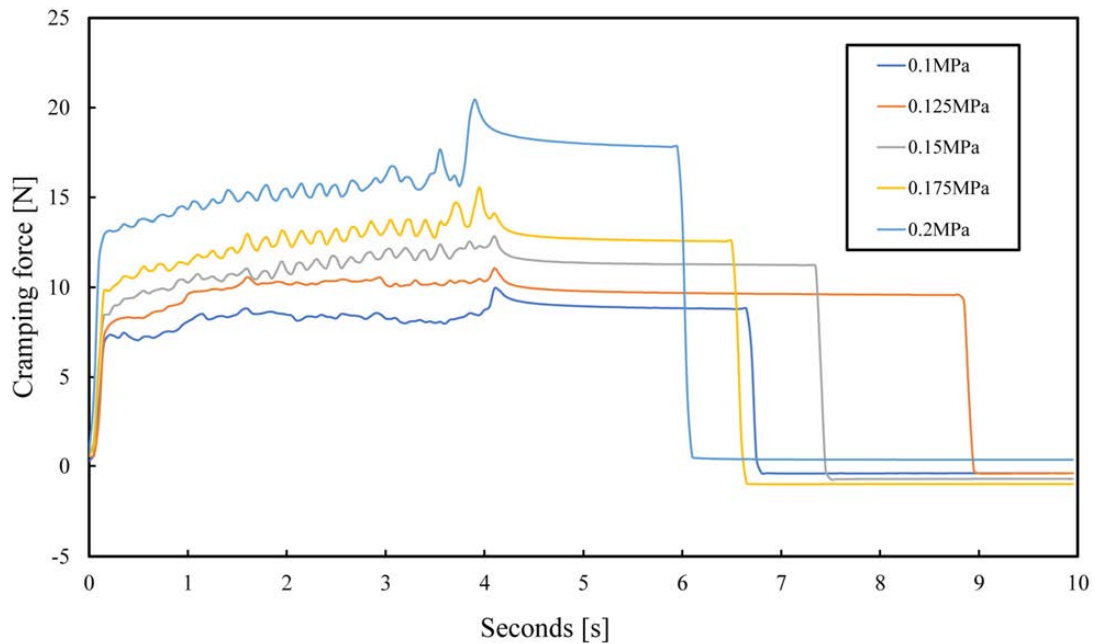
Next, how the static friction coefficient is calculated based on the measured maximum static frictional force is explained. The pulling force was measured five times for each internal pressure, and the average values of the pulling force were calculated accordingly. The static friction coefficient was determined using the average value of the tensile force at each measured internal pressure and (32). The formula used is as follows:

$$\mu_1 = \frac{F_{measured\_wire\ cramping}}{nkPS_1/4}, \quad (44)$$

$n$  is the number of ball joints and  $F_{measured\_wire\ cramping}$  is the average value of the tensile force at each measured internal pressure.



**Fig. 50** Experimental setup for measuring the clamping force under positive pressurization. The holder and arm are made of resin containing glass (Rigid 10K) and are manufactured using stereolithography (Formlabs, Form 3, United States).



**Fig. 51** Raw data of the last measured cramping force at each internal pressure. The first peak of the measured tensile force is the maximum static frictional force.

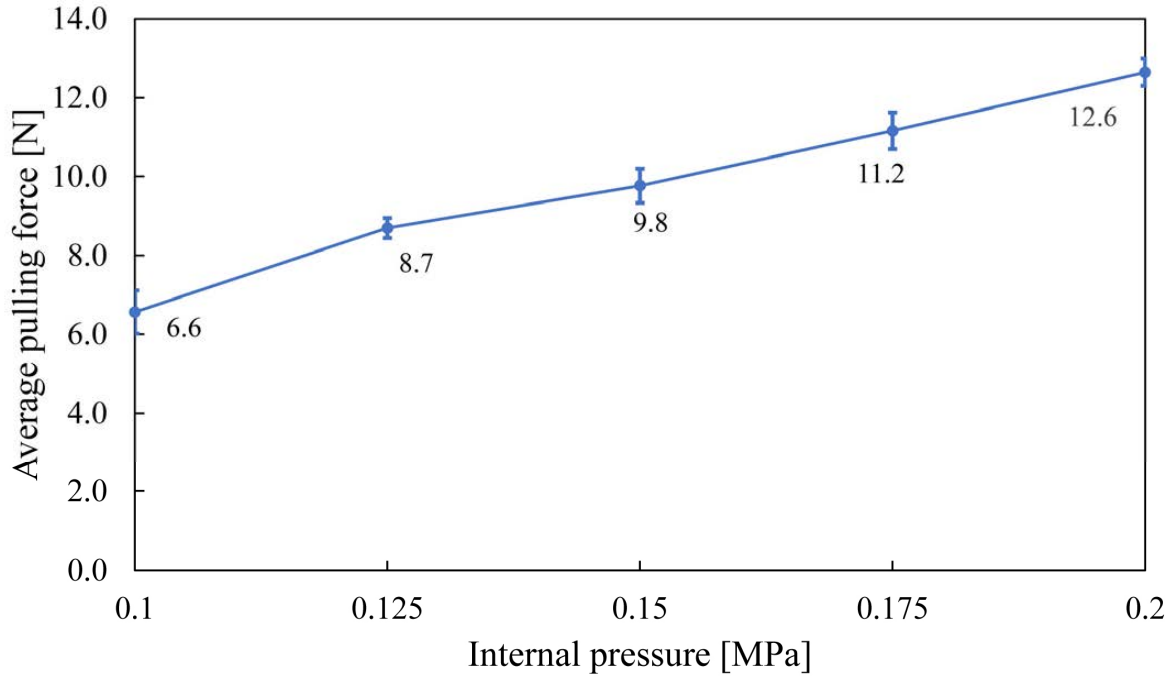


Fig. 52 Raw data of the last measured cramping force at each internal pressure.

**TABLE IX**  
Static friction coefficient values for each internal pressure

Internal pressure [MPa]	0.1	0.125	0.15	0.175	0.2
Static friction coefficient	0.345	0.365	0.342	0.335	0.332

Experimental conditions:

- The applied pressures were 0.1, 0.125, 0.15, 0.175, and 0.2 MPa.
- The pulling distance was 20 mm.
- The pulling velocity was 5 mm/s.
- The number of ball joints  $n$  was 2.
- The magnification factor between the length of the contact area with the rubber tube and the length of the lever's clamping area  $k$  was two.

Fig. 51 shows the raw data for the last measured pulling force at each internal pressure. Based on these raw data, the pulling force that initially reached its first peak value was designated as the maximum static friction force. The average value of the maximum static frictional force determined for each internal pressure was substituted into (44).

Fig. 52 shows the average values of the maximum static frictional force for each internal pressure, whereas Table IX lists the values of the static friction coefficient

for each internal pressure, calculated from the data in Fig. 52 using (44). According to these results, the value of  $\mu_l$  in this paper is established as 0.344. This value is used to evaluate the holding torque in Subsection IV.4.2

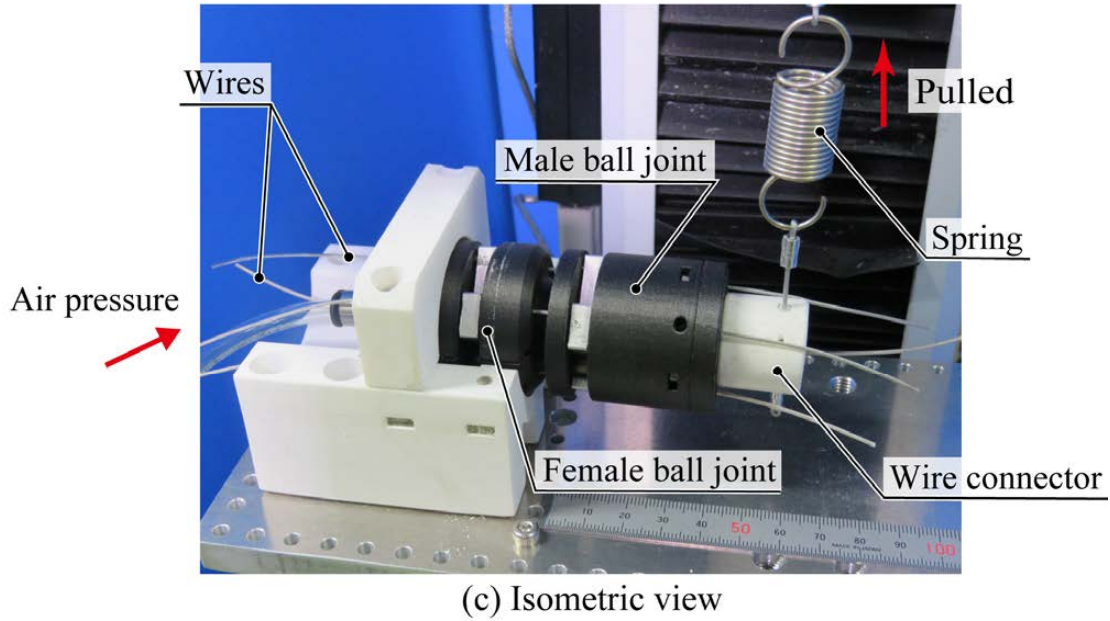
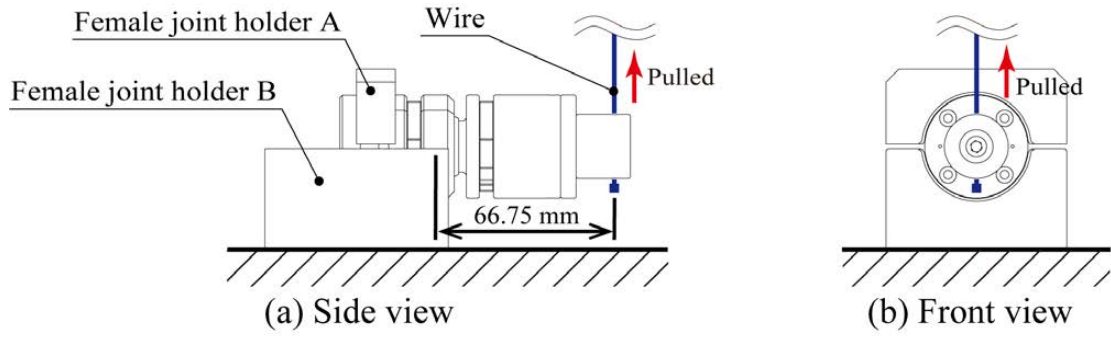
### **Subsection III.4.2 Measurement of the holding torque in the pitch direction with and without wires.**

In this subsection, the holding torque measurements in the bending directions are presented, including the maximum and minimum values, with and without wires. Fig. 53 shows the devices that were used to measure the holding torque in the pitch direction.

I measured the maximum and minimum pulling forces with wires and without wires, in the bending directions when the male joint was rotated to determine the maximum static frictional force using an experimental setup. The position of the experimental unit was adjusted to measure the maximum and minimum pulling forces of the wires. In this experiment, the wire connectors of the male joints were pulled using a wire connected to a spring attached to a tensile testing machine (Model 3343, INSTRON, Japan) when the internal pressure was applied. The pulling force at each internal pressure was measured five times, and the average values of the friction forces were obtained. The holding torque was calculated by multiplying the determined maximum value of the static frictional force by the length between the center of rotation and the pulling wire. The pulling wire used in the experiments was made of stainless steel (SC-120; Osaka Coat Rope, Japan). A high-precision regulator (IR1020-01, ISE30A-01, SMC, Japan) was used to control the internal pressure.

Experimental conditions:

- The applied pressures were 0.1, 0.125, 0.15, 0.175, and 0.2 MPa.
- The moment arm lengths were 66.75 mm in the pitch directions, as shown in Fig. 52.
- The pulling velocity was 30 mm/min.
- A tension coil spring (JB-311, TOKYO HATSUJYO MANUFACTURING, Japan) was used in the experiment. The spring constant was determined to be 0.7.
- The maximum pulling extension was set to 40 mm to measure the maximum static frictional force in the bending direction.



**Fig. 53** Experimental setup for measuring the holding torque in the bending direction. This setup offset the moments due to the weight of the arm from the measured value. The holder and connector are made of resin containing glass (Rigid 10K) and are manufactured using stereolithography (Formlabs, Form 3, United States).

- The coefficient of static friction between ball joints  $\mu_2$  was 2.03, which was determined from the experimental values of the average holding torque  $\tau_{measured\_no\_wire}$  at all internal pressures without wires and the following equation (45).

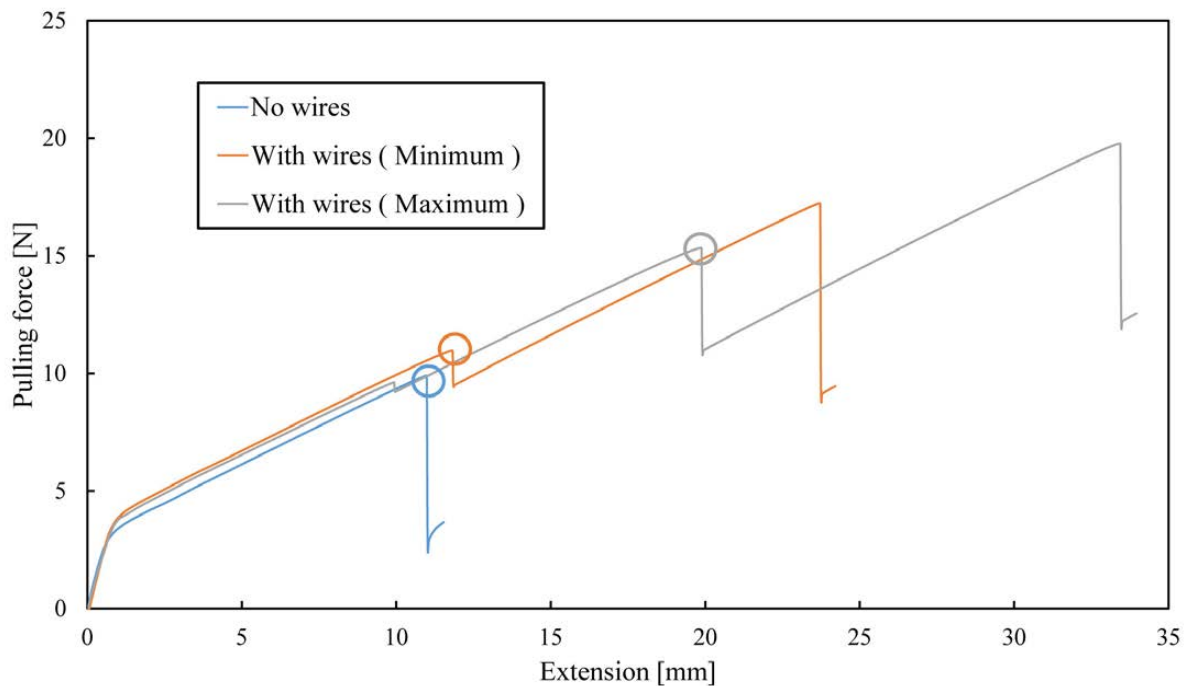
$$\mu_2 = \frac{\tau_{measured\_no\_wire}}{4 \int_0^{\frac{\pi}{2}} \sigma_2 \cdot r_0 \sqrt{\sin^2 \theta_2 \sin^2 \alpha + \cos^2 \theta_2} \cdot r_0 \sin \theta_2 \cdot d\alpha}, \quad (45)$$

Fig. 54 shows the raw data of the last measured maximum and minimum pulling forces with the wire in the bending direction and the pulling force without the wire when 0.2 MPa was applied. During the experiment, the male joint was pulled by a spring-loaded wire while a positive pressure was applied, causing the spring to extend. The spring contracts when the male joint rotates. The tensile force observed when the spring is compressed represents the maximum static frictional force. The holding torque was calculated by multiplying the tensile force observed

when the spring was compressed by the distance between the center of rotation and the tension wire.

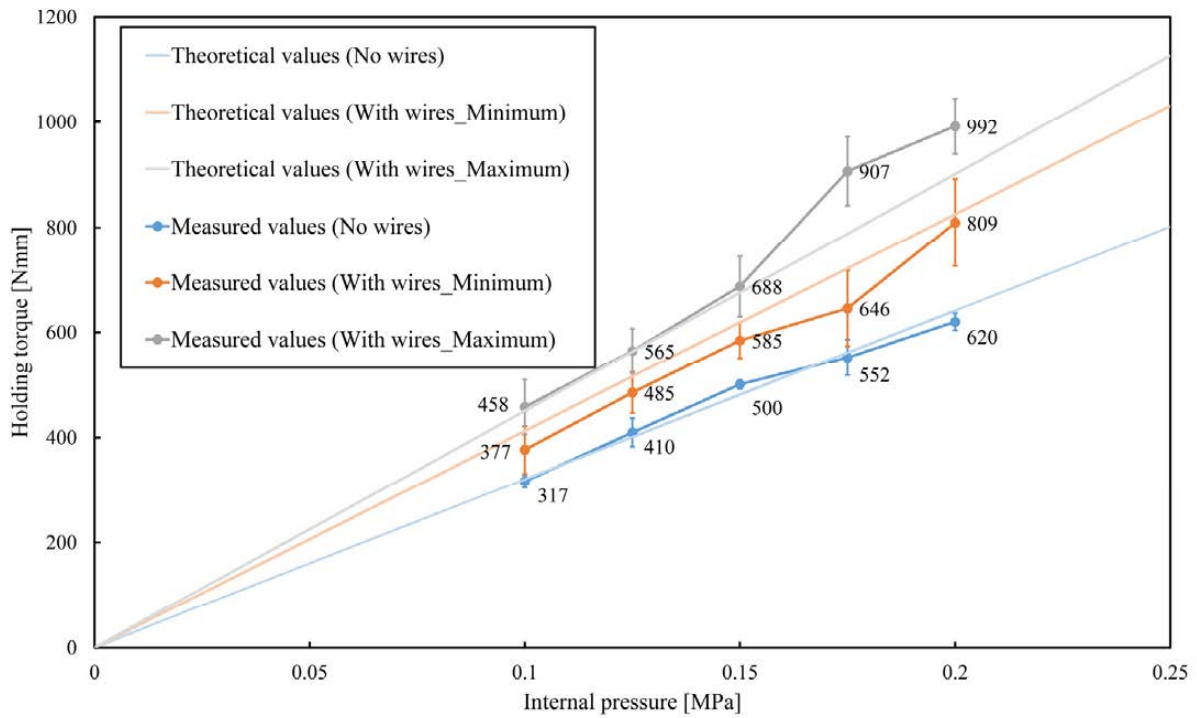
Fig. 55 shows the theoretical and measured values of the maximum and minimum holding torques with and without wires in the pitch direction at each internal pressure. Table X lists the magnification factors between the maximum and minimum holding torques for each measured internal pressure. Table X lists the errors between the theoretical and measured values of the maximum and minimum holding torques with and without wires in the bending direction for each internal pressure.

Fig. 55 and Table XI show that there is an anisotropy in the holding torque contingent on the wire arrangement. In the design parameters of the prototype in this paper, the magnification factors between the maximum and minimum holding torque with wire of the theoretical values were 1.09 times, and Table IX shows that the average magnification factors for each internal pressure of the experimental values were 1.24 times.



**Fig. 54** Raw data of the last measured pulling forces with the wire in the bending direction and the pulling force without the wire when 0.2 MPa was applied. The frictional force at the circle point is the maximum static friction force for calculating the holding torque under each condition.





**Fig. 55** Results of the theoretical and the measured values of holding torque in the bending directions. The error bar indicates the standard deviation of the measured value. This graph validates that the holding torque increases with the presence of wires at each internal pressure.

**TABLE X**

**Magnification factors between the maximum and minimum holding torque for each internal pressure measurement**

Internal pressure [MPa]	0.1	0.125	0.15	0.175	0.2
Magnification of locking torque	1.21	1.16	1.18	1.40	1.23

**TABLE XI**

**Errors between the theoretical and measured values of the maximum and minimum holding torques with wires and the holding torques without wires**

Internal pressure [MPa]	0.1	0.125	0.15	0.175	0.2
Error (With wires_Maximum) [%]	1.6	0.26	1.7	15.0	10.1
Error (With wires_Minimum) [%]	8.6	6.0	5.5	10.5	1.9
Error (No wires) [%]	1.2	2.1	4.0	1.6	3.3

Fig. 55 and Table XI display the average errors between the measured and theoretical values, indicating a 5.7% difference for the maximum holding torque, 6.5% for the minimum holding torque, and 2.5% for the holding torque without wire.

The larger average errors in the holding torque with wires compared to the holding torque without wires imply the increased number of contact surfaces resulting from wire usage, and a reduction in the contribution of the wire clamping force generated by the lever in certain situations. The results in this paper indicate that slipping on the spherical surface of the joint and slipping between the lever and wire do not occur simultaneously.

One way to evaluate the contribution of only wire clamping is to design a locking mechanism that relies solely on levers and wires, without the use of joints. Also, if there is slack in the wire, the effectiveness of the wire clamp in generating holding torque decreases, whereas the influence of the frictional force between the ball joints becomes more prominent. Methods to eliminate wire slack include winding the wire around a pulley and using a shape-memory alloy wire.

## **Section III.5 Discussion of Chapter III.**

In the proposed mechanism, the rubber tube is occasionally cut when positively pressurized, which causes difficulty maintaining airtightness. This problem arose because the rubber tube strongly contacted the corner of the lever, which led to the formation of holes on the rubber tube surface. There are several strategies to mitigate this problem and prevent damage to the rubber tubes. These include minimizing the sharpness of the lever corners, using a material more resistant to cuts such as Dragon-skin, instead of Ecoflex, and considering the use of a protective covering for the rubber tube made from a material with more resistance to cuts.

The wire crushing caused by lever clamps must be considered. Under the conditions of this prototype, I did not confirm to detect any wire crushing after several experiments. However, the effects on the wire during long-term operation cannot be dismissed. Therefore, a durability test of the wire is necessary for the practical application of the proposed mechanism.

It is necessary to determine the appropriate distance between the levers in the axial direction for the shape-holding and joint-bending angles. If the distance between the levers in the axial direction is large, the wire may buckle when the joint angle is changed, causing the cramping force to cease functioning. However, it must be taken into account that if the distance between the levers in the axial

direction is small, the maximum bending angle of the joint will be limited.

The cramping force acts mainly in the bending direction when the wires are arranged linearly, thereby limiting their effectiveness in the twisting direction. An example of a wire positioning that can exert a cramping force in the twisting direction is a spiral shape similar to that of a mesh tube. Nevertheless, considering the active bending function, it may be necessary to accommodate helical and linear wire arrangements.

Configurations that can further improve the holding torque in the proposed mechanism include changing the lever length and using the same ball joint as in the radial expansion type of Chapter II. Because this mechanism uses a boost mechanism, known as a lever, the configuration of the lever and wire may enable the attainment of a significant holding torque, even at pressures of one atmosphere or less.

In addition to ball joints, there are other methods for controlling the expansion of rubber tubes, such as hoses. The advantage of this approach is that the use of a ball joint results in discrete bending deformation of the linear structure, whereas using a hose allows for continuous deformation.

A concrete example of a structure that requires only two actuators for wire-based active bending is an actuator arrangement such as a toroidal origami monotrack [117]. By positioning two active pulleys driven by motors at the base of the linear structure and winding each wire diagonally, active bending in the pitch and yaw directions became feasible.

## **Section III.6 Conclusion of Chapter III.**

In this chapter, a novel mechanism is presented featuring a linear structure in which a wire is actuated for structure locking by leverage using positive pressurization. Positive pressure expands the enclosed rubber tube, causing the lever to pivot around the pin and subsequently clamp the wire with the pillars. The proposed variable stiffness mechanism achieves not only a high joint-locking but also active bending.

Using a theoretical model of the holding torque in the proposed mechanism, the holding torque based on the measured holding torque in the bending direction was

evaluated when pressure was actually applied.

It was confirmed that the holding torque increased in the presence of wires at each internal pressure. Moreover, the results of this study show that the holding torque, both with and without wires, was evaluated through a combination of theoretical models and actual measurements.

In the future, I intend to explore applications for the proposed mechanism, such as employing it in soft manipulators designed for challenging environments like underwater, inside of MRI, and in radiation-exposed settings. It's important that the proposed mechanism can be constructed using materials different from those outlined in this paper, and its locking function remains intact as long as the tube remains undamaged. By selecting materials for the proposed mechanism that are well-suited to the intended environment, there is a prospect that the mechanism will operate reliably, even in the aforementioned conditions.

## Chapter IV

# Articulated Tube Mechanism with Variable Stiffness and Shape Restoration Using a Pneumatic Actuator

# **Chapter IV Articulated Tube Mechanism with Variable Stiffness and Shape Restoration Using a Pneumatic Actuator**

## **Section IV.1 Abstract of Chapter IV.**

In this chapter, an articulated structure with a pneumatic artificial muscle that enables to change the rigidity and shape restoration by positive pressurization is explained. This mechanism consists of a single McKibben pneumatic artificial muscle [118][119] as a soft actuator enclosed in a link structure of connected rigid hollow segments (Fig 56).

The mechanism enables it to deform freely and achieve a high stiffness; it can also continuously change the holding torque based on a change in internal pressure. Furthermore, because the structure of the proposed mechanism is multi-jointed, it can hold arbitrary joint angles owing to the contraction force generated when a pressure is applied thereto. In addition, the shape of the hollow segment is simple, and its strength can be increased; consequently, its pressure resistance is high.

Moreover, since the McKibben pneumatic artificial muscle enclosed inside the link structure returns to a linear shape due to the force of elasticity and inner pressure, this mechanism can also obtain an actuation effect. The shape restoration occurs because the volume of the McKibben pneumatic artificial muscle when it is pressurized is most stable when it has a linear shape. This restoring actuation can be controlled by adjusting the time of rigidity from the root to the tip of the structure by changing the flow rate of air. There is a possibility that it can be applied for actuation [120][121] by using the restoration effect through this flow rate adjustment.

I measured the torque in the bending direction due to friction when the internal pressure and inner segment diameter were changed. I confirmed that the error between the measured and theoretical torque value was within a 20% at any inner diameter.

Also, since a pneumatic artificial muscle is enclosed inside the structure, an actuation effect can occur when the pressure is applied. I measured the restoring angle and force of this effect when the valve opening ratio and inner segment



**Fig. 56** Prototype of the proposed variable stiffness mechanism consisting of a pneumatic artificial muscle enclosed in a link structure.

diameter were changed. I confirmed the function that can change the shape restoration characteristics by changing the flow rate with a single pneumatic artificial muscle.

## Section IV.2 Basic principle of variable stiffness and shape restoration.

### Subsection IV.2.1 Driven method by McKibben pneumatic artificial muscles.

The various variable stiffness mechanisms have been researched that increase stiffness using friction, such as a method in which hollow segments contract by pulling a wire (Fig. 57(a)). However, in this mechanism, it was difficult to generate an actuation other than contraction when the wire is pulled.

In a previously proposed method on ball joint-type segments using positive pressure in Chapter II (Fig. 57 (b)), there is a thin-walled hemispherical rigid shell and a radial expandable hemisphere with slits in the longitudinal direction. Fig. 56(b) shows the internal workings of the proposed mechanism, which consists of an articulated structure with a ball joint connection and a rubber tube running through the structure. The hemisphere of the ball joint is deflected by pressurizing

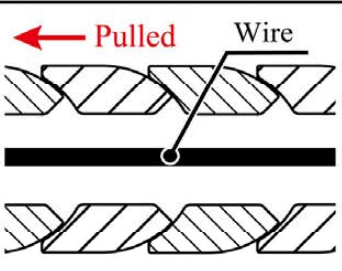
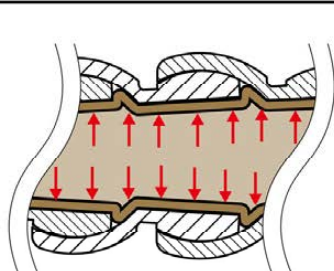
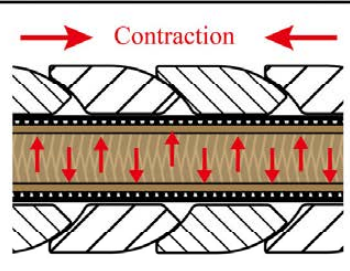
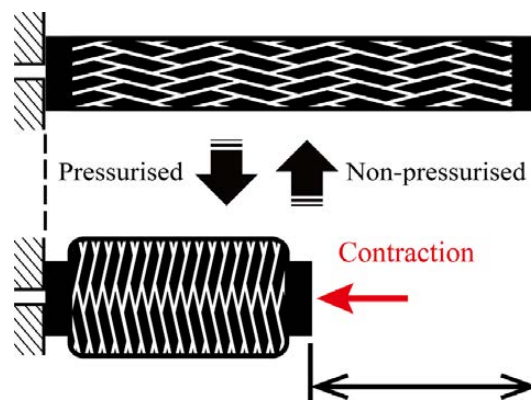
Wire method	Positive-Pressurisation method	
 <p>(a) Wire with segments in the axial direction</p>	 <p>(b) Rubber tube with ball joint type segments in the radial direction</p>	 <p>(c) Pneumatic artificial muscle with segments in the axial direction</p>
<p>✓ Structure becomes high stiffness by pulling a wire.</p> <p>✗ Difficult to generate an actuation.</p>	<p>✓ Structure becomes high stiffness by contacting pressure.</p> <p>✗ Difficult to generate an actuation, and the segments may separate during pressurization.</p>	<p>✓ Structure becomes high stiffness by contracting an artificial muscle.</p> <p>✓ Possible to generate an actuation.</p>

Fig. 57 Classification of friction-based variable stiffness mechanisms: (a) Wire method in the axial direction. (b) Positive-pressurization method in radial di-rection. (c) Positive-pressurization method in axial direction.



Contraction force when pressurized.

Fig. 58 Principle of pneumatic artificial muscles.

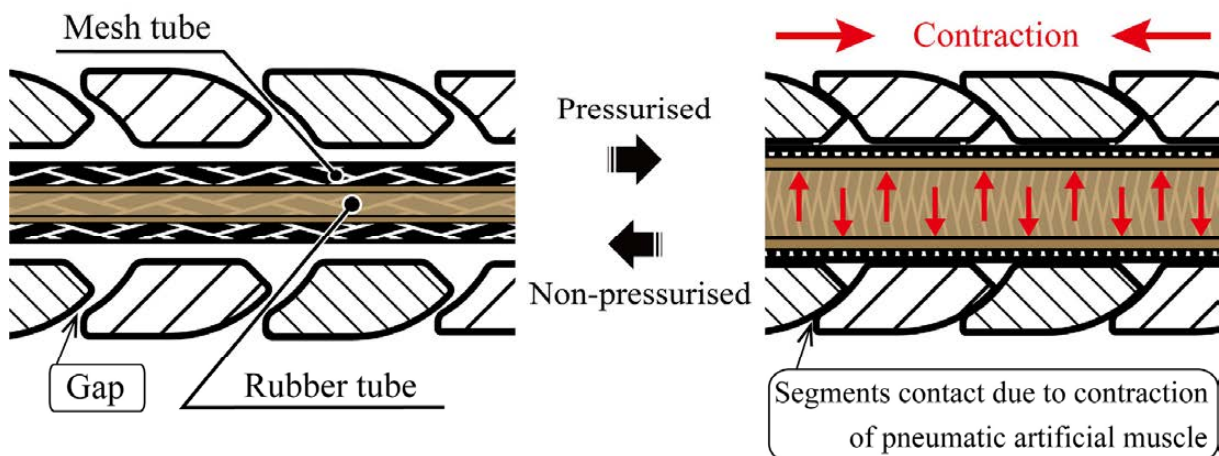


Fig. 59 Internal workings of the proposed mechanisms.



the rubber tube, and contact pressure is generated between the hemisphere and shell.

However, because this previous mechanism requires a radial expandable hemisphere to be fitted to the rigid shell, if the gap between the shell and hemisphere is large, the segments will dislocate during pressurization. Moreover, the enclosed rubber tube has a tendency to twist when it is not pressurized.

I devised a positive-pressurized variable stiffness mechanism that utilizes the axial contraction force generated by pneumatic artificial muscles to solve these problems (Fig. 57(c)). In this mechanism, pneumatic artificial muscles are enclosed inside the link structure connecting the hollow segments. To increase the stiffness, the segments come into contact because of the contraction force generated by pressurization. Moreover, the separation risk between each hollow segment can also be eliminated. Fig. 58 shows the principle of the pneumatic artificial muscles, and Fig. 59 shows the internal workings of the proposed mechanisms, which consist of an articulated structure with a hollow segment connection and pneumatic artificial muscles running through the structure.

The proposed mechanism not only provides such variable stiffness by applying positive-pressure but also enables the actuation from a curved shape by adjusting the flow rate of air. Furthermore, when the proposed mechanism is twisted, the enclosed pneumatic artificial muscle creates a rotational force around the axial direction.

## **Subsection IV.2.2      Theoretical model of holding torque in the pitch direction.**

This subsection explains the constructed model to derive the theoretical values of holding torque in the bending direction in the proposed mechanism. The purpose of this model is to estimate the value of the holding torque. In addition, modeling the holding torque in the bending direction serves as an index for estimating the limit against which the linear structure can extend.

Fig. 60 shows the normal directional force on the differential area of the male bowl joint. The distance from the center of rotation of the joint to the differential area is  $r_0$ . The angle from  $z$ -axis to the tip of male bowl joint is  $\theta_l$ , while that around the  $x$ -axis is  $\alpha$ .

The holding torques in the bending direction is  $\tau_l$ . The radius  $r_z$  to the differential area on the circumference of radius  $r_0 \sin \theta_l$  in Fig. 59 is as follows:

$$r_z = r_0 \sqrt{\sin^2 \theta_1 \sin^2 \alpha + \cos^2 \theta_1}. \quad (46)$$

(46) indicates the distance to the center of rotation around the  $z$ -axis of the holding torque in the bending direction.

$f_{nl}$  is the normal forces obtained from the axial forces in a differential area. At this time, the tangential force caused by the expansion of the rubber tube cancels out; thus, it does not affect the holding torque.

The expansion force in the axial direction is transmitted to the bowl joint within the range of  $0 \leq \alpha \leq \pi/2$ . The reason for this range is that, in this study, it is assumed that the joints are in line contact with each other.

The expansion force in the axial direction  $f_{n1}$  is obtained as follows.

$$f_{n1} = F \cos \theta_1. \quad (47)$$

Here,  $F$  is the measured axial force applied by the pneumatic artificial muscle. The value of  $F$  is to be determined using measurements obtained from the experimental setup described in Subsection IV.4.1, which will be elaborated upon later in this part. The segment moves in the axial direction and is grounded on the contact surface of the segment; however, the segment does not deform at this time.

From (47), the stresses  $\sigma_l$ , which is forces per unit area in the axial directions is as follows.

$$\sigma_1 = \frac{f_{n1}}{4 \int_0^{\pi/2} r_0 \sin \theta_1 d\alpha}, \quad (48)$$

From (46) to (48), the holding torque  $\tau_l$  in the bending direction caused by the internal pressure can be calculated by the maximum static friction force with respect to the distance to the center of rotation as follows:

$$\tau_1 = 4 \int_0^{\pi/2} \mu \sigma_1 \cdot r_0 \sqrt{\sin^2 \theta_1 \sin^2 \alpha + \cos^2 \theta_1} \cdot r_0 \sin \theta_1 d\alpha. \quad (49)$$

$\mu$  is the coefficient of static friction. This model considers only the contraction force of the pneumatic artificial muscle. Here, assuming that the central axes between joints are horizontal and coaxial. Also, the model shows that the torque is proportional to the radius of the segment and the coefficient of static friction, the

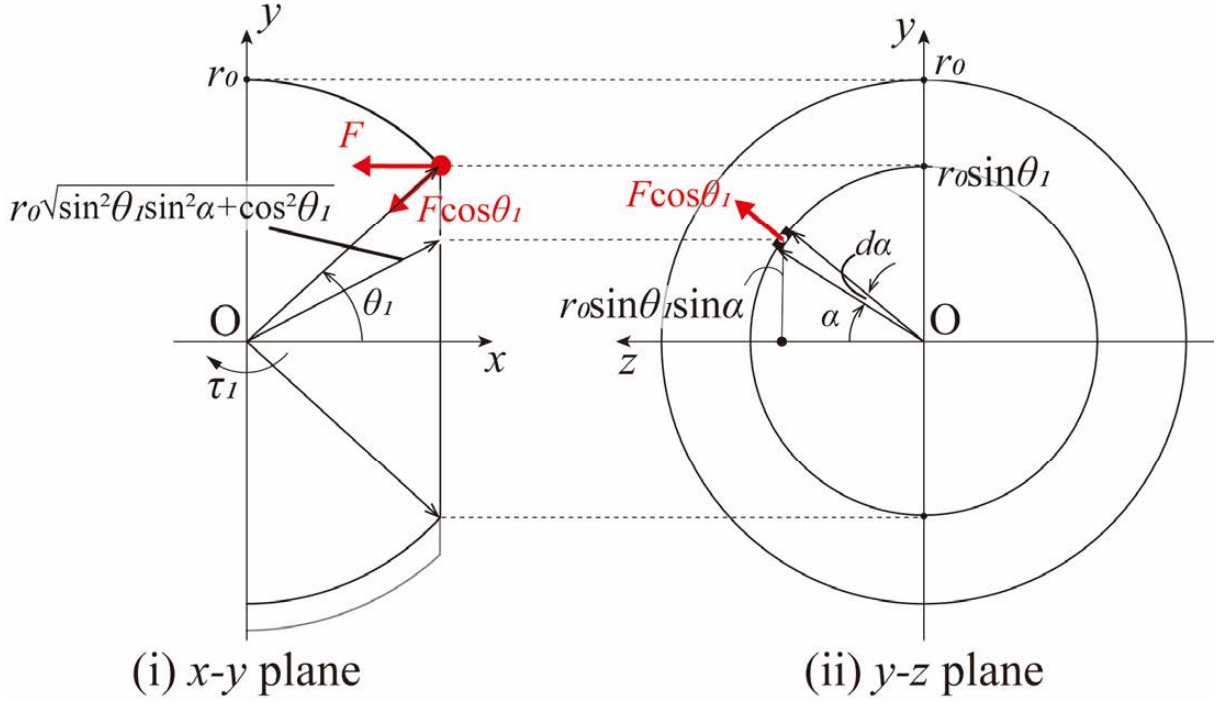


Fig. 60 Holding torque due to the contraction force applied to the contact surface of the segment by the pneumatic artificial muscle.

axial force applied by the pneumatic artificial muscle. The effect of the shape-restoring actuation is directly measured by comparing the theoretical value of the holding torque with the contraction force and measured value of the holding torque.

### Section IV.3 Mechanism design of prototype.

This section explains the assembly method, which is shown in Fig. 61(a). The air plug was inserted into the cap and then glued to it using an adhesive bond. The hollow segments were connected to form a linear structure. The pneumatic artificial muscle's root was glued to the connector, and the connector was attached to the locking head. Finally, the head was fixed to the hollow segments and the tube fitting was inserted into the connector.

Fig. 55 shows the prototype, Table XII lists the specifications, and Fig. 61(b) shows the fabricated hollow segment. The outer diameter of the hollow segments is the same value as the prototype in Chapter II.

The segment of the prototype is made of acrylic resin and is manufactured using a 3D printer (AGILISTA, Keyence, Japan). The coefficient of static friction of this resin is 0.427 [79]. The mesh tube (BTUB-UL20-10, Misumi, Japan) is made of polyester monofilament, and the braid angle is 20°. The rubber tube is made of

silicon rubber (custom-made product, Hagitec, Japan) with a shore hardness of 55. A detailed discussion of tube materials is a topic for future work, but these tubes were used because they are easily deformed by external force when no pressure is applied.

The prototype could vary its joint angles arbitrarily when not pressurized and could hold the joint angle when pressurized. Fig. 61(c) shows the maximum radius of curvature, which was 25 mm. The maximum bending angle per segment was  $26^\circ$  and the prototype had 21 segments. So, the total bending angle was  $546^\circ$ .

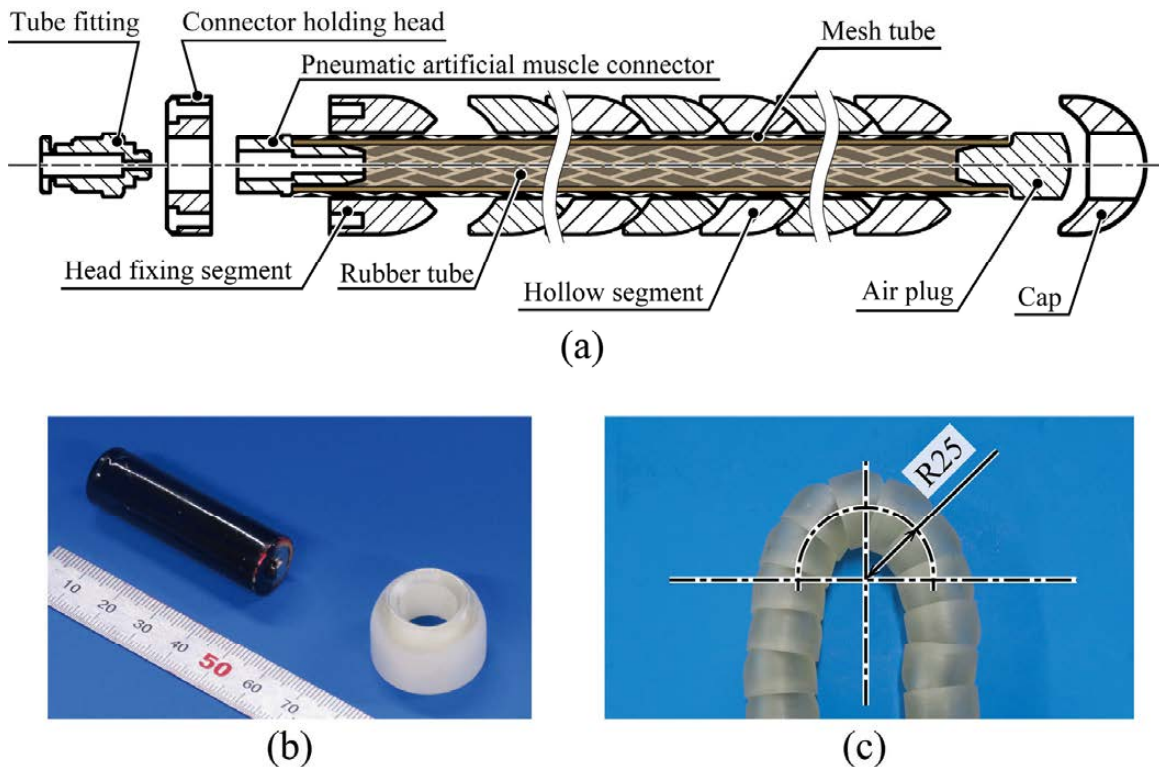


Fig. 61 Prototype of the proposed method. (a) Assembly method of the linear structure. (b) Fabricated hollow segment. (c) Maximum radius of the curvature of the prototype.

TABLE XII  
Specification of the prototype.

Length	[mm]	330
Mass	[g]	130.6
Outer segment diameter	[mm]	25.0
Inner segment diameter	[mm]	13.0
Outer diameter of the mesh tube	[mm]	10.0
Inner diameter of the mesh tube	[mm]	9.0
Outer diameter of the rubber tube	[mm]	7.0
Inner diameter of the rubber tube	[mm]	6.5

Moreover, when the flow rate of the air was changed in this prototype, the amount of restoration differed. To indicate the amount of change from the position of the tip of the prototype, the prototype was placed on a Teflon sheet and pressurized by changing the flow rate [L/min]. When the flow rate was high (Fig. 62), the position change of the prototype tip was about 7 mm because the restoration effect was enhanced. In contrast, when the flow rate was low (Fig. 63), the restoration effect was weakened, the tip position changed significantly, the movement distance was 61 mm.

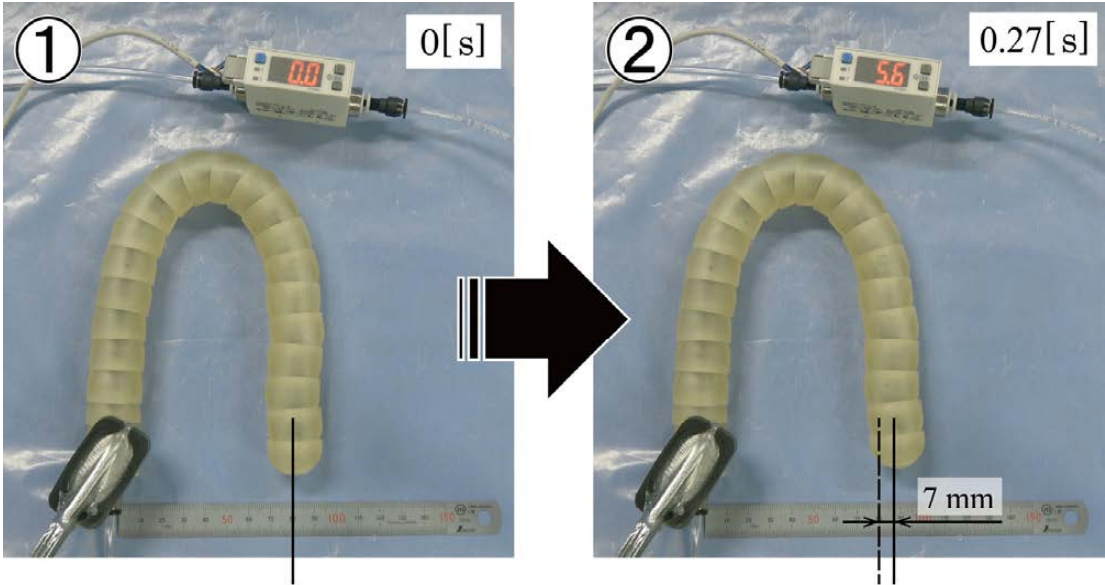


Fig. 62 Results of the shape-restoring actuation when the flow rate is increased using the prototype.

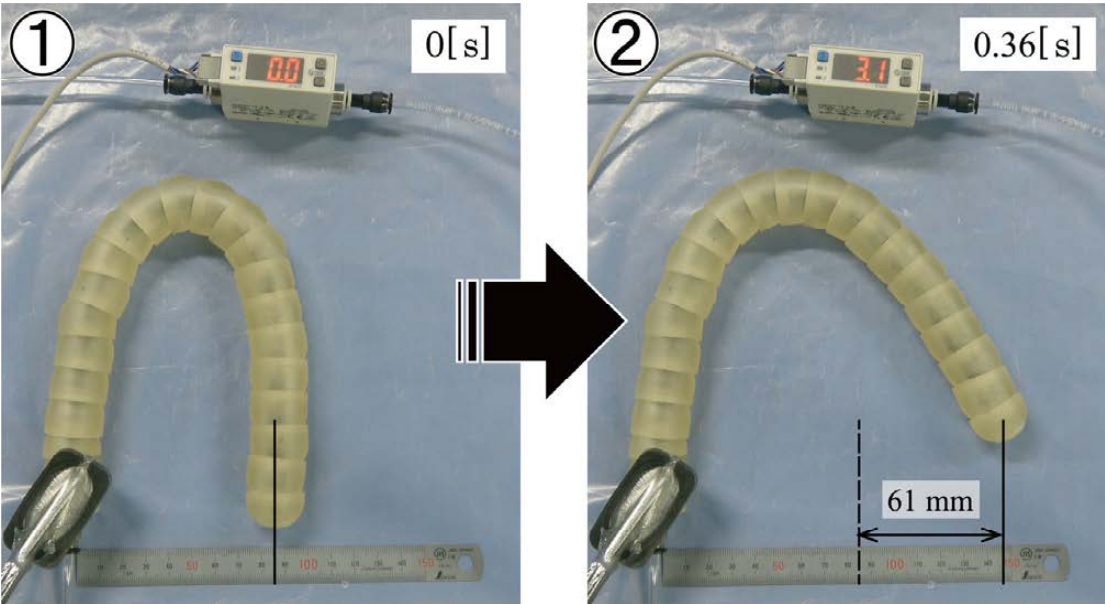


Fig. 63 Results of the shape-restoring actuation when the flow rate is reduced using the prototype.

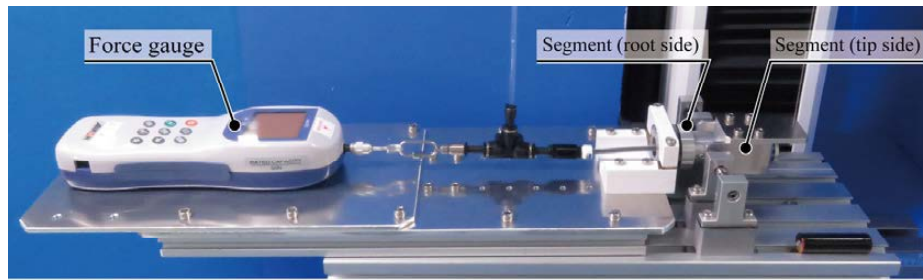
## Section IV.4 Experiment for evaluating the performance of prototype.

### Subsection IV.4.1 Measurement of holding torque in the pitch direction.

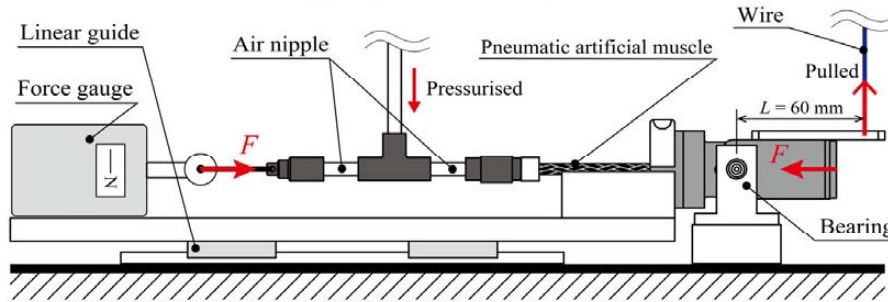
This subsection presents the measurements of the holding torque in the bending direction and compare them with the theoretical values. I evaluated the effect of pneumatic artificial muscles on the holding torque when the joint angle is horizontal, by measuring the holding torque when the segment inner diameter and internal pressure are changed. The reason for measuring the holding torque in the horizontal state is to prevent the bulging pneumatic artificial muscle from coming into contact with anything other than the inner wall of the segment.

Fig. 64 shows the devices used to measure the holding torque in the pitch direction. In this experiment, the moment arm was pulled upward by a wire that was tied to a tensile testing machine (Model 3343, INSTRON, Japan) under pressure. Furthermore, because the wire used in the experiments was made of stainless steel, the wire itself was long and not included in the model. A high precision regulator (IR1020-01, ISE30A-01, SMC, Japan) was used to control the air pressure. A pneumatic artificial muscle with a drive length of 100 mm, and outer diameter of 5 mm (PMJ40×100-UK-Q, Koganei, Japan) were used to measure the holding torque. A force gauge was attached to the base of the pneumatic artificial muscle, and the contraction force was measured simultaneously by moving the force gauge fixed to the linear guide and the segment at the base together. The material of the segment was machined duralumin (A2017) treated with white alumite with a surface roughness of Ra 3.2. I machined the metal to reduce the deformation of the segment due to contraction force and measure the coefficient of static friction.

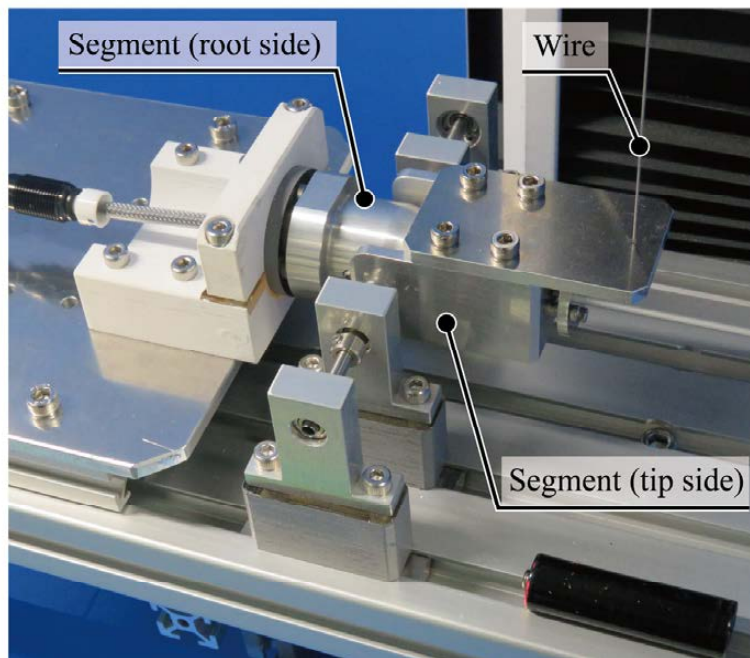
Fig. 65 shows the cross-sectional view of the experimental device and split collar. The root segment has an internal thread, which was fixed with a truncated cone point screw so that the collar did not shift. The chamfer angle of the collar was 30°. If the bending angle was 30°, the cross-section of the pneumatic artificial muscle would not be crushed by the segment.



(a) Experimental setup



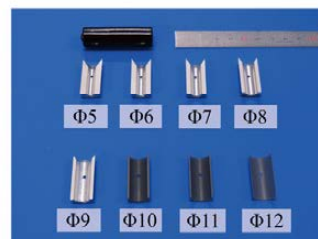
(b) Method of measurement for holding torque



(c) Experimental setup about segment

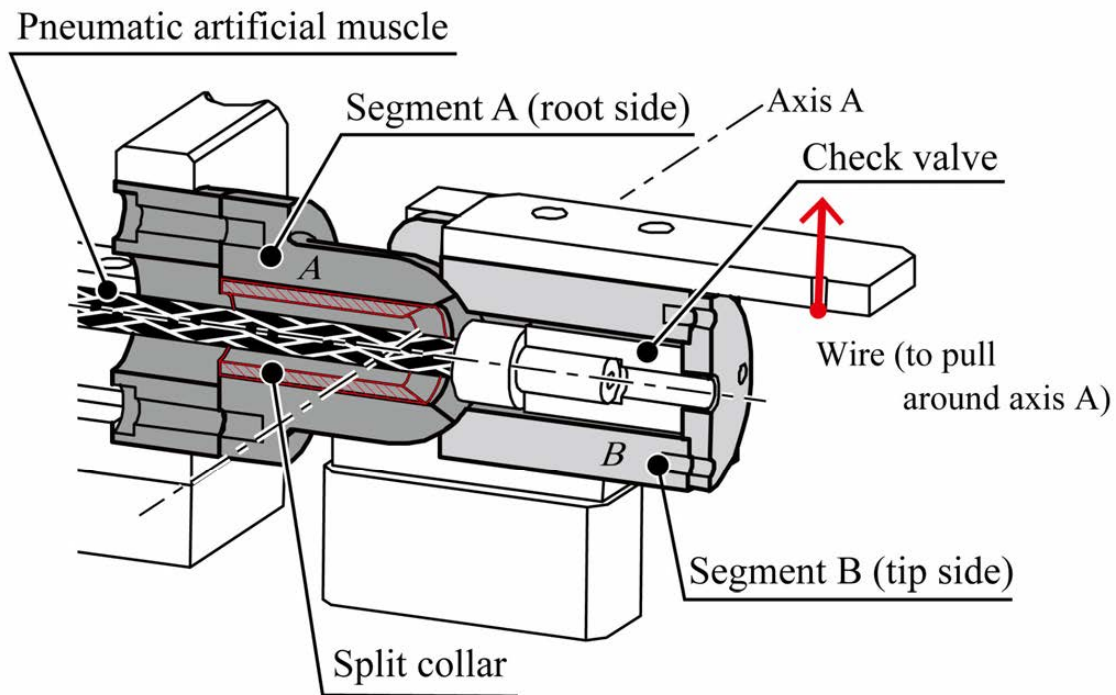


(d) Pneumatic artificial muscle



(e) Split collar for adjusting inner segment diameter [mm]

**Fig. 64** Experimental device for measuring holding torque in the pitch direction. (a) Experimental setup. (b) Method of measurement for holding torque. (c) Experimental setup about segment. (d) Pneumatic artificial muscle. (e) Split collar for adjusting inner segment diameter.



**Fig. 65** Cross-sectional view of the experimental device for measuring holding torque in the pitch direction.

The force required for pulling at each pressure was measured five times, and the average value of the maximum static friction force was obtained. The holding torque was then calculated by multiplying the obtained maximum value of the static friction force by the length from the center of rotation to the tip of the arm.

Experimental conditions:

- Pressures of 0.2, 0.25, and 0.3 MPa were applied. Here, 0.3 MPa is the maximum working pressure, and 0.2 MPa is the pressure required to obtain a torque of about 0.1 Nm.
- The inner segment diameters were 5, 6, 7, 8, 9, 10, 11, 12, and 13 mm. The split collars having diameters 5, 6, 7, 8, and 9 mm were made from machined duralumin (A2017), while those with diameters 10, 11, and 12 mm were made of ABS-like resins (Tough 2000) by using stereolithography (Formlabs, Form 3, United States). Here, 5 mm was the same value as the outer diameter of a pneumatic artificial muscle, and 13 mm was the maximum inner diameter of the experimental segment when the split collar was not used.
- The outer segment diameter was 25 mm.
- The moment arm length  $L$  was 0.06 m.



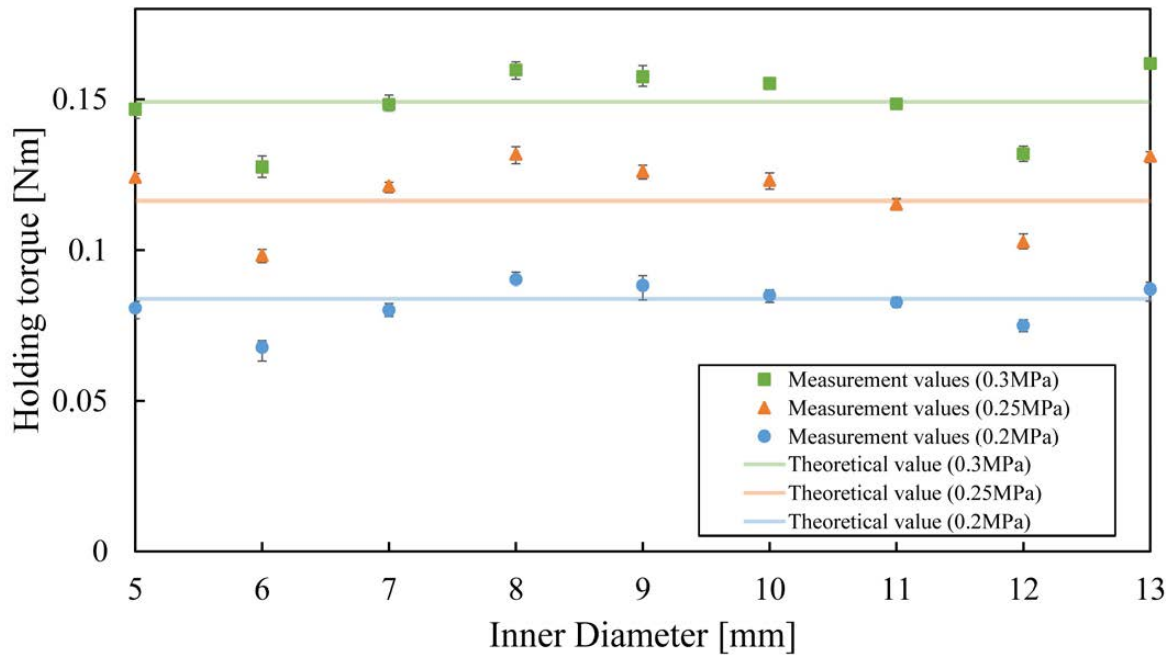
- The mass of tip segment is 106 g.
- The pulling velocity was 0.25 mm/s.
- The axial distance between the segments was 0.5 mm. When the pneumatic artificial muscle constructed by 0.5 mm, the outer diameter of the pneumatic artificial muscle became 5.5 mm.
- To measure the maximum static friction force in the pitch directions, the pulling extensions was 2 mm.
- The axial distance between the segments was 0.5 mm.
- The angle from z-axis to the tip of male bowl joint  $\theta_l$  is  $(43.5\pi/180)$ .
- The coefficient of static friction was 0.574, which was determined from exuation (49) and the experimental values of average holding torque at all diameters.

$$\mu = \frac{\tau_{measured\_bending}}{4 \int_0^{\pi} \sigma_1 \cdot r_0 \sqrt{\sin^2 \theta_1 \sin^2 \alpha + \cos^2 \theta_1} \cdot r_0 \sin \theta_1 d\alpha}, \quad (50)$$

**TABLE XIII**

**Theoretical value of the holding torque for each internal pressure**

Internal pressure [MPa]	0.2	0.25	0.3
Locking torque [Nm]	0.084	0.116	0.149



**Fig. 66 Comparison of the theoretical and measured values of holding torque in the pitch direction. The error bar indicates the maximum and minimum of the measured values, and the average of five trials is shown.**

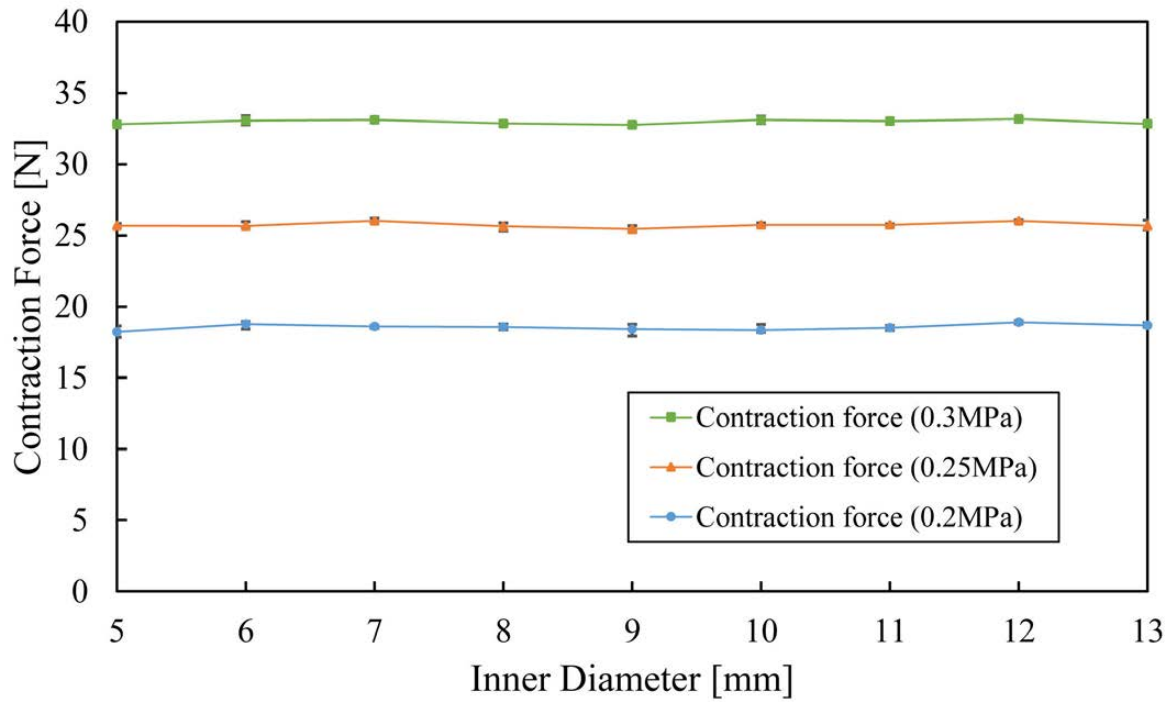


Fig. 67 Results of the measured values of contraction force. The error bar indicates the maximum and minimum of the measured values, and the average of five trials is shown.

TABLE XIV

Error values of the holding torque in the bending direction between measured and theoretical values for each internal pressures and inner diameters.

Internal pressure [MPa]	Inner diameter [mm]								
	5	6	7	8	9	10	11	12	13
0.2	3.7 %	19.1 %	4.5 %	7.7 %	5.3 %	1.4 %	1.4 %	10.6 %	3.8 %
0.25	6.6 %	15.5 %	4.3 %	13.3 %	8.4 %	5.9 %	0.93 %	11.7 %	12.7 %
0.3	1.6 %	14.4 %	0.56 %	7.1 %	5.7 %	4.1 %	0.45 %	11.5 %	8.6 %

Fig. 66 compares the measured and theoretical values for each inner diameter and internal pressure. The moments due to the arm's self-weight were offset from the measured values. Table XIII shows the theoretical value of the holding torque for each internal pressure.

Fig. 67 shows the actual values of the contraction force generated when I measured the holding torque. These results show that the difference in contraction force is small even when the inner segment diameters are changed.

As these results and Table XIV show, the error between the measured and theoretical torque value was within 20% at any inner diameter. So, assuming that the central axes between joints were horizontal and coaxial, the holding torque is

not affected by the value of the inner segment diameter.

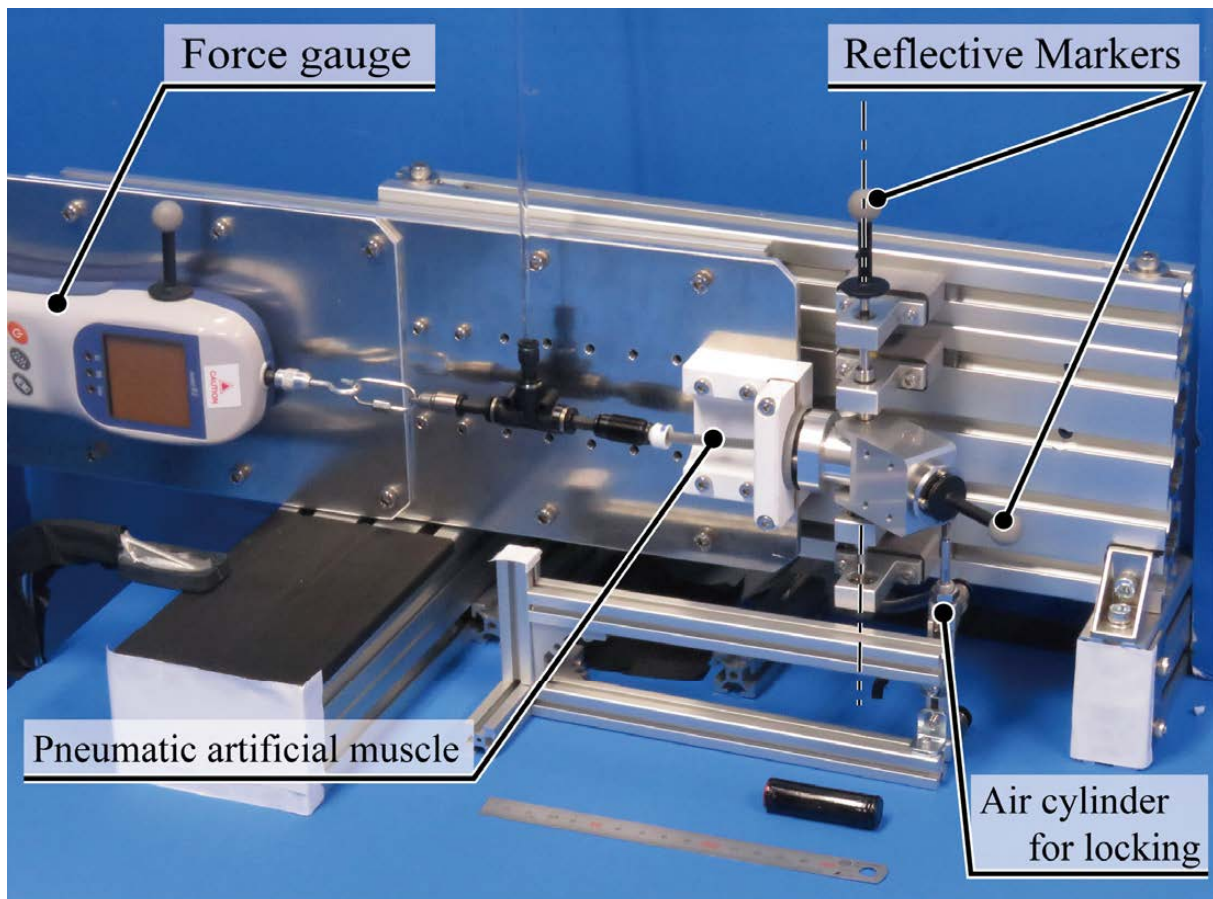
It was possible to estimate the theoretical maximum total length of the prototype that can retain the linear shape with the current model of holding torque. From the theoretical value, when assuming the mass of the prototype is 130.6 g, the maximum total length of the prototype that can retain the linear shape was 131 mm at 0.2 MPa, 182 mm at 0.25 MPa, and 233 mm at 0.3 MPa.

## **Subsection IV.4.2 Measurement of the restoring angle and force using the pneumatic artificial muscle.**

In this subsection, the effect of the shape-restoring actuation by the pneumatic artificial muscle is evaluated by measuring the restoring angle and force when the inner segment diameter and flow rate are varied. The restoring angle and restoring force are expected to increase as the flow rate with the valve opening ratio. This is because the restoring angle and the restoring force depend on the actuation time.

Fig. 68 shows the devices used to measure the restoring angle and force. In this experiment, the experimental device used to measure the holding torque in the pitch direction is rotated by 90°, and the restoration effect is measured using motion capture. Markers were attached to the tip of the segment, and their trajectories were recorded by a motion capture system (OptiTrack Flex 3, Acuity Inc., Japan). A speed controller for air pressure (IB-Series IB-Flow Takt Time Controller, Koganei, Japan) was used to control the valve opening. The flow rate of air at each valve opening was measured with a flow meter (PFM711S-C6-A-M, SMC, Japan).

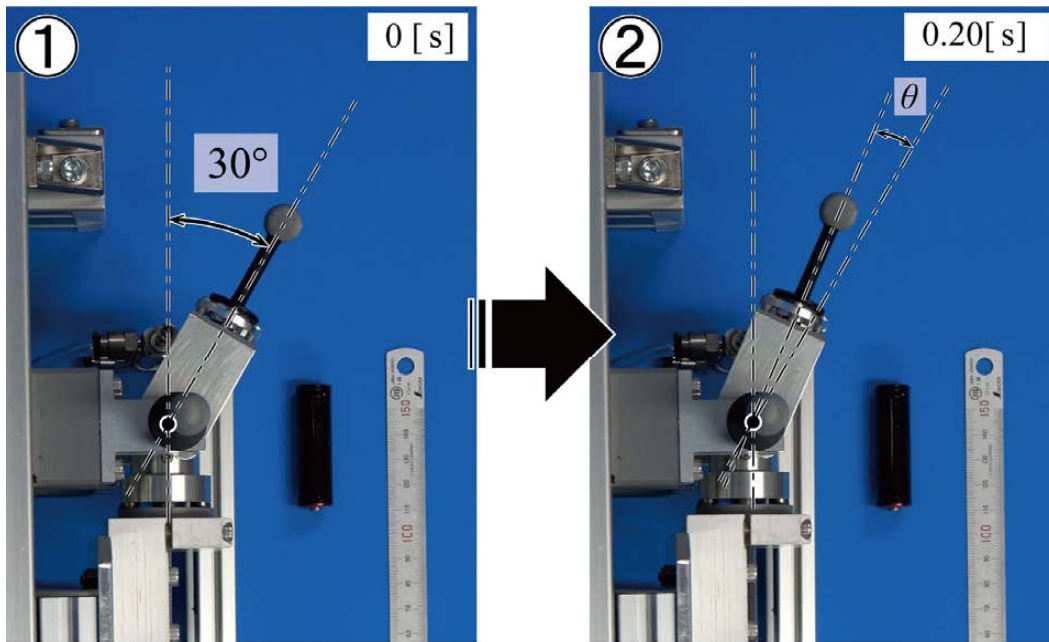
The restoring angle and force at each valve opening and segment inner diameter were measured five times. The restoring angle  $\theta$  is defined from the rotation central axis to the position to which the arm is moved by pressurization (Fig. 69). The restoring force is calculated by measuring the acceleration using motion capture and multiplying the acceleration by the mass of the segment. The angles and forces restored by the pneumatic artificial muscles during pressurization were both measured. I used a cylinder to stop the rotation of the segment during non-pressurization. By pressurizing the pneumatic artificial muscle and the cylinder at the same time, the restoration effect of the pressurized pneumatic artificial muscle was measured while removing the restraint on rotation.



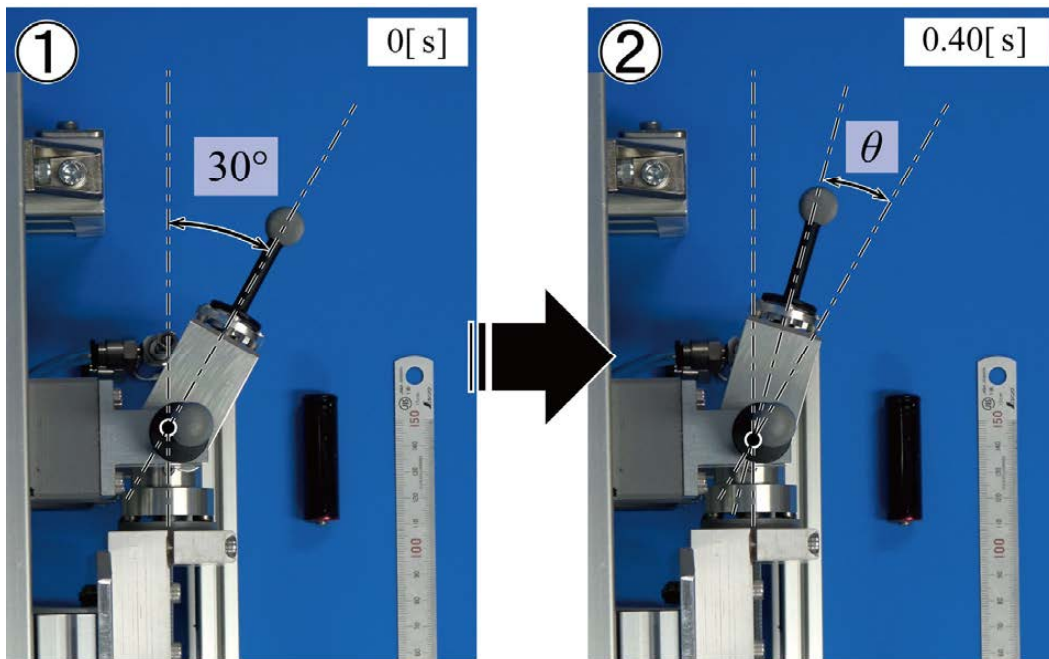
**Fig. 68** Experimental device for measuring the restoration angle and force using the pneumatic artificial muscle.

Experimental conditions:

- A pressure of 0.3 MPa was applied.
- The valve openings of the pneumatic artificial muscle were 0, 25, 50, 75, and 100%. The flow rates at each valve opening were 0 L/min (0%), 4 L/min (25%), 8 L/min (50%), 11 L/min (75%), and 14 L/min (100%).
- The valve opening of the cylinder for fixing the rotating segment was 100%. The flow rate was 14 L/min.
- The mass of tip segment is 106 g.
- The inner segment diameters were 5, 6, 7, 8, 9, 10, 11, 12, and 13 mm.
- The bending angle was 30 degrees.
- The outer segment diameter was 25 mm.
- The axial distance between the segments was 0.5 mm.



(a) The valve opening was 100% when the inner segment diameter is 8mm.



(b) The valve opening was 25% when the inner segment diameter is 8mm.

**Fig. 69 Shape-restoring actuation.** Here,  $\theta$  is the restoring angle, which is defined from the rotation central axis to the position the arm moved by pressurization. (a) The restoring angle decreased when the valve opening is increased. (b) The restoring angle increased when the valve opening is decreased.

Fig. 70 shows the measured values of the restoring angle for each inner diameter and valve opening. The restoring angle increased when the flow rate was reduced, and the restoring angle decreased when the flow rate was increased. For a low flow rate, the restoring angle was large when the inner diameter was 9 mm or more, while the restoring angle was small when the inner diameter was 8 mm or less.

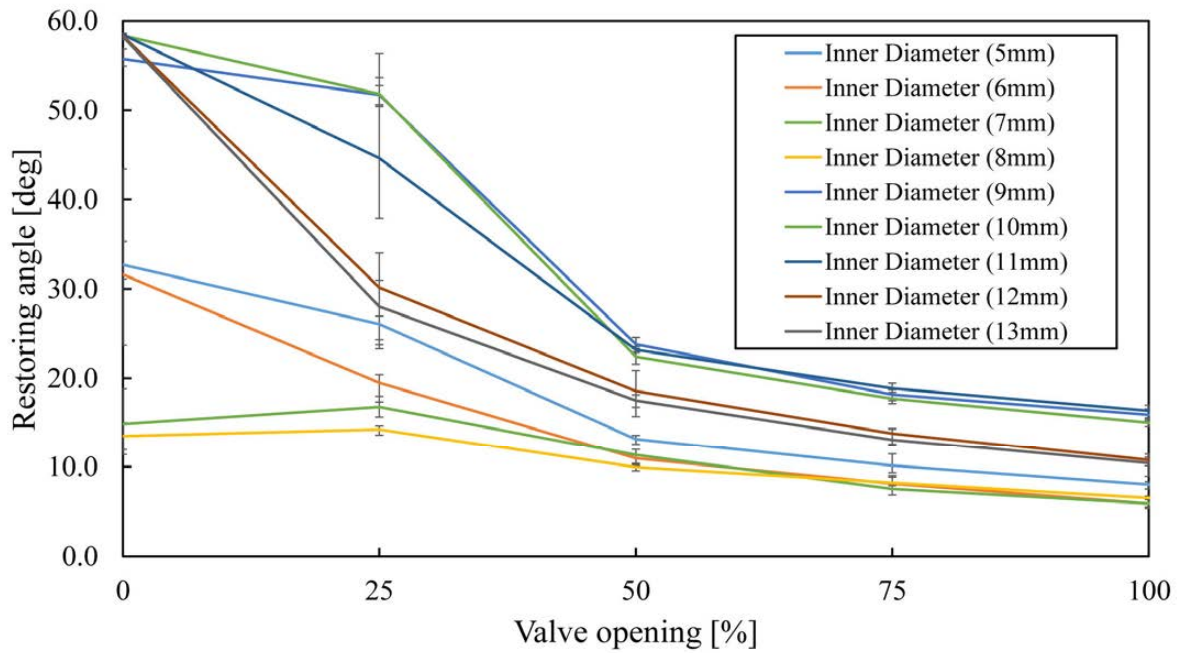


Fig. 70 Results of the measured values of restoring angle  $\theta$ .

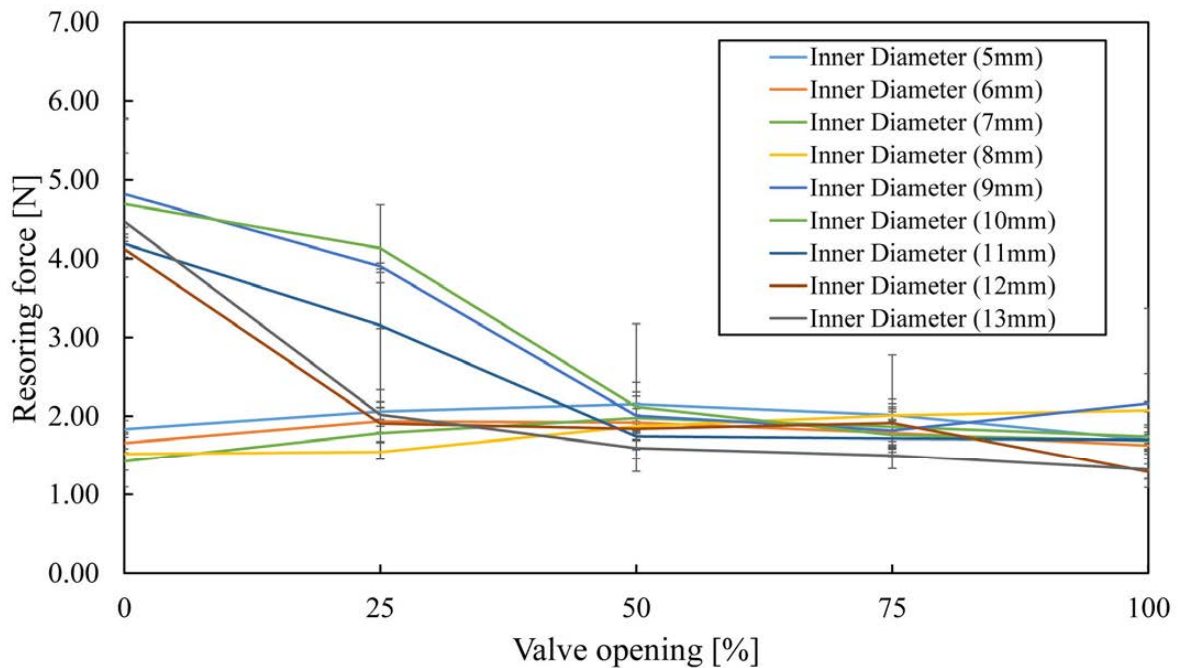


Fig. 71 Results of the measured values of restoring force.

Fig. 71 shows the measured values of the restoring force for each inner diameter and valve opening. For a low flow rate, the restoring force was large when the inner diameter was 9 mm or more, while the restoring force was small when the inner diameter was 8 mm or less. There was no difference in the restoring force when the flow rate was high, regardless of the inner diameter.

The results show that the restoring angle and restoring force depend on the

segment inner diameter. The cause of this difference is thought to be the frictional resistance caused by the pneumatic artificial muscle contacting the inner wall of the segment. In order to enhance the restoring effect, the inner diameter of the segment should be increased to avoid the pneumatic artificial muscles from contacting the inner wall of the segment.

For only one segment, I confirmed a strong restoring effect that allows the shape to be restored to a linear shape from a state bent by 30 degrees. However, for the structure in which multiple segments are concatenated, inertial and friction may resist the segments to become a straight line by single pressurization. Thus, pulse actuation will be one of the solutions to realize this motion (see supplementary video). Also, increasing the diameter of the artificial muscle enclosed inside may improve the shape restoration performance.

## **Section IV.5 Discussion of Chapter IV.**

A parameter that affects the shape-restoring actuation is the distance between the segments in the axial direction, and changing it could be considered in addition to the method described in Subsection IV.4.2 to measure the restoring angle and force. Furthermore, because the time until the contact force is generated can be adjusted by changing the distance between the segments, the distance between the segments in the axial direction is an effective method for increasing the restoring angle. In other words, it is possible to enhance the performance of the shape-restoring actuation by increasing the distance between segments and reducing the flow rate of air.

To do this, it is thought that a tensioner mechanism that can arbitrarily adjust the distance between segments is required. Increasing the inter-segment distance means that the contraction rate of the pneumatic artificial muscle increases and the holding torque decreases. Therefore, it would be necessary to implement a function to arbitrarily switch between shortening the inter-segment distance when a high holding torque is required and increasing the inter-segment distance when a high shape-restoring actuation is needed.

It is thought that implementing a tensioner mechanism can solve the limitations of the current prototype. The limitations are that the prototype does not return to

its initial shape and the possibility that the locking of an arbitrary shape might be hindered by the restoration operation. The restoration effect is easy to work around if there is a gap between the segments. In contrast, the absence of a gap can reduce the restorationability through a pressing force that does not hinder movement during flexing of the prototype. In other words, inputs other than that provided by the pneumatic artificial muscles is required to eliminate the restoration angle.

It is an application goal for the link structure connecting the segments, but it is also applied to grippers. When this mechanism forms a branch structure, a variable stiffness is possible to be provided to the entire structure using a single actuator, so the proposed mechanism can be applied to soft grippers. In addition, by enclosing the pneumatic artificial muscle inside this branched structure and changing the flow rate of each of the pneumatic artificial muscles, it is thought that the amount of displacement when the branched link structure moves will differ.

## **Section IV.6 Conclusion of Chapter IV.**

In this chapter, I developed a new fluid-driven mechanism that switches stiffness via friction through positive pressurization of a McKibben pneumatic artificial muscle. The proposed mechanism consists of a pneumatic artificial muscle enclosed in a link structure of connected hollow segments. This mechanism not only provides such variable stiffness by applying positive-pressure but also enables the actuation from a curved shape by adjusting the flow rate of air.

This chapter evaluated the effect of pneumatic artificial muscles on the holding torque when the joint angle is horizontal, by measuring the holding torque when the segment inner diameter and internal pressure are changed. The torque in the bending direction due to friction when internal pressure and inner segment diameter were changed was measured, and it was confirmed that the error between the measured and theoretical torque value was within 20% at any inner diameter.

Moreover, the restoring angle and force when flow rate and inner segment diameter were changed were measured. I confirmed an un-precedented function that can change the shape restoration characteristics by changing the flow rate



with a single rubber tube.

In the future, I will design a tensioner mechanism for arbitrarily changing the distance of the segments in the axial direction. Additionally, it will be necessary to investigate the holding torque, restoring angle and force when the distances of the segments are changed. Also, it is necessary to perform an FEM analysis on the torque when the joint angle, frictional force between the McKibben pneumatic artificial muscle and the inner wall of the segment, and frictional force between individual segments are changed as well as for the shape-restoration.

## Chapter V

Pneumatic Driven Hollow Variable  
Stiffness Mechanism Aiming  
Alternately Insertion of Telescopic  
Guide Tubes

# **Chapter V      Pneumatic Driven Hollow Variable Stiffness Mechanism Aiming Alternately Insertion of Telescopic Guide Tubes**

## **Section V.1      Abstract of Chapter V.**

The proposed mechanism, which utilizes positive-pressurization and friction, enables the distribution of the working fluid across the entire device with a single actuator based on the flow path design, facilitating its application to various configurations like elongated (snake-like), branched, and planar structures, as depicted in Fig. 72. The locking function is preserved regardless of changes in the volume or structure of the locking device. Consequently, it is possible to maintain a high holding force in each of these three structural forms. Although there exists a method to replace the rubber tube used for holding a joint angle at will with a wire, in snake-like forms, shape-holding is possible even with the tension of a single wire. However, the loss of wire tension due to sliding resistance between the joint and wire imposes a limitation on the total length of multi-jointed structures. Moreover, in branched and planar structures, it is difficult to hold all joints with a single wire. While a differential mechanism can be employed in branched and planar structures, the wire-tension decreases as the number of wires increases.

In this study, I focused one of the applications of snake-like forms for aiming to construct the disaster robots with the variable stiffness mechanism using positive pressure. The proposed mechanism maintains stiffness at long distances due to its positive-pressurization-based variable stiffness design.

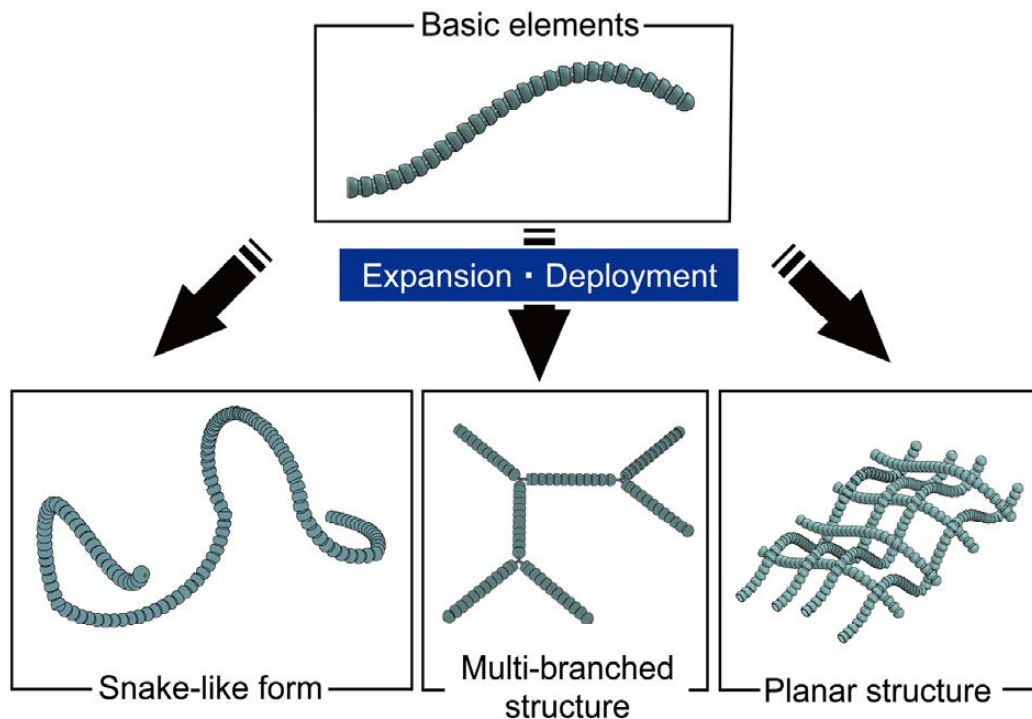
Disaster robots that can work safely and quickly in complex and fragile environments are required for collecting information from debris for initial response and recovery work. Various types of snake-like robots have been proposed with the aim of propelling through the rubble, such as the wheeled, the continuous track, modular articulated, vibrating cilia, and the push-in type that can be inserted into a confined space.

This chapter introduces a novel variation of snake-like push-in types featuring a dual radial-layer structure. This design enables propulsion along an arbitrary trajectory by alternately sliding its two coaxial tubes and modulating their

stiffness through internal pressurization. The innovative variable stiffness mechanism of this design incorporates a hollow structure, which not only simplifies the overall design but also facilitates activation by positive pressure.

The prototype of snake-like forms is consisted of a single rubber tube enclosed inside 3-axis rotary ball joint with slit in the Chapter II. The rationale for using the mechanism proposed in Chapter II, as compared to other proposed mechanisms, lies in its ease of constructing a hollow structure for aiming alternately propulsion. To form a hollow structure while sealing a rubber tube, it is necessary to encase a hose within the tube. However, the mechanism in Chapter III faces challenges in securing space for the hose due to the presence of levers. Furthermore, the mechanism in Chapter IV is difficult to maintain the contraction of artificial muscles on the hose.

A prototype model was developed for evaluating of principle, and the average pulling forces required to actuate either the inner or the outer tube when the other tube is bent at 1/225 and fixed were measured to be namely 67.6 N and 5.66 N, respectively. This evaluation experiment validated the proposed principle of contactless propulsion mechanism.



**Fig. 72 Applications of the proposed variable stiffness mechanism via friction and positive-pressurization.**

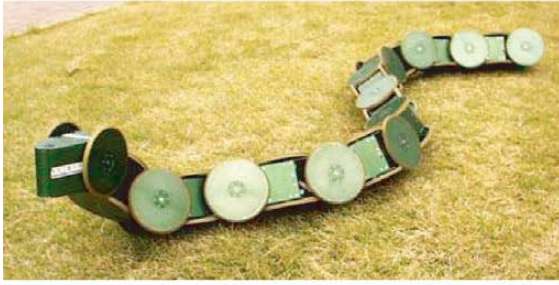
## Section V.2 Application examples of snake-like robots with the variable stiffness mechanism using positive pressure.

When a natural or a human-made disaster, it is necessary to collect information from the collapsed buildings and the debris for the initial response and recovery work. For the purpose of safety, it is not advisable for humans to enter such complex and fragile environments and pass through the heavy debris. Therefore, there is a need for robots that can work safely and quickly [122].

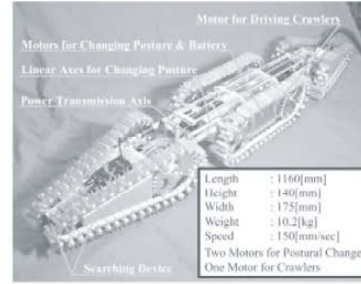
Snake-like robots can enter confined spaces because of their long and thin shape during disaster. Research on various snake-like robots has led to their categorization into two primary classes: those guided by virtual tracks and those guided by physical tracks. The virtual track type actively acquires trajectory information by continuously measuring the overall posture of the snake-like form during propulsion. In contrast, the physical track type passively obtains trajectory data using a snake-like form with higher rigidity.

One example of the virtual track type is the wheel-type [123][124] (Fig. 73(a)), crawler-type [125][126] (Fig. 73(b)), modular type [127][128] (Fig. 73(c)), ciliated vibrating type [129]. The wheel, crawler, modular-type can be propelled in an uneven environment by controlling the joint angle of the robot according to the three-dimensional shape of the ground. As a ciliated vibrating type, Tadokoro et al. proposed an active scope camera [129] (Fig. 73(d)) has inclined cilia on the entire surface of the body and is propelled by vibration while crawling on the ground. This robot type can be constructed with a smaller diameter and lighter weight compared to wheel-based, crawler, or modular types.

Conversely, within the realm of physical track types, the push-in type has been introduced as a methodology for snake-like robots. One of the push-in type robots, the rescue manipulator [114] allows for the left and right manipulators to be pushed alternately to propel the robot in any direction, by using the duplex mechanism (Fig. 74). One of the drawbacks of this type is the complexity of the structure owing to the large number of parts and the difficulty in protecting the sliding parts with a dustproof cover. There is also a pre-bent telescopic tube [130] depicted in Fig. 75. This allows propulsion along any trajectory by alternately



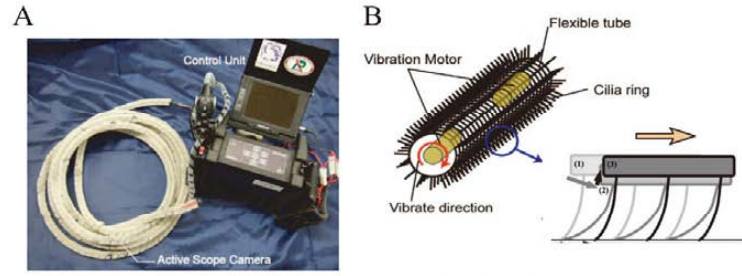
(a) Wheel-typed snake robot.



(b) Crawler-typed snake robot.



(c) Modular typed snake robot.



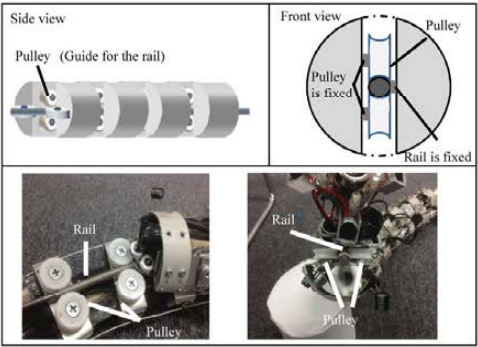
(d) Ciliated vibrating typed snake robot.

**Fig. 73** Previous snake-like robots have been proposed with the aim of propelling through the rubble, such as the wheeled [123], the continuous track [125], modula robots [127] and the vibrating cilia [128].

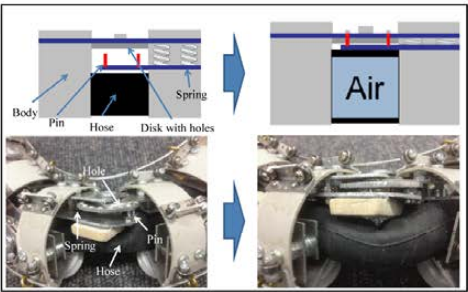
pushing coaxial tubes and twisting them. However, as it doesn't offer variable stiffness, the tube needs to be pre-bent just before pushing. Then, there is the robotic catheter navigation [131] shown in Fig. 76. This technique permits the tube's stiffness to be changed by pulling a wire threaded through multiple beads. By pushing the articulated structures in alternation, the robot can move in any trajectory. However, similar to the semicircular duplex manipulator [130], the left and right manipulators are alternately pushed in, leading to an issue where stiffness becomes anisotropic based on the bending direction.

In this chapter, I focused on the basic push-in type robot and developed a snake-like robot with a two radial-layer structure. This robot is propelled on an arbitrary trajectory by sliding two coaxial tubes alternately and switching stiffness with the help of internal pressurization. This robot is assembled by connecting hollow ball joints with rubber tubes inside. The tip of the robot can be actively bent by applying tension in a wire. The tubular variable stiffness mechanism is newly proposed and, owing to its simple configuration, positive pressure fluid drive, and a hollow structure, this snake-like robot has the following functions that were not previously available: (i) The structure makes it easy to pass through cameras,

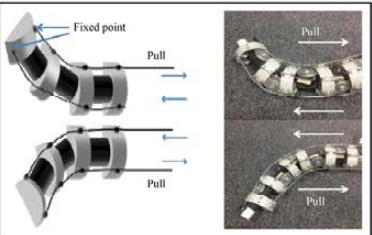
LEDs, wires, and actuators, simplifying the process of adding cable parts. (ii) It can steer and propel in any direction in three-dimensional spaces, and can be propelled without any contact with the environment. (iii) The supply pressure of a single chamber can adjust all the joints of the robot to a uniform stiffness. In addition, since a positive pressure is used instead of a negative pressure, there is no limit to the supply pressure in principle. (iv) Due to the absence of a motor in the body, it is lightweight and therefore, it is easy to develop a structure which is waterproof and dustproof.



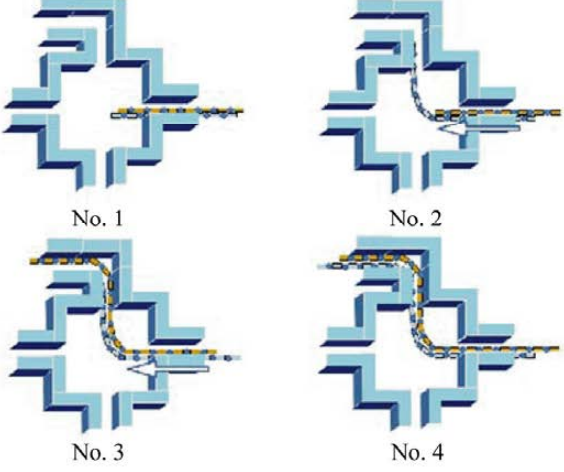
Proposed duplex mechanism.



Locking mechanism.



Direction control.



Movement of the proposed manipulator.

**Fig. 74 Semicircular duplex manipulator.**

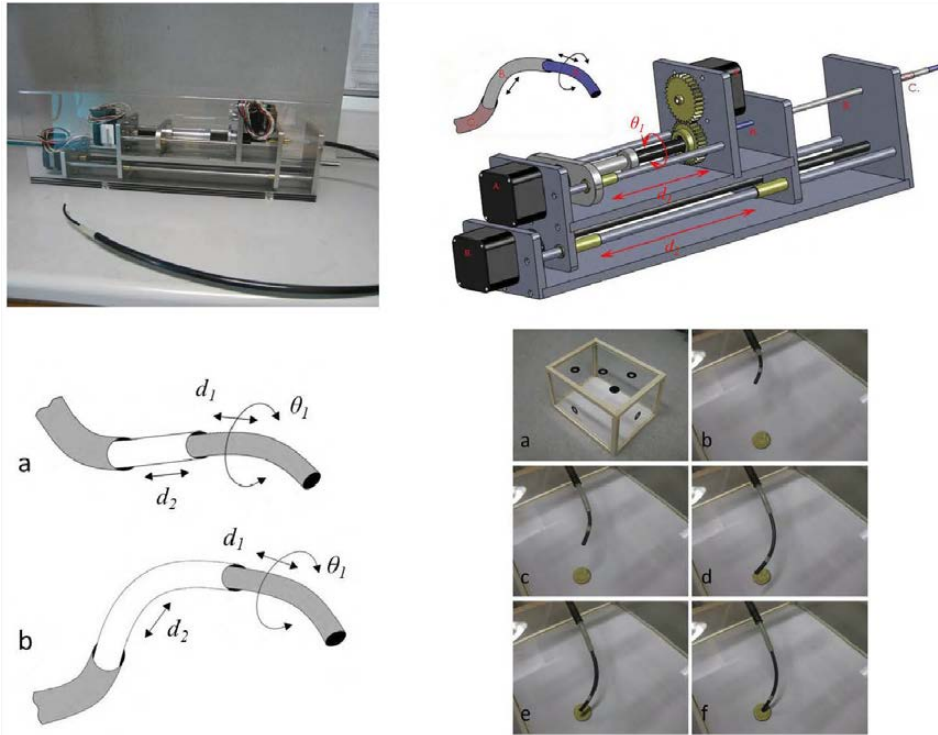


Fig. 75 Pre-bent telescopic tube.

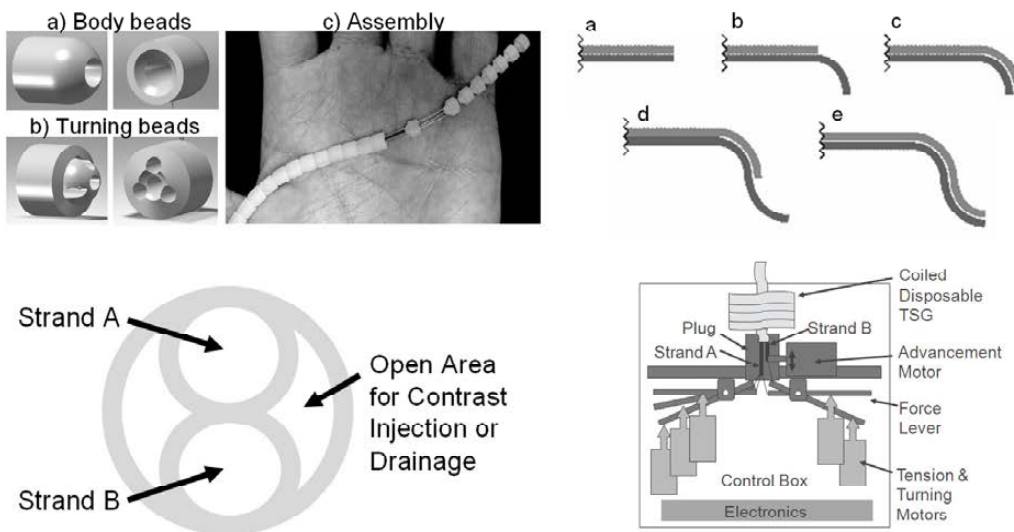


Fig. 76 Robotic catheter navigation.

### Section V.3 Basic principle of propulsion method with the variable stiffness mechanism.

As this configuration does not come into contact with the environment, I focus on a propulsion system with two variable-rigidity structures connected by sliders, which propel and change the stiffness alternately. This method is also used in the duplex mechanism [130], where a variable-rigidity structure is successfully propelled by alternately pushing out the left and right variable-rigidity structures.



In this chapter, I consider a method which differs from conventional methods in that it uses a variable stiffness tubular structure with inner and outer tubes which coaxially slide on each other. Fig. 77 shows the configuration of the mobile unit used to achieve this operation. It consists of outer and inner variable stiffness tubes where the diameter of the inner tube is slightly smaller than that of the outer tube. Either end has an active bending mechanism that can curve in an arc shape. Variable stiffness tubes have high stiffness in any direction when the rigidity is high. Conversely, in the case of low rigidity, the stiffness is reduced in the bending direction, but the longitudinal stiffness remains high. In addition, the coefficient of friction between the inner and the outer tubes is small, and they slide easily.

The coaxial structure has various advantages in terms of design, function, and performance. For example, a simple thin PTFE-coated tube can be used to slide the two variable stiffeners, eliminating the need for bulky guide parts and rollers as used in [130]. Additionally, there is no anisotropy in the bending stiffness depending on the bending direction. Furthermore, the push-in lengths of two variable-stiffness structures are equal regardless of the trajectory, which facilitates the control of the amount of push-in. However, since the diameters of the inner and the outer tubes are different, the bending rigidity varies between the tubes, and this needs to be considered in the design and the operation.

Based on this configuration, Fig. 78 shows the principle of the slide motion for moving on an arbitrary trajectory. The active bending mechanism is connected to the inner tube. Initially, the active bending mechanism is carried out in accordance with the direction of the propulsion. Next, the stiffness of the inner tube is increased, and the outer tube with lower stiffness is pushed out to the tip of inner tube. Then, the stiffness of the outer tube is increased, and the inner tube with lower stiffness is pushed out. Thereafter, these actions are repeated.

The curving mechanism bends in an arc, which propels the object along a trajectory of interconnected arcs. Therefore, the smaller the amount of bending of the inner tube, the smoother the trajectory that can be drawn. The trajectory is not limited to a two-dimensional plane and is also applicable in three-dimensional space.

In this study, the variable stiffness mechanism using friction and positive-

pressurization consists of a single rubber tube enclosed inside 3-axis rotary joint is applied to for switching the stiffness of a snake-like robot. Because of the using proposed mechanisms, the conditions required for a variable stiffness mechanism are, that its rigidity does not decrease even if it is extended over a long distance, that a hollow structure can be constructed, and that a high rigidity can be achieved.

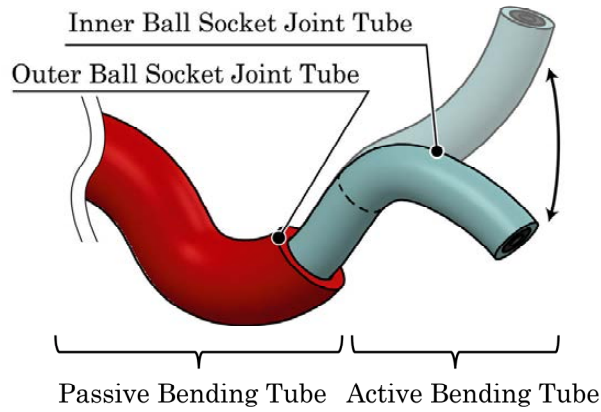


Fig. 77 Basic configuration of the proposed robot.

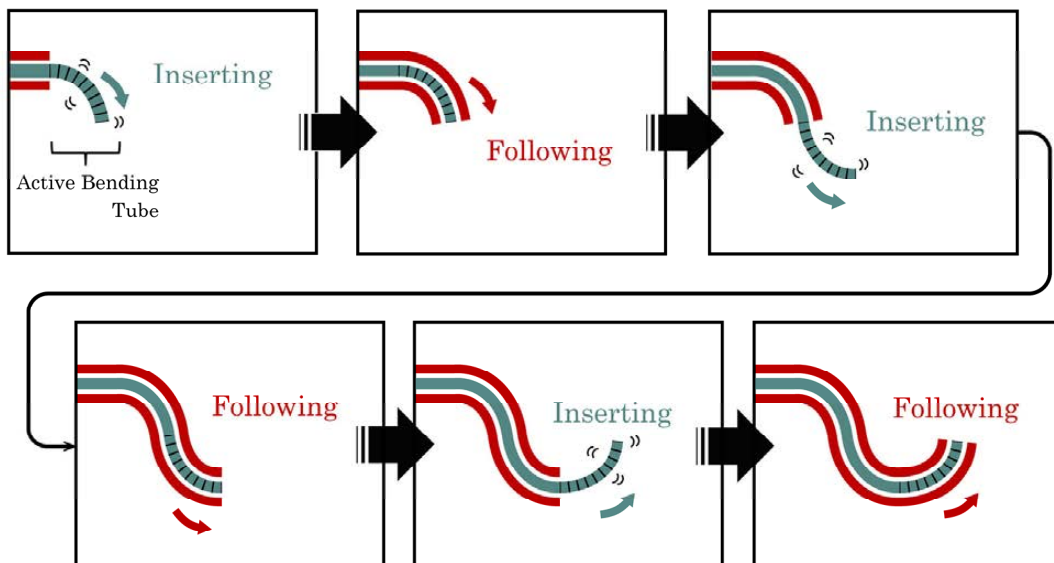


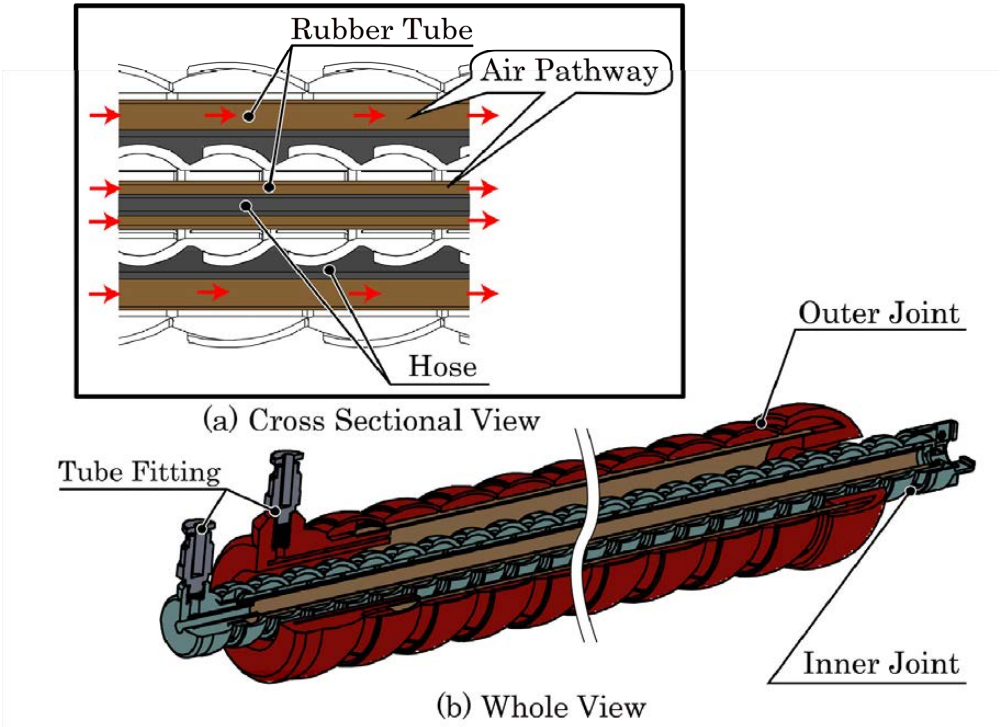
Fig. 78 Steps for sliding motion.

## Section V.4 Mechanical design of prototype with the variable stiffness mechanism using positive pressure.

The joint was designed and the first prototype model of a snake-like robot with a two radial-layered structure was realized. The specifications of the prototype model (Table XV), its cross-sectional view, and the air infiltration path are shown,

respectively (Fig. 79). The joints of the single variable stiffness tube used in the prototype were made of acrylic resin and were 3D-printed. An elastic tube made of natural rubber is enclosed in the tubular body to keep it airtight. In addition, a hose is placed inside the rubber tube through which the variable stiffness tube passes. The inner variable stiffness tube consists of a metal coil-filled hose and the outer one contains a duct hose from the tip to the root. Since the configuration requires the addition of pressurized air between the rubber tube and the hose, it is necessary to use a hose that does not easily buckle towards the inner radial direction due to the pressure. The inner variable stiffness tube does not collapse when external pressure of 0.2 MPa is applied. Since the duct hose used in the outer variable stiffness tube has a larger diameter than the inner tube and is more collapsible, it can be applied only up to 0.1 MPa.

The prototype was fabricated using the following process. First, a rubber tube is glued to the hose through which the variable stiffness tube is passed, and a cap



**Fig. 79** Cross-sectional view and air infiltration path of the prototype internal/external slider.

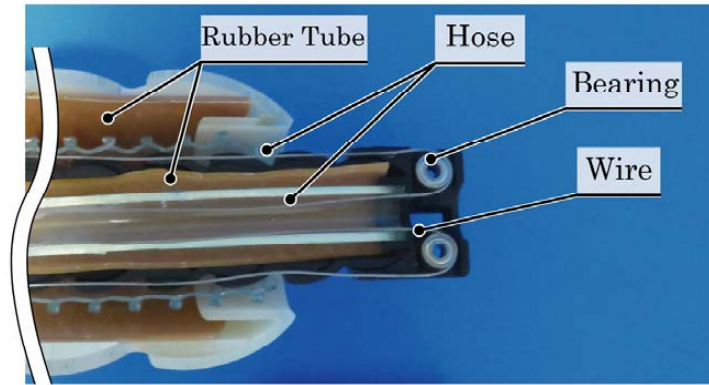


Fig. 80 Cross-sectional model of the tip-side end.

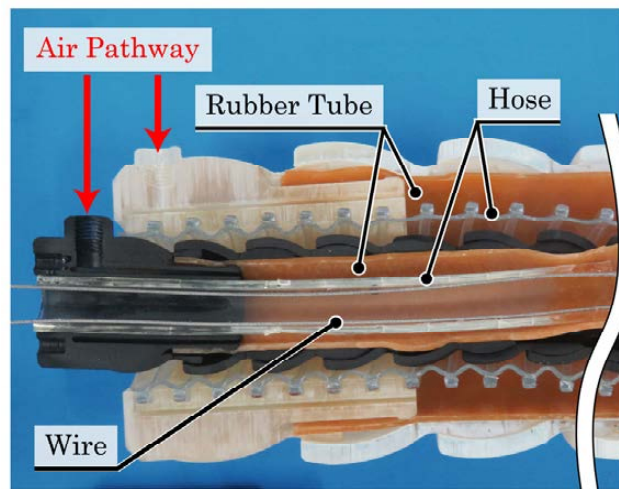
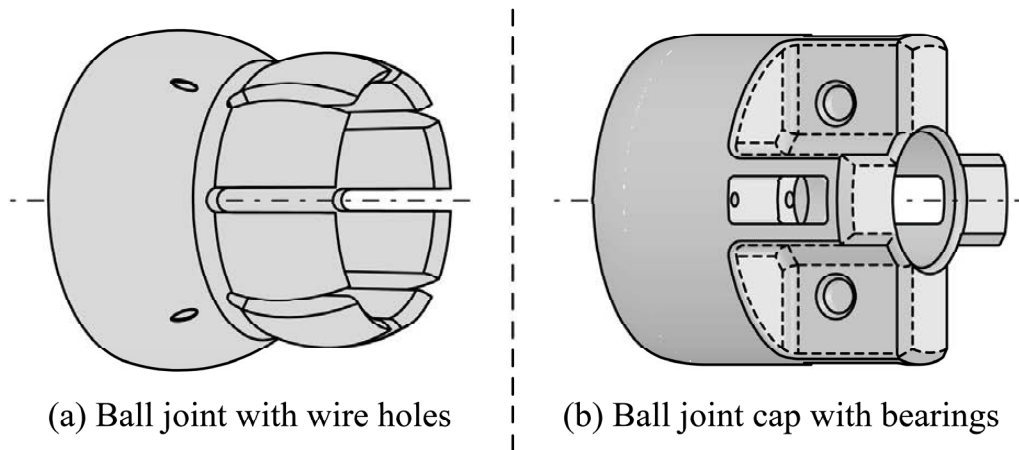


Fig. 81 Cross-sectional model of the root-side end.

**TABLE XV**  
Specification of the prototype.

Inner Ball Socket Joint Tube	Length	1250mm	
	Mass	490g	
	Ruber Tube	Inside Diameter	18.00mm
		Outside Diameter	20.00mm
	Segment	Convex Diameter	25.00mm
		Concave inner Diameter	25.06mm
Concave outer Diameter		29.06mm	
Outer Ball Socket Joint Tube	Length	1000mm	
	Mass	1428g	
	Ruber Tube	Inside Diameter	50.00mm
		Outside Diameter	52.00mm
	Segment	Convex Diameter	60.00mm
		Concave inner Diameter	60.04mm
Concave outer Diameter		68.04mm	



**Fig. 82 Joint and cap used in the active curved part of the inner tube.**

with a rigid hemisphere is attached to the end of the hose (Fig. 80). Next, the radially expandable hemisphere of the joint is inserted into the rigid hemisphere of the cap. Finally, the seals are maintained by gluing the roots of the rubber tube and hose to the joint with the tube fitting, as shown in Fig. 82.

As shown in Fig. 80 and Fig. 82, the inner variable stiffness tube has a hole in the joint that is used in the active curvature of the inner variable stiffness tube to pass a wire through. The wire is fixed at one end by a joint 250 mm from the tip and bent back through a bearing at the tip to the root. The wire is then passed through a coil-filled hose, and the tip of the inner variable stiffness tube is actively bent by pulling the wire at the bottom. The wire is better suited to be installed and passed inside the hose through the joint owing to its compact design. Therefore, it is passed through the inner tube and not the outer one.

## **Section V.5 Experiment for evaluating of basic principle.**

### **Subsection V.5.1 Required pulling force to insert the tube in the other bent tube.**

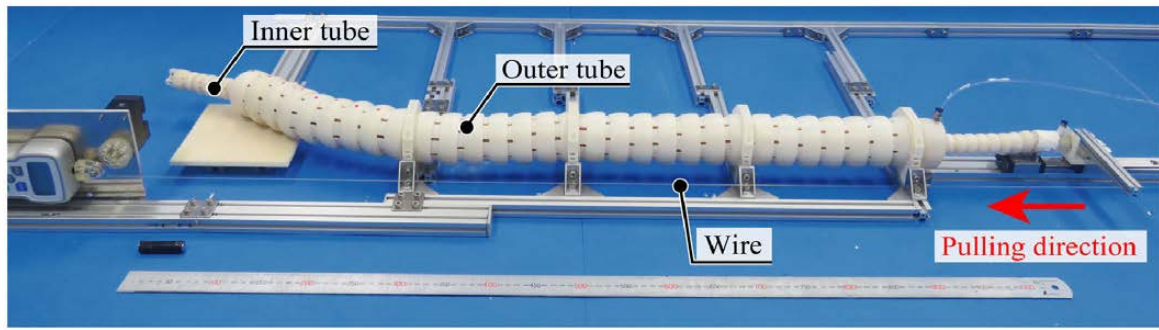
There is a concern that a large amount of friction may occur between the inner and outer tube when they are slid along the curved shape. Therefore, I measured the pulling force generated when the tube is slid along the curved shape in a two-dimensional plane, as shown in the Fig. 83 and Fig. 84.

The base of the tube and the arm are fixed to a linear guide, and one end of the wire is attached to this arm. The wire is then wound by a motor to slide the tube. A force gauge is used to measure the tension generated when the wire is wound up.

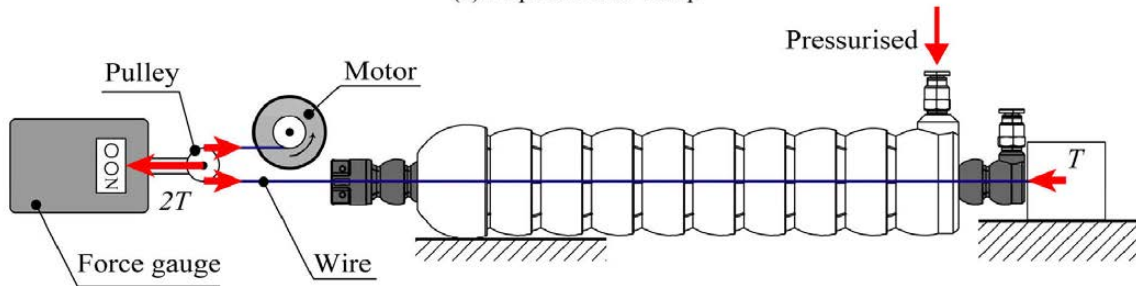
To reduce the friction, talcum powder was applied to the inner layer of the hose, through which the tube passes, and a PTFE coated sheet was placed on the contact surface between the tip of the tube and the floor. The outer tube is clamped to the base at equal intervals beginning at 250 mm from the tip to the root.

(i) Measuring Method:

- The joint is locked by filling air into the rubber tubes enclosed in the inner and the outer tubes causing them to expand. A pressure of 0.2 MPa is applied to the inner tube and 0.1 MPa to the outer tube.
- The inner tube is 1.25 m long, and the outer tube is 1 m long.
- The wire is wound up by a motor with a rotation speed of 30 [min<sup>-1</sup>] to slide the tube
- When the inner tube is in a flexible state and the outer tube is in a highly rigid state, the inner tube is pulled in the left direction shown in Fig. 83.
- When the outer tube is in a flexible state and the inner tube is in a highly rigid state, the inner tube is pulled in the left direction shown in Fig. 84.
- The tube is bent at 250 mm from the tip of one end and has four different radii of curvatures (Fig. 85 and Fig. 86): 1/750, 1/450, 1/300, 1/225 to measure the pulling force generated for each radii of curvatures five times and to obtain the average value of the maximum wire tension measured.

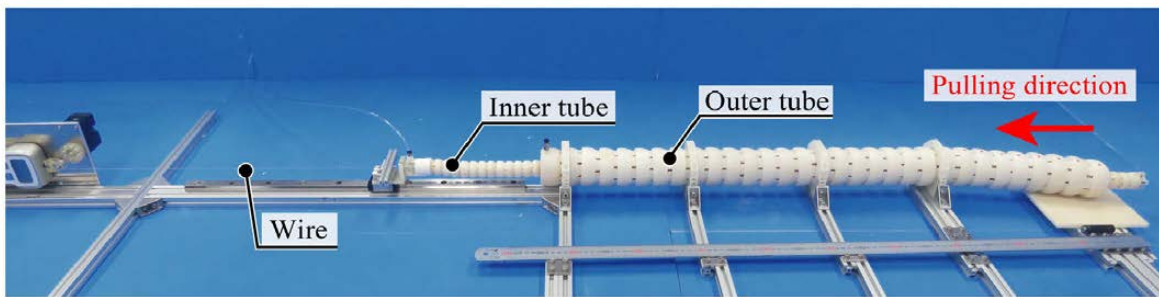


(a) Experimental setup

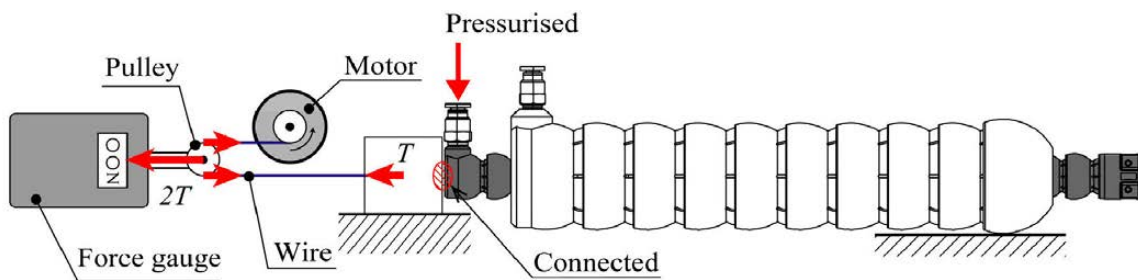


(b) Method of measurement for pulling force

**Fig. 83** Experimental device when the inner tube is in a flexible state and the outer tube is in a highly rigid state.

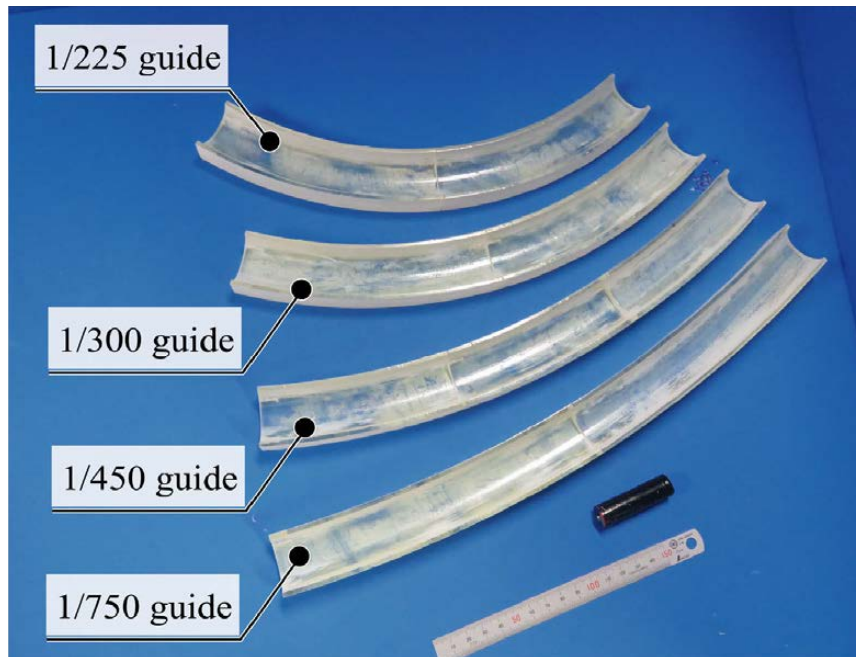


(a) Experimental setup



(b) Method of measurement for pulling force

**Fig. 84** Experimental device when the outer tube is in a flexible state and the inner tube is in a highly rigid state.



**Fig. 85** The guide rail of each radius of curvature.



(i) When the guide rail is used for retaining the outer tube.



(ii) When the guide rail is used for retaining the inner tube.

**Fig. 86** Methods for retaining the tube by using the guide rail.

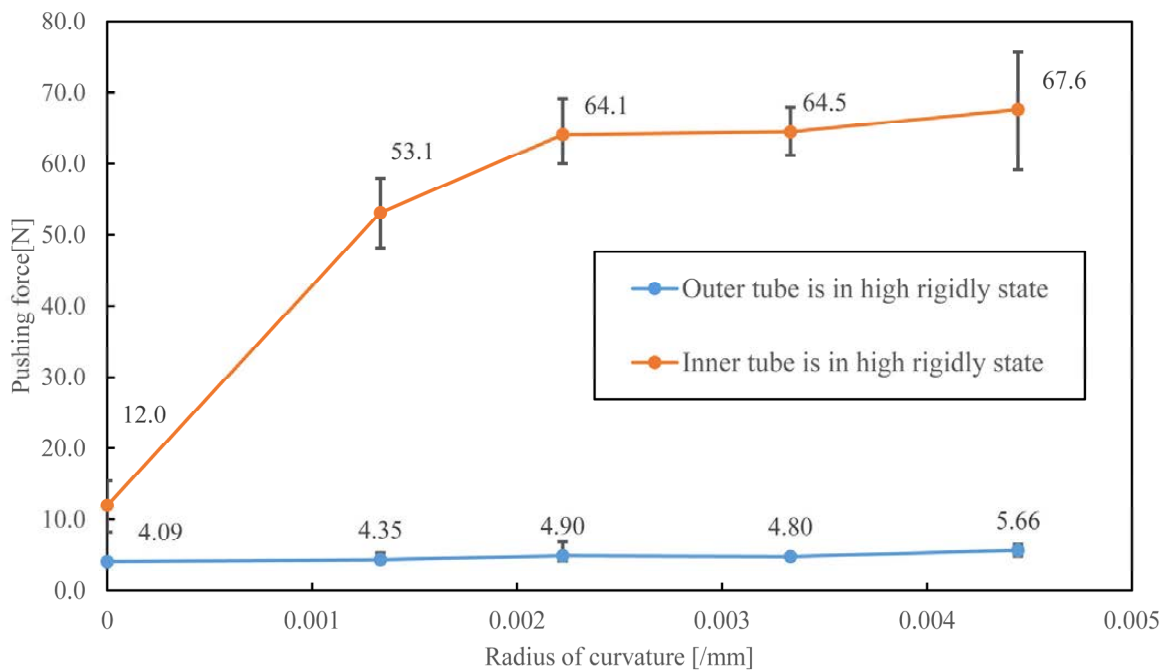
(ii) Results:

The experimental conditions for measuring required pushing force and the measurement results of the pulling force are shown in Table XVI and Fig. 87. The value of the y-axis shown at the origin of the x-axis is the measurement result of the pulling force when the tube is not bent. The error bars show the maximum and minimum experimental values. It was found that the average pulling forces required to actuate either the inner or the outer tube when the other tube is bent at 1/225 and fixed were measured to be namely 67.6 N and 5.66 N respectively, and



**TABLE XVI**  
**Experimental conditions for measuring required pushing force.**

Internal Pressure [MPa]	inner	0.2
	outer	0.1
Rotational speed [min <sup>-1</sup> ]	30.0	
Radius of curvature[mm <sup>-1</sup> ]	1/750, 1/450, 1/300, 1/225	



**Fig. 87 Relationship between the radius of curvature and required pushing force.**

the pulling force increased when the radius of curvature is larger. The shape of the outer tube can be sufficiently retained the shape against the pulling force generated when inner tube is slid. But the shape of the inner tube is not well the shape against the pulling force generated when the outer tube is in a flexible state and the inner tube is in a highly rigid state, the inner tube is slid.

### Subsection V.5.2 Test on a Curved Narrow Environment.

In order to verify whether a alternately propulsion is possible using the first prototype model, an alternating propulsion test was conducted with an obstacle in place (Fig. 88). A mesh tube was attached to the prototype model to reduce the

friction between the floor and the model because the test was conducted with the prototype model on a plane.

It was found that the prototype model can be propelled without touching an obstacle, when a pressure of 0.2 MPa is applied to the inner tube and 0.1 MPa is applied to the outer tube, by alternately switching the inner and outer rigidity of the slide.

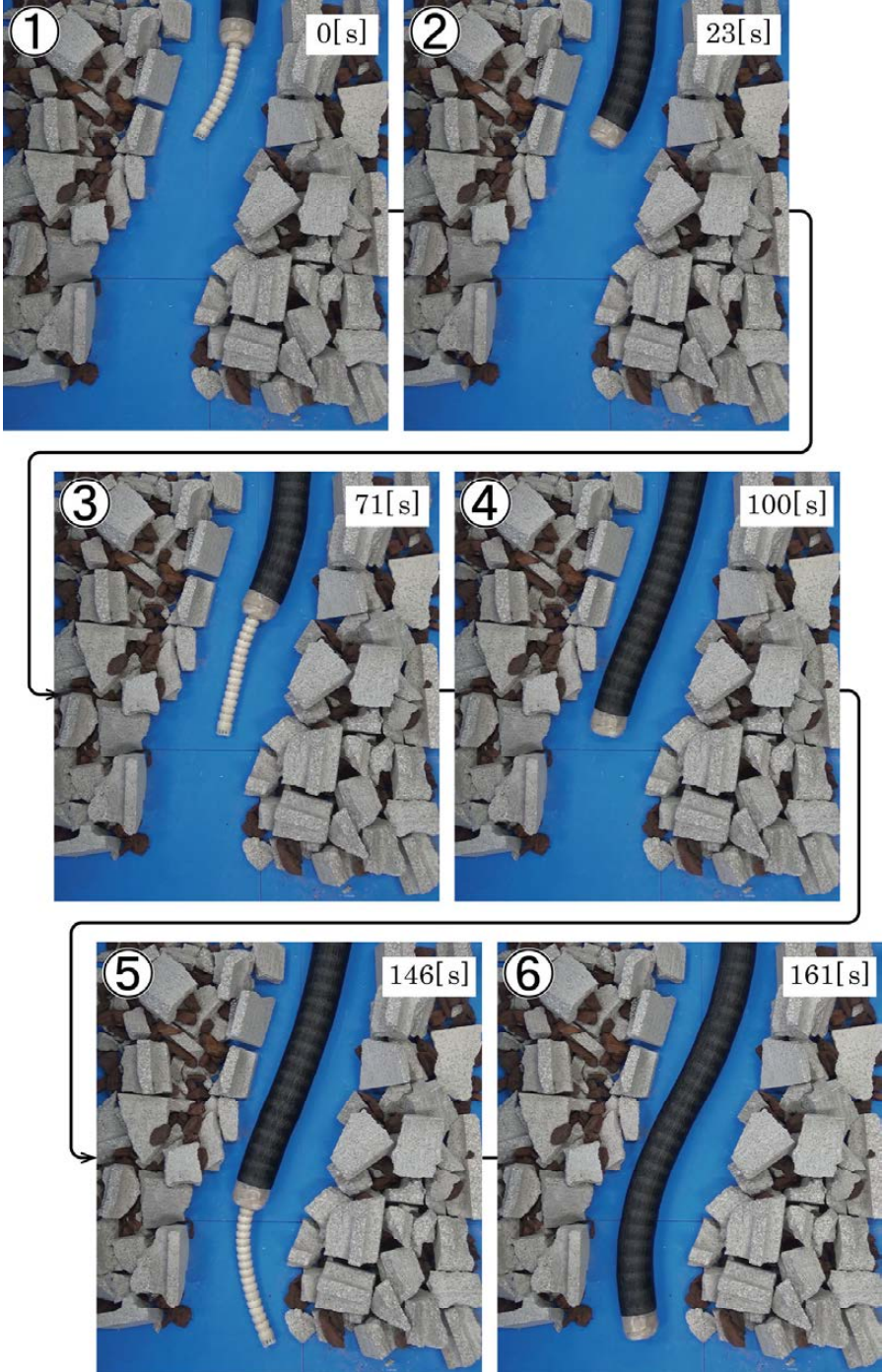


Fig. 88 Test on a curved narrow environment. 1,3,5 : the inner tube is in a flexible state and the outer tube is in a highly rigid state. 2,4,6 : the outer tube is in a flexible state and the inner tube is in a highly rigid state.

## Section V.6 Discussion of Chapter V.

To reduce the resistance, it is necessary to construct a snake-like form with no steps. This is due to the small holding torque as well as the large resistance generated between the inner and outer tube surfaces when they are alternately slid. This is because the surface of the prototype model is slightly uneven and hangs down under its own weight, which can easily get stuck in the tip of model.

In addition, even if the resistance force generated between the tube surfaces is small, as shown in Fig. 87, when the curvature of the trajectory is large, a large pushing force is required at the root of the tube. If the resistance force generated between the tube surfaces is too large, the method of attaching the rollers to the model, rather than slipping and reducing the resistance force by friction is also considered.

The tube does not draw a complete arc but rather, an approximate curve of the arc by the repetition of the bending of each joint. Since it is difficult to align the central axis of the tube, that the trajectory of the movement can shift slightly when the alternate sliding is repeated. Attaching a cilium to the surface of the tube enables the alignment of the central axis.

One of the drawbacks when the tube is moved in the air is that a large moment is applied to the root of the tube. Therefore, it is also considered to be effective to ground the tip at regular intervals before it reaches the limit of the holding torque. The feasibility of this method needs to be verified in the future.

Due to the geometric constrains of the joint design, the current maximum bendable radius of curvature is  $1/225$ . The radial expandable hemisphere is extended longitudinally in order to increase the curvature of the tube. However, it is difficult to assemble the rigid hemisphere owing to the lack of space for the rubber tubes and hoses, and the small diameter of the entrance to the rigid hemisphere. Therefore, it will be difficult to extend the radially expandable hemisphere further in the future.

When retrieving the robot inserted in the debris field, it is possible in principle to avoid touching the debris by pulling the robot while alternately switching the stiffness.

## Section V.7 Conclusion of Chapter V.

In this chapter, a snake-like robot is devised, with two fluid-driven tubular variable stiffness mechanisms in the radial direction, capable of alternately propulsion by mutual sliding. The basic principles of alternately propulsion and the fluid-driven tubular variable stiffness mechanism are presented.

In order to verify whether an alternately propulsion is possible using the prototype, first the average pushing forces required to actuate either the inner or the outer tube when the other tube is bent and fixed were measured. Next, the bending angle, at which the tip of outer tube is investigated when the inner tube is propelled. And finally, an alternating propulsion test was conducted with an obstacle in place.

## Chapter VI

### Conclusion and future aspects

## Chapter VI Conclusion and future aspects

### Section VI.1 Overall discussions of proposed mechanism about the holding torque via theoretical comparison.

In this section, to conclude which mechanism among those proposed in Chapters II, III, and IV demonstrates superior holding torque, I perform a theoretical comparison under conditions where internal pressure, joint radius, rubber tube radius, friction coefficient, and angle of shell range to the tip of male joint are standardized. While the theoretical values of torque in Chapter IV were derived using actual measurements of the contraction force of artificial muscles, for the comparisons in this chapter, to align the diameters of the rubber tubes, I refer to the theoretical model of the contraction force  $F_{pneumatic\ artificial\ muscle}$  of McKibben-type artificial muscles, based on reference [132], as detailed in the following equation.

$$F_{pneumatic\ artificial\ muscle} = \frac{\pi}{4} D_0^2 P \left( \frac{1}{\sin \theta_0} \right)^2 \{3(1 - \varepsilon)^2 \cos^2 \theta_0 - 1\}. \quad (51)$$

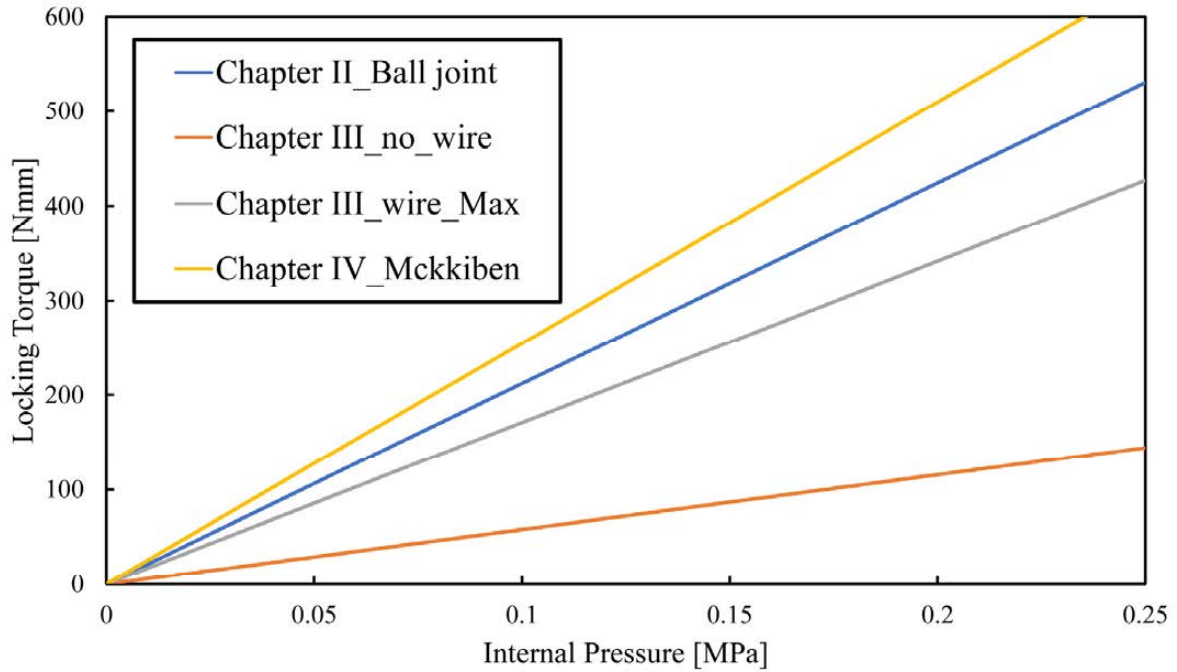
In this context,  $D_0$  represents the initial diameter of the artificial muscle,  $P$  denotes the internal pressure,  $\theta_0$  is the initial knitting angle of the fibers constituting the mesh tube, and  $\varepsilon$  signifies the axial contraction ratio, defined as the contraction displacement divided by the initial length.

The additional conditions pertaining to the artificial muscle when calculating torque are as follows.

- Initial diameter of the artificial muscle : 14 mm
- Initial knitting angle of the fibers constituting the mesh tube : 20 degrees
- Axial contraction ratio : 0 (Constrain the artificial muscle at its initial length)

Furthermore, the internal pressure, as well as the coefficients of friction between the joints and between the wire and the lever, and the angle of shell range to the tip of male joint are set as follows.

- Joint radius: 12.5 mm
- Rubber tube diameter: 14 mm
- Internal pressure: 0.1, 0.125, 0.15, 0.175, 0.2 MPa
- Coefficient of static friction between the joints: 0.3



**Fig. 89 Theoretical comparison of holding torque in proposed mechanisms across chapters.**

- Coefficient of static friction between wire and lever: 0.3
- Angle of shell range to the tip of male joint:  $65\pi/180$

Under the aforementioned conditions, Fig. 89 presents the theoretical values of the holding torque in the pitch direction at each internal pressure for each proposed mechanism when the angle between the joints is 0 degrees. Chapter II involves a ball joint with slits combined with a rubber tube, Chapter III comprises a ball joint without slits coupled with a rubber tube, lever, and wire, and Chapter IV consists of a bowl-shaped joint with a McKibben-type rubber artificial muscle. Fig. 89 displays the holding torque in the pitch direction for each mechanism; however, only Chapter III, due to the anisotropy in torque resulting from its wire arrangement, shows both the maximum torques with wires and the torques without wires.

As evident from Fig. 89, the mechanism combining the bowl-shaped joint with the McKibben-type rubber artificial muscle exhibits superior holding torque. This is attributed to the fact that the huge output force during positive-pressurization is achieved when using artificial muscles. Under the current analysis conditions, the force amplification by the lever used in Chapter III was twofold, whereas the amplification achieved through the artificial muscle was fourteenfold. Additionally,

this mechanism not only provides high holding torque when the angle between the joints is 0 degrees but also prevents the dislocation of the joints.

Furthermore, the mechanism in Chapter IV, characterized by its significant holding torque due to contraction force, is deemed suitable for miniaturization. To enhance the holding torque performance of the mechanisms in Chapters II and III, an increase in the joint and chamber radii is inevitable. However, this increase in radii leads to a reduction in the ratio of holding torque to the weight of the device. In contrast, the use of McKibben-type pneumatic artificial muscles is expected to increase the holding torque relative to weight.

However, it is important to note that in the mechanism of Chapter IV, an increase in the bending angle between the joints may lead to a decrease in the contraction force. An increase in the bending angle fundamentally compresses the enclosed artificial muscle, increasing the initial knitting angle of the fibers and thus reducing the holding torque. While changes in stress do occur with an increase in the bending angle between joints in the mechanisms in Chapters II and III, the use of rubber tubes results in minimal changes in expansion force, thereby mitigating a significant decrease in holding torque.

Furthermore, in the proposed mechanisms, the holding torque due to radial forces decreases as the bendable angle per joint decreases, whereas the holding torque due to axial forces reduces as the bendable angle increases. This is because the radial force is at its maximum when the shell range is at  $\pi/2$ , and the axial force is maximum when the shell range is 0. The proposed mechanisms in Chapters II and III are expected to increase bendable angles per joint, but increasing bendable angles in the Chapter IV mechanism may prove challenging.

Therefore, if concerns such as low holding torque and enlarged joint and chamber radii are not issues and an increase in joint angles is desired, the radial force-based methods of Chapters II and III are recommended, while for scenarios where increasing joint angles is unnecessary and the focus is on miniaturization and high holding torque, the axial force-dependent approach of Chapter IV is advisable.



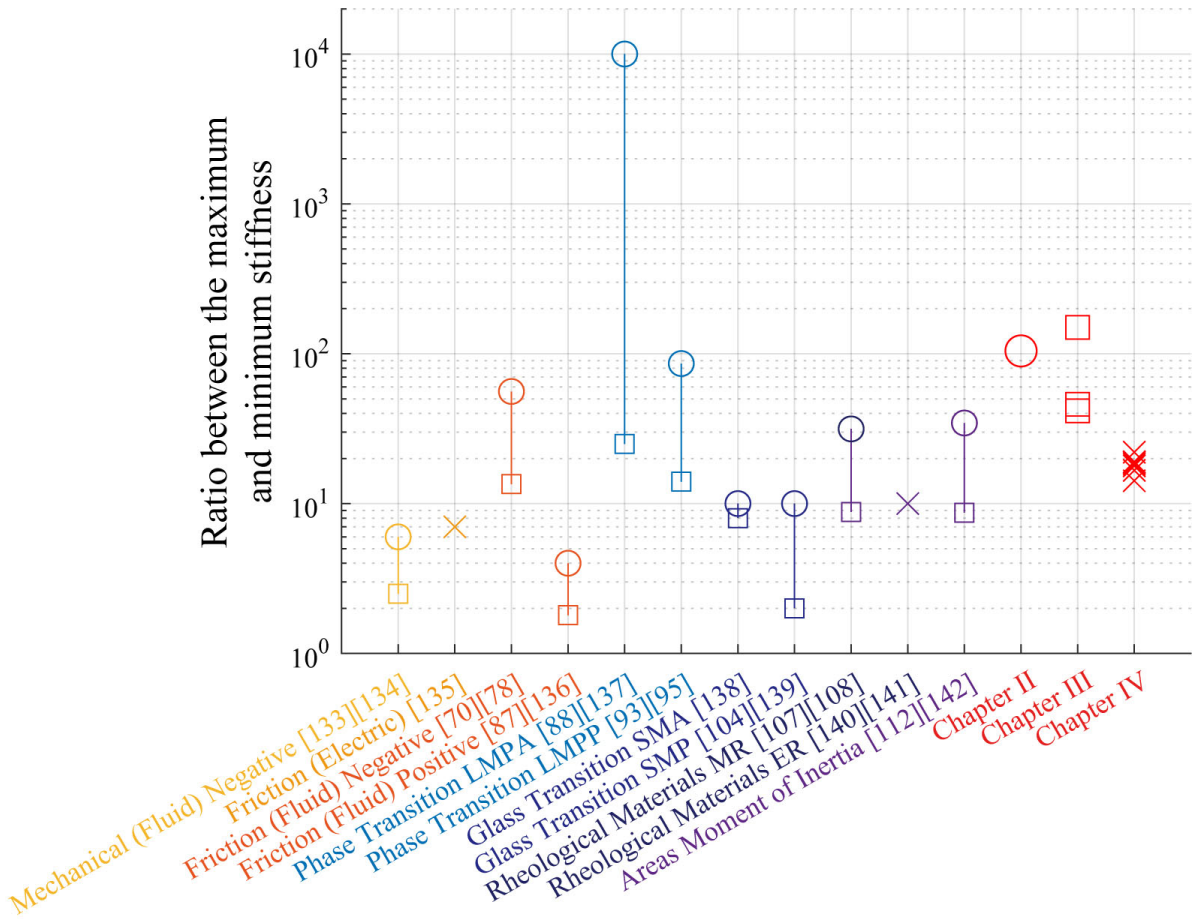
## Section VI.2 Comparison of the previous and proposed methods in terms of the ratio between maximum and minimum stiffness.

This section discusses the comparison of the variable stiffness mechanism ratios between previous methods and the proposed method in this study, both in high-stiffness and flexible modes, and explores approaches to enhance these ratios.

To compare the ratios, the holding torque in the pitch direction at 0 MPa was measured in Chapters II, III, and IV. The measured results showed that the torque in the pitch direction at 0 MPa for Chapter II was 2.54 Nmm, for Chapter III was a maximum (with wire) of 6.61 Nmm and a minimum (with wire) of 17.6 Nmm, without wire was 14.9 Nmm. Also, Chapter IV was 8.02 Nmm (5 mm), 8.99 Nmm (6 mm), 7.79 Nmm (7 mm), 8.46 Nmm (8 mm), 8.36 Nmm (9 mm), 8.28 Nmm(10 mm), 8.32 Nmm(11 mm), 7.93 Nmm (12 mm), 7.35 Nmm (13 mm).

Dividing these values by the maximum holding torque obtained in the actual measurement for each chapter, the ratios are as follows: 104 times for Chapter II, 150 times for the maximum (with wire) and 46 times for the minimum (with wire) in Chapter III, 41 times without wire. Also, 18 times (5 mm), 14 times (6 mm), 19 times (7 mm), 19 times (8 mm), 19 times (9 mm), 19 times (10 mm), 18 times (11 mm), 17 times (12 mm), 22 times (13 mm) for Chapter IV.

Fig. 90 compares the ratio of the proposed method with the ratio between the high-stiffness and flexible modes of the conventional method as shown in Chapter I. The graph indicates that the highest ratio is achieved when using a low-melting-point alloy, attributable to its exceptionally high stiffness. This principle of high stiffness is also applicable to the geometric approach and the second moment of area method. The maximum value of shape-locking force is determined by the stiffness of the components used, and it is impossible to achieve locking forces beyond the yield stress. Moreover, it implies that it is challenging to enhance the locking force up to the yield stress using the friction method.



**Fig. 90** Comparison of the previous and proposed methods in terms of the ratio between maximum and minimum stiffness. In Chapters II, III, and IV, the ratios are determined by dividing the peak actual torque value by the actual torque value measured at 0 MPa.

## Section VI.3 Conclusion of the thesis.

This study focused on the development of a novel variable stiffness mechanism capable of transitioning between different stiffness states. The proposed mechanism is characterized by exceptional design scalability, high and adjustable locking force, and a greater range of deformation. To realize such a high-performance mechanism, I adopted a method that controls the relative positioning of components arranged in opposition, using positive pressure exerted through friction and air. This approach was selected for its capability to design arbitrary flow paths, the high pressure achievable through positive-pressurization, and the incorporation of spherical friction surfaces.

The study aimed to devise a positive-pressure-activated variable stiffness mechanism that utilizes friction and air, demonstrating its potential as a groundbreaking locking device in the field of soft robotics. This objective was

pursued by developing a variable stiffness hose capable of navigating narrow spaces, using the proposed mechanism. The study involved the development of structures that output the friction-based holding force by expansion force during positive-pressurization, a quantitative evaluation of the holding performance in the mechanism, and the construction of a hose with a hollow, multi-layered structure capable of variable stiffness.

Initially, I developed a structure that effectively outputs the expansion force while controlling the expansion deformation of a pressurized chamber. To limit the significant expansion deformation of a rubber tube, components were placed in the direction of the tube's expansion. The holding force through friction is outputted, resulting from the expansion force of the rubber tube, by positioning components with hollow shapes and spherical surfaces on the exterior of the tube. This design ensures that the components contact and lock when the tube expands.

Following this design principle, I conducted a quantitative evaluation of the holding torque for both radially expandable and axial contraction types of the proposed mechanism. Each mechanism is detailed in the subsequent chapters.

**【 Chapter II 】** For the radially expandable type, I designed and fabricated a ball-type joint combining a deflection part and a shell with a rubber tube. This design focuses on ease of assembly, prevention of dislocation during pressurization, and joint holding torque via friction. The holding torque of this mechanism was verified through theoretical modeling, finite element analysis, and empirical measurements, ensuring that the results were consistent within a 30% margin of error.

**【 Chapter III 】** This chapter evaluated the performance of a radially expandable type combining a ball-type joint and rubber tube with a lever for clamping a wire. This study evaluated the holding performance theoretically and empirically, focusing on the anisotropy of the holding torque due to wire arrangement and the comparative analysis of the holding torque with and without the lever. This research confirmed that the theoretical and empirical values of the friction-based holding torque between the ball joints and the lever-wire system were within a 20% margin of error.

【 Chapter IV 】 This chapter quantitatively evaluated the shape-locking and shape restoration performances of the axially contraction type, which combines a bowl-type joint with male and female spherical surfaces and a McKibben-type artificial rubber muscle. The evaluation of the holding torque, based on theoretical models and empirical measurements, confirmed that the discrepancy between the theoretical and empirical values was within 20% margin of error. Additionally, I measured the recoverable angle during varied pressurization flow rates, confirming the feasibility of controlling the restoration angle through flow rate adjustment.

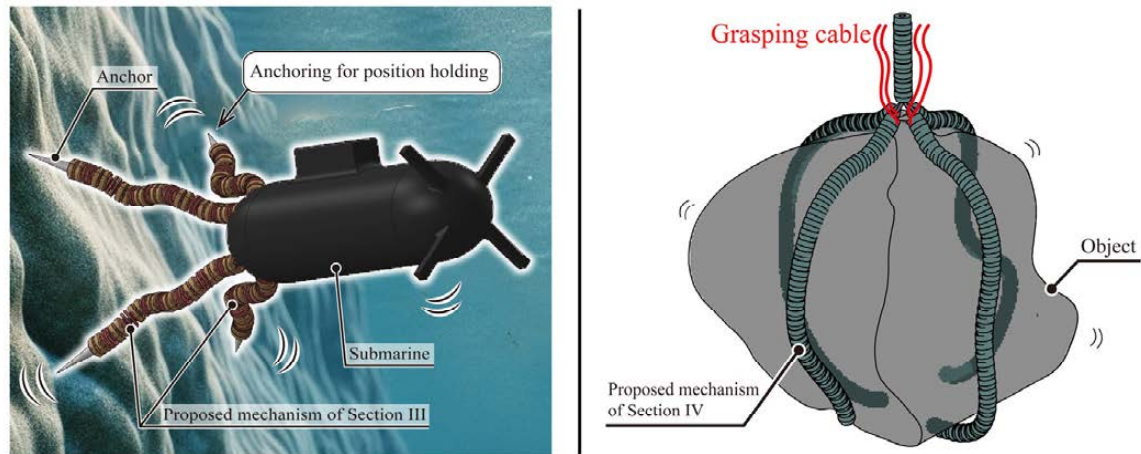
Finally, to assess the propulsion performance of a variable stiffness hose with a hollow multi-layered structure that enables alternating propulsion, I constructed a prototype hose using the radially expandable type. I measured the sliding resistance between hoses during alternating propulsion to validate its effectiveness.

The insights derived from this study substantiate the efficacy of a novel positive-pressurization and friction-based locking mechanism in the field of soft robotics, corroborating its robust locking performance. Moreover, the scalability and adaptability of the proposed mechanism indicate its potential to make a substantial contribution to the evolution of soft robotics. This advancement is projected to broaden the spectrum of applications and enhance interaction capabilities across diverse environments and a multitude of tasks.

## **Section VI.4 Future aspects.**

The proposed variable stiffness mechanism conceived in this study, due to its simple structure, offers high scalability. Compared to traditional methods, it is conceivable to expand its applications not only to lengthening and coaxial multilayering but also to branching and planar structuring. Applications such as soft grippers, which utilize multiple branched linear elements as fingers to conform to the shape of an object and generate high gripping force, and crawlers that conform to road surfaces for enhanced traversability and stability with their planar structure, are also conceivable.

Future work will explore the application and expansion of proposed mechanism



**Fig. 91** The application of the mechanism proposed in Chapter III for above-water and underwater operations using a snake-like form. The application of the mechanism introduced in Chapter IV for underactuated soft grippers without restoring cable.

of Chapter III and IV to robotics elements beyond disaster response snake-like forms with Chapter II and V (Fig,91). The mechanism proposed in Chapter III, while having a multitude of components and a suboptimal torque-to-weight ratio, also features a wire that is clamped by a lever and possesses an active bending function. Consequently, it holds potential for application in both above-water and underwater operations, where the influence of root moment due to its own weight is minimal. The mechanism introduced in Chapter IV operates by pressurizing while altering the flow rate, thereby creating variability in the shape restoration effect of the artificial muscle. This method allows for the achievement of two effects – increased rigidity and actuation – with a single input of pressurization. It shows potential for application in underactuated soft grippers.

Additionally, when quantitatively comparing the holding performance of variable stiffness mechanisms, I believe it is possible to compare not only the ratio of maximum to minimum holding force but also the switching time of the lock. In the future, I plan to conduct quantitative comparisons using both the ratio of maximum to minimum holding force and the lock switching time. When selecting a method for the variable stiffness mechanism, if the length of the switching time is not a concern and the goal is to increase the ratio of maximum holding force to minimum holding force, the low-melting-point alloy (phase change) method is suitable. On the other hand, if the priority is to reduce the switching time over the ratio, the electric or fluidic method is more appropriate. Thus, I believe it is

necessary to expand the criteria for quantitatively evaluating variable stiffness mechanisms beyond the ratio of maximum to minimum holding force and lock switching time, in order to develop indicators for selecting the optimal variable stiffness mechanism method according to the use case.

## ACKNOWLEDGEMENT

First and foremost, I am extremely grateful to my esteemed supervisor and chief inspector, Prof. Tadakuma for his invaluable advice and continuous guidance during my PhD study. His immense knowledge, suggestive ideas and plentiful experience have encouraged throughout the duration of my academic research. I thank Prof. Tadokoro, Prof. Hashimoto, and Prof. Owaki, for their insightful feedback that drastically improved my doctoral thesis.

I thank Prof. Watanabe, Prof. Abe, and all the members of the mechanism team of Tadokoro Human–Robot Informatics Laboratory. Their assistance and support made me enjoy my research and academic life in Tohoku University. Furthermore, I am grateful to the laboratory secretaries. Without their support for the five-years, I would not have completed my research. I would really appreciate if these people kept cheering for me as I am eager to continue giving my best to invent and widespread robotic technology valuable for human society and progress of science as a responsible researcher.

The study was supported by MEXT Grant-in-Aid for Scientific Research on Innovative Areas, Science of Soft Robot Interdisciplinary integration of mechatronics, material science, and bio-computing, Grant Number 18H05471 and JST [Moonshot R&D – MILLENIA Program] Grant Number [JPMJMS2034].

Finally, I would like to conclude the acknowledgement by expressing my best gratitude to my parents, my sister, my grandparents, my uncle and aunt for their tremendous understanding and encouragement.

## REFERENCES

- [1] R. Pfeifer, F. Iida, and J. Bongard, “New robotics: Design principles for intelligent systems,” *Artif. Life*, vol. 11, no. 1–2, pp. 99–120, 2005.
- [2] D. Trivedi, C. D. Rahn, W. M. Kier, and I. D. Walker, “Soft robotics: Biological inspiration, state of the art, and future research,” *Appl. Bionics Biomech.*, vol. 5, no. 3, pp. 99–117, 2008.
- [3] S. Kim, C. Laschi, and B. Trimmer, “Soft robotics: A bioinspired evolution in robotics,” *Trends Biotechnol.*, vol. 31, no. 5, pp. 287–294, 2013.
- [4] M. Plooij, G. Mathijssen, P. Cherelle, D. Lefeber, and B. Vanderborght, “Lock your robot: A review of locking devices in robotics,” *IEEE Robot. Autom. Mag.*, vol. 22, no. 1, pp. 106–117, 2015.
- [5] M. Manti, V. Cacucciolo, and M. Cianchetti, “Stiffening in soft robotics: A review of the state of the art,” *IEEE Robot. Autom. Mag.*, vol. 23, no. 3, pp. 93–106, 2016.
- [6] L. Blanc, A. Delchambre, and P. Lambert, “Flexible medical devices: Review of controllable stiffness solutions,” *Actuators*, vol. 6, no. 3, pp. 1–31, 2017.
- [7] A. Loeve, P. Breedveld, and J. Dankelman, “Scopes too flexible and too stiff,” *IEEE Pulse*, vol. 1, no. 3, pp. 26–41, 2010.
- [8] H. M. Le, L. Cao, T. N. Do, and S. J. Phee, “Design and modelling of a variable stiffness manipulator for surgical robots,” *Mechatronics*, vol. 53, no. May, pp. 109–123, 2018.
- [9] C. Li et al., “A Miniature Manipulator with Variable Stiffness towards Minimally Invasive Transluminal Endoscopic Surgery,” *IEEE Robot. Autom. Lett.*, vol. 6, no. 3, pp. 5541–5548, 2021.
- [10] E. Brown et al., “Universal robotic gripper based on the jamming of granular material,” *Proc. Natl. Acad. Sci. U. S. A.*, vol. 107, no. 44, pp. 18809–18814, 2010.
- [11] J. R. Amend, E. Brown, N. Rodenberg, H. M. Jaeger, and H. Lipson, “A positive pressure universal gripper based on the jamming of granular material,” *IEEE Trans. Robot.*, vol. 28, no. 2, pp. 341–350, 2012.
- [12] G. Fantoni et al., “CIRP Annals - Manufacturing Technology Grasping devices and methods in automated production processes,” *CIRP Ann. - Manuf. Technol.*, vol. 63, no. 2, pp. 679–701, 2014.
- [13] C. Wright et al., “Design and architecture of the unified modular snake robot,” *Proc. - IEEE Int. Conf. Robot. Autom.*, pp. 4347–4354, 2012.
- [14] C. Parrott, T. J. Dodd, and R. Groß, “HiGen: A high-speed genderless mechanical connection mechanism with single-sided disconnect for self-reconfigurable modular robots,” *IEEE Int. Conf. Intell. Robot. Syst.*, no. Iros, pp. 3926–3932, 2014.
- [15] K. Mitsui, R. Ozawa, and T. Kou, “An under-actuated robotic hand for multiple grasps,” *IEEE Int. Conf. Intell. Robot. Syst.*, pp. 5475–5480, 2013.
- [16] S. H. Collins and A. Ruina, “A bipedal walking robot with efficient and human-like gait,” *Proc. - IEEE Int. Conf. Robot. Autom.*, vol. 2005, no. April, pp. 1983–1988, 2005.



- [17] M. Wisse, G. Feliksadal, J. van Frankenhyyzen, and B. Moyer, "Passive-based walking robot," *IEEE Robot. Autom. Mag.*, vol. 14, no. 2, pp. 52–62, 2007.
- [18] M. Tavakoli, L. Marques, and A. T. De Almeida, "Flexirigid, a novel two phase flexible gripper," *IEEE Int. Conf. Intell. Robot. Syst.*, pp. 5046–5051, 2013.
- [19] R. Unal, S. M. Behrens, R. Carloni, E. E. G. Hekman, S. Stramigioli, and H. F. J. M. Koopman, "Prototype design and realization of an innovative energy efficient transfemoral prosthesis," *2010 3rd IEEE RAS EMBS Int. Conf. Biomed. Robot. Biomechatronics, BioRob 2010*, pp. 191–196, 2010.
- [20] S. H. Collins and A. D. Kuo, "Recycling energy to restore impaired ankle function during human walking," *PLoS One*, vol. 5, no. 2, 2010.
- [21] K. Gilpin and D. Rus, "Modular robot systems," *IEEE Robot. Autom. Mag.*, vol. 17, no. 3, pp. 38–55, 2010.
- [22] A. Yagi , K. Matsumiya , K. Masamune , H. Liao , and T. Dohi , " Rigid-flexible outer sheath model using slider linkage locking mechanism and air pressure for endoscopic surgery ," in *Proc. Medical Image Computing and Computer-Assisted Intervention (MICCAI'06)* , pp. 503 – 510, 2006 .
- [23] M. B. Wiggin, G. S. Sawicki, and S. H. Collins, "An exoskeleton using controlled energy storage and release to aid ankle propulsion," *IEEE Int. Conf. Rehabil. Robot.*, pp. 1–5, 2011.
- [24] B. Brackx, M. Van Damme, A. Matthys, B. Vanderborght, and D. Lefeber, "Passive ankle-foot prosthesis prototype with extended push-off," *Int. J. Adv. Robot. Syst.*, vol. 10, 2013.
- [25] B. Li, Q. Deng, and Z. Liu, "A spherical hopping robot for exploration in complex environments," *2009 IEEE Int. Conf. Robot. Biomimetics, ROBIO 2009*, pp. 402–407, 2009.
- [26] J. Geeroms, L. Flynn, R. Jimenez-Fabian, B. Vanderborght, and D. Lefeber, "Ankle-Knee prosthesis with powered ankle and energy transfer for CYBERLEGS  $\alpha$ -prototype," *IEEE Int. Conf. Rehabil. Robot.*, pp. 1–6, 2013.
- [27] M. Palpacelli, L. Carbonari, and G. Palmieri, "A lockable spherical joint for robotic applications," *MESA 2014 - 10th IEEE/ASME Int. Conf. Mechatron. Embed. Syst. Appl. Conf. Proc.*, pp. 1–6, 2014.
- [28] N. I. Kern, T. J. Majewski, R. J. Triolo, R. Kobetic, and R. D. Quinn, "A locking compliant device inspired by the Anatomy of the spine," *J. Mech. Des. Trans. ASME*, vol. 131, no. 1, pp. 014 501-1–014 501-3, 2009.
- [29] A. Kossett and N. Papanikolopoulos, "A robust miniature robot design for land/air hybrid locomotion," *Proc. - IEEE Int. Conf. Robot. Autom.*, pp. 4595–4600, 2011.
- [30] G. Elliott, G. S. Sawicki, A. Marecki, and H. Herr, "The biomechanics and energetics of human running using an elastic knee exoskeleton," *IEEE Int. Conf. Rehabil. Robot.*, vol. 0, no. 4, pp. 1–6, 2013.
- [31] J. H. Bickford, *Mechanisms for Intermittent Motion*. New York: Industrial Press, 1972.
- [32] G. Mathijssen, D. Lefeber, and B. Vanderborght, "Variable recruitment of parallel elastic elements: Series-parallel elastic actuators (SPEA) with dephased mutilated gears,"

- IEEE/ASME Trans. Mechatronics, vol. 20, no. 2, pp. 594–602, 2015.
- [33] J. Realmuto, G. Klute, and S. Devasia, “Nonlinear passive cam-based springs for powered ankle prostheses,” *J. Med. Devices, Trans. ASME*, vol. 9, no. 1, pp. 1–10, 2015.
- [34] M. Li, W. Cheng, and R. Xie, “Design and Experimental Validation of Two Cam-Based Force Regulation Mechanisms,” *J. Mech. Robot.*, vol. 12, no. 3, pp. 1–14, 2020.
- [35] H. A. Mauch, “Stance control for above-knee artificial legs—design considerations in the S-N-S knee,” *Bull. Prosthet. Res.*, vol. 10, no. 10, pp. 61–72, 1968.
- [36] C. Semini et al., “Design of the Hydraulically Actuated, Torque-Controlled Quadruped Robot HyQ2Max,” *IEEE/ASME Trans. Mechatronics*, vol. 22, no. 2, pp. 635–646, 2017.
- [37] S. H. Hyon, T. Yoneda, and D. Suewaka, “Lightweight hydraulic leg to explore agile legged locomotion,” *IEEE Int. Conf. Intell. Robot. Syst.*, pp. 4655–4660, 2013.
- [38] C. K. Huang and M. C. Shih, “Design of a hydraulic anti-lock braking system (ABS) for a motorcycle,” *J. Mech. Sci. Technol.*, vol. 24, no. 5, pp. 1141–1149, 2010.
- [39] T. Morita and S. Sugano, “Development of one-D.O.F. robot arm equipped with mechanical impedance adjuster,” *IEEE Int. Conf. Intell. Robot. Syst.*, vol. 1, pp. 407–412, 1995.
- [40] G. Hirzinger, A. Albu-Schäffer, M. Hähle, I. Schaefer, and N. Sporer, “On a new generation of torque controlled light-weight robots,” *Proc. - IEEE Int. Conf. Robot. Autom.*, vol. 4, pp. 3356–3363, 2001.
- [41] Y. Sugahara, T. Endo, H. O. Lim, and A. Takanishi, “Design of a battery-powered multi-purpose bipedal locomotor with parallel mechanism,” *IEEE Int. Conf. Intell. Robot. Syst.*, vol. 3, no. October, pp. 2658–2663, 2002.
- [42] E. J. Rouse, L. M. Mooney, and H. M. Herr, “Clutchable series-elastic actuator: Implications for prosthetic knee design,” *Int. J. Rob. Res.*, vol. 33, no. 13, pp. 1611–1625, 2014.
- [43] K. Yamatoh, M. Ogura, K. Kanbe, and Y. Isogai, “Piezoelectric brake device,” U.S. Patent 4 854 424, Aug. 8, 1989.
- [44] G. Hirzinger et al., “Advances in Robotics: The DLR Experience,” *Int. J. Rob. Res.*, vol. 18, no. 11, pp. 1064–1087, 1999.
- [45] S. Munir, L. Tognetti, and W. J. Book, “Experimental evaluation of a new braking system for use in passive haptic displays,” *Proc. Am. Control Conf.*, vol. 6, pp. 4456–4460, 1999.
- [46] M. Laffranchi, N. G. Tsagarakis, and D. G. Caldwell, “A variable physical damping actuator (VPDA) for compliant robotic joints,” *Proc. - IEEE Int. Conf. Robot. Autom.*, pp. 1668–1674, 2010.
- [47] B. Kang, R. Kojcev, and E. Sinibaldi, “The first interlaced continuum robot, devised to intrinsically follow the leader,” *PLoS One*, vol. 11, no. 2, pp. 1–16, 2016.
- [48] M. Plooij, T. Van Der Hoeven, G. Dunning, and M. Wisse, “Statically balanced brakes,” *Precis. Eng.*, vol. 43, pp. 468–478, 2016.
- [49] Q. Li, V. Naing, J. A. Hoffer, D. J. Weber, A. D. Kuo, and J. M. Donelan, “Biomechanical energy harvesting: Apparatus and method,” *Proc. - IEEE Int. Conf. Robot. Autom.*, vol. 48109, pp. 3672–3677, 2008.

- [50] T. Siedel, D. Lukac, T. Geppert, C. Benckendorff, and M. Hild, "Operating characteristics of a passive, bidirectional overrunning clutch for rotary joints of robots," 2011 23rd Int. Symp. Information, Commun. Autom. Technol. ICAT 2011, pp. 1–7, 2011.
- [51] N. G. Tsagarakis, S. Morfey, H. Dallali, G. A. Medrano-Cerda, and D. G. Caldwell, "An asymmetric compliant antagonistic joint design for high performance mobility," IEEE Int. Conf. Intell. Robot. Syst., pp. 5512–5517, 2013.
- [52] M. Controzzi, C. Cipriani, and M. C. Carrozza, "Miniaturized non-back-drivable mechanism for robotic applications," Mech. Mach. Theory, vol. 45, no. 10, pp. 1395–1406, 2010.
- [53] H. Zhao, B. Wang, G. Zhang, and J. Li, "Concept of a new overrunning clutch with the characteristic of reverse force transfer at high speed," Eng. Reports, vol. 3, no. 11, pp. 1–13, 2021.
- [54] J. Baca, S. G. M. Hossain, P. Dasgupta, C. A. Nelson, and A. Dutta, "ModRED: Hardware design and reconfiguration planning for a high dexterity modular self-reconfigurable robot for extra-terrestrial exploration," Rob. Auton. Syst., vol. 62, no. 7, pp. 1002–1015, 2014.
- [55] I. Vanderniepen, R. Van Ham, M. Van Damme, and D. Lefeber, "Design of a powered elbow orthosis for orthopaedic rehabilitation using compliant actuation," Proc. IEEE RAS EMBS Int. Conf. Biomed. Robot. Biomechatronics, pp. 801–806, 2008.
- [56] H. Gu, M. Ceccarelli, and G. Carbone, "An experimental characterization of a 1-DOF anthropomorphic arm for humanoid robots," Proc. 13th World Sci. Eng. Acad. Soc. Int. Conf. Comput., pp. 92–99, 2009.
- [57] S. Morita, Toshio and Sugano, "Design and development of a new robot joint using a mechanical impedance adjuster," Proc. IEEE Int. Conf. Robot. Autom., vol. 3, pp. 2469–2475, 1995.
- [58] K. Goris, J. Saldien, B. Vanderborcht, and D. Lefeber, "How to achieve the huggable behavior of the social robot Probo? A reflection on the actuators," Mechatronics, vol. 21, no. 3, pp. 490–500, 2011.
- [59] P. Cherelle et al., "The MACCEPA actuation system as torque actuator in the gait rehabilitation robot ALTACRO," Proc. IEEE RAS EMBS Int. Conf. Biomed. Robot. Biomechatronics, pp. 27–32, 2010.
- [60] B. Peerdeman, S. Stramigioli, E. E. G. Hekman, D. M. Brouwer, and S. Misra, "Development of Underactuated Prosthetic Fingers with Joint Locking and Electromyographic Control," Mech. Eng. Res., vol. 3, no. 1, p. 130, 2013.
- [61] J. Kim and S. B. Choi, "Design and modeling of a clutch actuator system with self-energizing mechanism," IEEE/ASME Trans. Mechatronics, vol. 16, no. 5, pp. 953–966, 2011.
- [62] J. Werkmeister and A. Slocum, "Theoretical and experimental determination of capstan drive stiffness," Precis. Eng., vol. 31, no. 1, pp. 55–67, 2007.
- [63] O. Baser and E. Ilhan Konukseven, "Theoretical and experimental determination of capstan drive slip error," Mech. Mach. Theory, vol. 45, no. 6, pp. 815–827, 2010.
- [64] M. Quigley, A. Asbeck, and A. Ng, "A low-cost compliant 7-DOF robotic manipulator," Proc.

- IEEE Int. Conf. Robot. Autom., pp. 6051–6058, 2011.
- [65] D. F. B. Haeufle, M. D. Taylor, S. Schmitt, and H. Geyer, “A clutched parallel elastic actuator concept: Towards energy efficient powered legs in prosthetics and robotics,” *Proc. IEEE RAS EMBS Int. Conf. Biomed. Robot. Biomechatronics*, pp. 1614–1619, 2012.
- [66] A. Sledd and M. K. O’Malley, “Performance enhancement of a haptic arm exoskeleton,” *Proc. Symp. Haptic Interfaces Virtual Environ. Teleoperator Syst.*, pp. 375–381, 2006.
- [67] G. Stellin et al., “Preliminary design of an anthropomorphic dexterous hand for a 2-years-old humanoid: Towards cognition,” *Proc. IEEE/RAS-EMBS Int. Conf. Biomed. Robot. Biomechatronics*, pp. 290–295, 2006.
- [68] V. Wall, R. Deimel and O. Brock, "Selective stiffening of soft actuators based on jamming," 2015 IEEE International Conference on Robotics and Automation (ICRA), Seattle, WA, USA, pp. 252-257, 2015.
- [69] N. G. Cheng et al., “Design and analysis of a robust, low-cost, highly articulated manipulator enabled by jamming of granular media,” *Proc. - IEEE Int. Conf. Robot. Autom.*, pp. 4328–4333, 2012.
- [70] Y. Wei, Y. Chen, Y. Yang, and Y. Li, “A soft robotic spine with tunable stiffness based on integrated ball joint and particle jamming,” *Mechatronics*, vol. 33, pp. 84–92, 2016.
- [71] P. Jiang, Y. Yang, M. Z. Q. Chen, and Y. Chen, “A variable stiffness gripper based on differential drive particle jamming,” *Bioinspiration and Biomimetics*, vol. 14, no. 3, pp. 0–15, 2019.
- [72] M. Fujita et al., “Jamming layered membrane gripper mechanism for grasping differently shaped-objects without excessive pushing force for search and rescue missions,” *Adv. Robot.*, vol. 32, no. 11, pp. 590–604, 2018.
- [73] M. Ibrahimi, L. Paternò, L. Ricotti, and A. Menciassi, “A Layer Jamming Actuator for Tunable Stiffness and Shape-Changing Devices,” *Soft Robot.*, vol. 00, no. 00, pp. 1–12, 2020.
- [74] D. C. F. Li, Z. Wang, B. Ouyang, and Y. H. Liu, “A reconfigurable variable stiffness manipulator by a sliding layer mechanism,” *Proc. - IEEE Int. Conf. Robot. Autom.*, vol. 2019-May, pp. 3976–3982, 2019.
- [75] T. Wang, S. Member, J. Zhang, Y. Li, J. Hong, and M. Y. Wang, “Electrostatic Layer Jamming Variable Stiffness for Soft Robotics,” *IEEE/ASME Trans. Mechatronics*, vol. 24, no. 2, pp. 424–433, 2019.
- [76] Y. S. Narang, J. J. Vlassak, and R. D. Howe, “Mechanically Versatile Soft Machines through Laminar Jamming,” *Adv. Funct. Mater.*, vol. 28, no. 17, pp. 1–9, 2018.
- [77] Y. Gao, X. Huang, I. S. Mann, and H. J. Su, “A Novel Variable Stiffness Compliant Robotic Gripper Based on Layer Jamming,” *J. Mech. Robot.*, vol. 12, no. 5, pp. 1–8, 2020.
- [78] Y. J. Kim, S. Cheng, S. Kim, and K. Iagnemma, “A novel layer jamming mechanism with tunable stiffness capability for minimally invasive surgery,” *IEEE Trans. Robot.*, vol. 29, no. 4, pp. 1031–1042, 2013.
- [79] R. Mukaide et al., “Radial-Layer Jamming Mechanism for String Configuration,” *IEEE Robot.*

- Autom. Lett., vol. 5, no. 4, pp. 5221–5228, 2020.
- [80] Chen, J. H. Chang, A. S. Greenlee, K. C. Cheung, A. H. Slocum, and R. Gupta, “Multi-turn, tension-stiffening catheter navigation system,” in *IEEE International Conference on Robotics and Automation*, pp. 5570–5575, 2010.
- [81] K. Tadakuma et al., “Fire-Resistant Deformable Soft Gripper Based on Wire Jamming Mechanism,” *2020 3rd IEEE International Conference on Soft Robotics (RoboSoft)*, New Haven, CT, USA, pp. 740–747, 2020.
- [82] R. Michikawa, T. Endo, and F. Matsuno, “A Multi-DoF Exoskeleton Haptic Device for the Grasping of a Compliant Object Adapting to a User’s Motion Using Jamming Transitions,” *IEEE Trans. Robot.*, vol. 39, no. 1, pp. 373–385, 2023.
- [83] Degani, H. Choset, B. Zubiate, T. Ota, and M. Zenati, “Highly articulated robotic probe for minimally invasive surgery,” in *In Proceedings of the 2006 IEEE International Conference on Robotics and Automation*, pp. 3273–3276, 2008.
- [84] Y. Jiang, D. Chen, C. Liu, and J. Li, “Chain-Like Granular Jamming: A Novel Stiffness-Programmable Mechanism for Soft Robotics,” *Soft Robot.*, vol. 6, no. 1, pp. 118–132, 2019.
- [85] Y. J. Kim, S. Cheng, S. Kim, and K. Iagnemma, “A stiffness-adjustable hyper-redundant manipulator using a variable neutral-line mechanism for minimally invasive surgery,” *IEEE Trans. Robot.*, vol. 30, no. 2, pp. 382–395, 2014.
- [86] Y. Nakata, “Tool Holding Articulated Arm”, U.S. Patent 20160151920, June. 2, 2016.
- [87] Canberk Sozer, L. Paternò, G. Tortora, and A. Menciasci, “A Novel Pressure-Controlled Revolute Joint with Variable Stiffness,” *Soft Robotics*, 2021.
- [88] H. Wang, Z. Chen, and S. Zuo, “Flexible Manipulator with Low-Melting-Point Alloy Actuation and Variable Stiffness,” *Soft Robot.*, vol. 9, no. 3, pp. 577–590, 2022.
- [89] W. Shan, T. Lu, and C. Majidi, “Soft-matter composites with electrically tunable elastic rigidity,” *Smart Mater. Struct.*, vol. 22, no. 8, 2013.
- [90] J. Shintake, B. Schubert, S. Rosset, H. Shea, and D. Floreano, “Variable stiffness actuator for soft robotics using dielectric elastomer and low-melting-point alloy,” in *IEEE International Conference on Intelligent Robots and Systems*, pp. 1097–1102, 2015.
- [91] R. Zhao, Y. Yao, and Y. Luo, “Development of a variable stiffness over tube based on low-melting-point-alloy for endoscopic surgery,” *J. Med. Devices, Trans. ASME*, vol. 10, no. 2, pp. 1–8, 2016.
- [92] H. Nakai, Y. Hoshino, M. Inaba, and H. Inoue, “Softening Deformable Robot: Development of Shape Adaptive Robot using Phase Change of Low-melting-point Alloy,” *J. Robot. Soc. Japan*, vol. 20, no. 6, pp. 69–74, 2002.
- [93] A. J. Loeve, J. H. Bosma, P. Breedveld, D. Dodou, and J. Dankelman, “Polymer rigidity control for endoscopic shaft-guide ‘Plastolock’ - A feasibility study,” *J. Med. Devices, Trans. ASME*, vol. 4, no. 4, pp. 1–6, 2010.
- [94] M. McEvoy and N. Correll, “Shape change through programmable stiffness,” *Springer Tracts Adv. Robot.*, vol. 109, pp. 893–907, 2016.

- [95] M. A. McEvoy and N. Correll, “Thermoplastic variable stiffness composites with embedded, networked sensing, actuation, and control,” *J. Compos. Mater.*, vol. 49, no. 15, pp. 1799–1808, 2015.
- [96] A. Balasubramanian, M. Standish, and C. J. Bettinger, “Microfluidic thermally activated materials for rapid control of macroscopic compliance,” *Adv. Funct. Mater.*, vol. 24, no. 30, pp. 4860–4866, 2014.
- [97] W. Shan, S. Diller, A. Tutcuoglu, and C. Majidi, “Rigidity-tuning conductive elastomer,” *Smart Mater. Struct.*, vol. 24, no. 6, 2015.
- [98] K. Ikuta, M. Tsukamoto, and S. Hirose, “Shape memory alloy servo actuator system with electric resistance feedback and application for active endoscope,” in *Proc. IEEE Int. Conf. Robotics and Automation*, Philadelphia, PA, 1988, pp. 427–430.
- [99] J. P. Swensen and A. M. Dollar, “Optimization of parallel spring antagonists for Nitinol shape memory alloy actuators,” *Proc. - IEEE Int. Conf. Robot. Autom.*, pp. 6345–6349, 2014.
- [100] Y. Haga, M. Mizushima, T. Matsunaga, K. Totsu, and M. Esashi, “Active bending ileus tube using shape memory alloy for treatment of intestinal obstruction,” *3rd Annu. Int. IEEE/EMBS Spec. Top. Conf. Microtechnology Med. Biol.*, pp. 249–252, 2005.
- [101] M. Ho and J. P. Desai, “Characterization of SMA actuator for applications in robotic neurosurgery,” *31st Annu. Int. Conf. IEEE EMBS*, pp. 6856–6859, 2009.
- [102] A. Arora, Y. Ambe, T. H. Kim, R. Ariizumi, and F. Matsuno, “Development of a maneuverable flexible manipulator for minimally invasive surgery with varied stiffness,” *Artif. Life Robot.*, vol. 19, no. 4, pp. 340–346, 2014.
- [103] A. Lendlein and R. Langer, “Biodegradable, elastic shape-memory polymers for potential biomedical applications,” *Science (80- )*, vol. 296, no. 5573, pp. 1673–1676, 2002.
- [104] A. Firouzeh, S. S. Mirrazavi Salehian, A. Billard, and J. Paik, “An under actuated robotic arm with adjustable stiffness shape memory polymer joints,” *IEEE Int. Conf. Robot. Autom.*, pp. 2536–2543, 2015.
- [105] D. Ratna and J. Karger-Kocsis, “Recent advances in shape memory polymers and composites: A review,” *J. Mater. Sci.*, vol. 43, no. 1, pp. 254–269, 2008.
- [106] S. Griffin, “Selectively flexible catheter and method of use,” *WO Patent 2006/060312*, June 8, 2006.
- [107] C. Majidi and R. J. Wood, “Tunable elastic stiffness with microconfined magnetorheological domains at low magnetic field,” *Appl. Phys. Lett.*, vol. 97, no. 16, pp. 2010–2012, 2010.
- [108] H. Ma, B. Chen, L. Qin, and W. Liao, “Design and testing of a regenerative magnetorheological actuator for assistive knee braces,” *Smart Mater. Struct.*, vol. 26, no. 3, pp. 1–13, 2017.
- [109] G. Park, M. T. Bement, D. A. Hartman, R. E. Smith, and C. R. Farrar, “The use of active materials for machining processes: A review,” *Int. J. Mach. Tools Manuf.*, vol. 47, no. 15, pp. 2189–2206, 2007.
- [110] A. Sadeghi, L. Beccai, and B. Mazzolai, “Innovative soft robots based on electro-rheological fluids,” *IEEE Int. Conf. Intell. Robot. Syst.*, pp. 4237–4242, 2012.

- [111] G. Olson, "Medical devices with variable stiffness," WO Patent 2007/015981, Feb. 8, 2007.
- [112] T. Takahashi, M. Watanabe, K. Tadakuma, E. Takane, M. Konyo, and S. Tadokoro, "Two-Sheet Type Rotary-Driven Thin Bending Mechanism Realizing High Stiffness," *IEEE Robot. Autom. Lett.*, vol. 6, no. 4, pp. 8333–8340, 2021.
- [113] F. Corucci, N. Cheney, F. Giorgio-Serchi, J. Bongard, and C. Laschi, "Evolving soft locomotion in aquatic and terrestrial environments: Effects of material properties and environmental transitions," *Soft Robot.*, vol. 5, no. 4, pp. 475–493, 2018.
- [114] M. Mizutani, Y. Shimodate, and K. Ito, "Semicircular duplex manipulator to search narrow spaces for victims," in *Proc. IEEE International Conference on Safety, Security, and Rescue Robotics*, 2011, pp. 7–12.
- [115] T. Miller-Jackson, Y. Sun, R. Natividad, and C. H. Yeow, "Tubular jamming: A variable stiffening method toward high-force applications with soft robotic components," *Soft Robot.*, vol. 6, no. 4, pp. 468–482, 2019.
- [116] C. Bishop, M. Russo, X. Dong, and D. Axinte, "A Novel Underactuated Continuum Robot With Shape Memory Alloy Clutches," *IEEE/ASME Trans. Mechatronics*, vol. 27, no. 6, pp. 5339–5350, 2022.
- [117] M. Watanabe et al., "Toroidal Origami Monotrack: Mechanism to Realize Smooth Driving and Bending for Closed-Skin-Drive Robots," *IEEE Int. Conf. Intell. Robot. Syst.*, vol. 2022-October, pp. 480–487, 2022.
- [118] C. P. Chou and B. Hannaford, "Measurement and modeling of McKibben pneumatic artificial muscles," *IEEE Trans. Robot. Autom.*, vol. 12, no. 1, pp. 90–102, Feb. 1996.
- [119] C. Xiang, M. E. Giannaccini, T. Theodoridis, L. Hao, S. Nefti-Meziani, and S. Davis, "Variable stiffness McKibben muscles with hydraulic and pneumatic operating modes," *Adv. Robot.*, vol. 30, no. 13, pp. 889–899, Jul. 2016.
- [120] N. Napp, B. Araki, M. T. Tolley, R. Nagpal, and R. J. Wood, "Simple passive valves for addressable pneumatic actuation," *Proc. - IEEE Int. Conf. Robot. Autom.*, pp. 1440–1445, 2014.
- [121] N. Vasios, A. J. Gross, S. Soifer, J. T. B. Overvelde, and K. Bertoldi, "Harnessing Viscous Flow to Simplify the Actuation of Fluidic Soft Robots," *Soft Robot.*, vol. 7, no. 1, pp. 1–9, 2020.
- [122] S. Tadokoro, "Mission and Overview of DDT Project," *Journal of Robotics Society of Japan*, Vol. 22, No.5, pp. 544–545, 2004.
- [123] S. Hirose and M. Mori, "Biologically Inspired Snake-like Robots," *IEEE International Conference on Robotics and Biomimetics*, Shenyang, China, August 2004.
- [124] A. Crespi, A. Badertscher, A. Guignard and A. J. Ijspeert, "AmphiBot I: An amphibious snake-like robot", *Robot. Auton. Syst.*, vol. 50-4, pp. 163-175, 2005.
- [125] T. Takayama and S. Hirose, "Development of Souryu-I connected crawler vehicle for inspection of narrow and winding space." 2000 26th Annual Conference of the IEEE Industrial Electronics Society. IECON 2000. 2000 IEEE International Conference on Industrial Electronics, Control and Instrumentation. 21st Century Technologies 1, Nagoya, Japan, October 2000.

- [126] T. Kamegawa, T. Yamasaki, H. Igarashi and F. Matsuno, "Development of The Snake-like Rescue Robot "KOHGA"", Proceedings of the 2004 IEEE International conference on Robotics and Automation, pp. 5081-5086, 2004.
- [127] C. Wright, A. Johnson, A. Peck, Z. McCord, A. Naaktgeboren, P. Gi-anfortoni, M. Gonzalez-Rivero, R. Hatton, and H. Choset, "Design of a modular snake robot," in Intelligent Robots and Systems, IEEE/RSJ International Conference on, pp. 2609–2614, 2007.
- [128] C. Wright, A. Buchan, B. Brown, J. Geist, M. Schwerin, D. Rollinson, M. Tesch, and H. Choset, "Design and Architecture of the Unified Modular Snake Robot," in IEEE International Conference on Robotics and Automation (ICRA), (St. Paul, USA), pp. 4347–4354, 2012.
- [129] K. Hatazaki, M. Konyo, K. Isaki, S. Tadokoro, F. Takemura, "Active Scope Camera for Urban Search and Rescue", IEEE/RSJ International Conference on Intelligent Robots and Systems San Diego, CA, USA, Oct 29 - Nov 2, 2007.
- [130] C. Sophocleous et al., "Development and initial testing of a prototype concentric tube robot for surgical interventions", in IEEE 12th Int. Conf. on BIBE, pp.227-232,2012.
- [131] Y. Chen, J. H. Chang, A. S. Greenlee, K. C. Cheung, A. H. Slocum, and R. Gupta, "Multi-turn, tension-stiffening catheter navigation system," Proc. - IEEE Int. Conf. Robot. Autom., pp. 5570–5575, 2010.
- [132] Shuichi WAKIMOTO, "Development and Application of Thin McKibben Artificial Muscles", Journal of The Society of Instrument and Control Engineers, Vol. 57, No. 11, pp. 8-19.
- [133] S. Zuo et al., "Nonmetallic rigid-flexible outer sheath with pneumatic shape locking mechanism and double curvature structure," Lect. Notes Comput. Sci. (including Subser. Lect. Notes Artif. Intell. Lect. Notes Bioinformatics), vol. 6891 LNCS, no. PART 1, pp. 169–177, 2011.
- [134] S. Zuo, K. Iijima, T. Tokumiya, and K. Masamune, "Variable stiffness outer sheath with 'Dragon skin' structure and negative pneumatic shape-locking mechanism," Int. J. Comput. Assist. Radiol. Surg., vol. 9, no. 5, pp. 857–865, 2014.
- [135] T. Wang, S. Member, J. Zhang, Y. Li, J. Hong, and M. Y. Wang, "Electrostatic Layer Jamming Variable Stiffness for Soft Robotics," IEEE/ASME Trans. Mechatronics, vol. 24, no. 2, pp. 424–433, 2019.
- [136] C. Sozer, S. K. Sahu, L. Paterno, and A. Menciassi, "Robotic Modules for a Continuum Manipulator With Variable Stiffness Joints," IEEE Robot. Autom. Lett., vol. 8, no. 8, pp. 4745–4752, 2023.
- [137] B. E. Schubert and D. Floreano, "Variable stiffness material based on rigid low-melting-point-alloy microstructures embedded in soft poly(dimethylsiloxane) (PDMS)," RSC Adv., vol. 3, no. 46, pp. 24671–24679, 2013.
- [138] T. P. Chenal, J. C. Case, J. Paik, and R. K. Kramer, "Variable stiffness fabrics with embedded shape memory materials for wearable applications," IEEE Int. Conf. Intell. Robot. Syst., no. Iros, pp. 2827–2831, 2014.
- [139] F. Gandhi and S. G. Kang, "Beams with controllable flexural stiffness," Smart Mater. Struct., vol. 16, no. 4, pp. 1179–1184, 2007.



- [140] Bo Liu, S. A. Boggs and M. T. Shaw, "Electrorheological properties of anisotropically filled elastomers," in IEEE Transactions on Dielectrics and Electrical Insulation, vol. 8, no. 2, pp. 173-181, April 2001.
- [141] C. Cao and X. Zhao, "Tunable stiffness of electrorheological elastomers by designing mesostructures," Appl. Phys. Lett., vol. 103, no. 4, 2013.
- [142] J. Ou, L. Yao, D. Tauber, J. Steimle, R. Niiyama, and H. Ishii, "JamSheets: Thin interfaces with tunable stiffness enabled by layer jamming," TEI 2014 - 8th Int. Conf. Tangible, Embed. Embodied Interact. Proc., pp. 65-72, 2014.

# RESEARCH ACHIEVEMENTS

## I. Peer-reviewed journals: 3 main-authored

- 1) Issei Onda, Kenjiro Tadakuma, Masahiro Watanabe, Kazuki Abe, Tetsuyou Watanabe, Masashi Konyo, and Satoshi Tadokoro, "Highly Articulated Tube Mechanism with Variable Stiffness and Shape Restoration Using a Pneumatic Actuator", IEEE Robotics and Automation Letter, vol. 7, no. 2, pp. 3664-3671, Apr. 2022. DOI: 10.1109/LRA.2022.3147246.
- 2) Issei Onda, Masahiro Watanabe, Kenjiro Tadakuma, Kazuki Abe and Satoshi Tadokoro, "Tube Mechanism With 3-Axis Rotary Joints Structure to Achieve Variable Stiffness Using Positive Pressure," in IEEE Robotics and Automation Letters, vol. 9, no. 1, pp. 675-682, Jan. 2024, doi: 10.1109/LRA.2023.3234767
- 3) Issei Onda, Masahiro Watanabe, Kenjiro Tadakuma, Kazuki Abe, and Satoshi Tadokoro, "Tube Mechanism to Achieve Positive-Pressurization Variable Stiffness by Lever and Wire," in IEEE Robotics and Automation Letters (Under Review).

## II. Peer-reviewed international conferences: 4 main-authored

- 1) Issei Onda, Masahiro Watanabe, Kenjiro Tadakuma, Eri Takane, Masashi Konyo, and Satoshi Tadokoro, "Pneumatic Driven Hollow Variable Stiffness Mechanism Aiming Non-Contact Insertion of Telescopic Guide Tubes," 2021 IEEE 4th International Conference on Soft Robotics (RoboSoft), Fri50.1, pp. 615-621, Apr. 2021.
- 2) Issei Onda, Kenjiro Tadakuma, Masahiro Watanabe, Kazuki Abe, Tetsuyou Watanabe, Masashi Konyo, and Satoshi Tadokoro, "Highly Articulated Tube Mechanism with Variable Stiffness and Shape Restoration Using a Pneumatic Actuator", 2022 IEEE 5th International Conference on Soft Robotics (RoboSoft), vol. 7, no. 2, pp. 3664-3671, Edinburgh, Apr. 2022.
- 3) Issei Onda, Shoya Shimizu, Kenjiro Tadakuma, Watanabe Masahiro, Kazuki Abe, and Satoshi Tadokoro, "Worm-inspired robot with variable stiffness mechanism including fluidic bellows", The 11th International Symposium on Adaptive Motion of Animals and Machines, Kobe, June.2023
- 4) Issei Onda, Masahiro Watanabe, Kenjiro Tadakuma, Kazuki Abe, and Satoshi Tadokoro, "Tube Mechanism with 3-axis Rotary Joints Structure to Achieve Variable Stiffness Using Positive Pressure," 2023 IEEE/RSJ International Conference on Intelligent Robots and Systems (IROS), 2023.

## III. Awards: 3

- 1) Robosoft2022 Best Poster Award, Issei Onda, Kenjiro Tadakuma, Masahiro Watanabe, Kazuki Abe, Tetsuyou Watanabe, Masashi Konyo, and Satoshi Tadokoro, "Highly Articulated Tube Mechanism with Variable Stiffness and Shape Restoration Using a Pneumatic Actuator", IEEE Robotics and Automation Society, April 8, 2022.
- 2) 東北大学 大学院情報科学研究科 博士後期課程学生発表会 ベストプレゼンテーション賞.
- 3) 研究奨励賞, 恩田一生, "加圧により柔剛切替を可能とする多関節線状メカニズムの原理考案・実機具現化", 日本ロボット学会, 2023.

## IV. Patents: 1 main-authored, 3 co-authored

- 1) 渡辺将広, 恩田一生, 多田隈建二郎, 昆陽雅司, 田所諭, "剛性可変連結体", 特願 2020-066431, 出願日: 2020年4月2日.
- 2) 渡辺将広, 恩田一生, 高橋知也, 多田隈建二郎, "剛性可変変形体および剛性可変機構", 特願 2021-020338, 出願日: 2021年2月12日.
- 3) 恩田一生, 多田隈建二郎, 渡辺将広, 阿部一樹, 昆陽雅司, 田所諭, "剛性可変連結体", 特願 2022-077213, 出願日: 2022年5月9日.
- 4) 渡辺将広, 恩田一生, 佐野峻輔, 多田隈建二郎, 田所諭, "剛性可変索状体", 特願 2023-95994, 出願日: 2023年6月12日.

## V. Scholarships: 4

- 1) 恩田一生, 博士後期課程学生特別支援制度, 東北大学 大学院情報科学研究科, 2021年4月~2021年6月.
- 2) 恩田一生, 学際高等研究教育院, 東北大学高等大学院機構, 2021年4月~2022年3月.
- 3) 恩田一生, 一般財団法人青葉工学振興会奨学金, 一般財団法人青葉工学振興会, 2021年6月~

2022年4月.

- 4) 恩田一生, 2022年度 特別研究員-DC2, 日本学術振興会, 2022年4月~2024年3月.

## VI. Domestic conferences: 7 main-authored, 9 co-authored

- 1) 恩田一生, 小澤悠, 高橋知也, 清水杜織, 渡辺将広, 多田隈建二郎, 昆陽雅司, 田所諭, "膜破損時にも柔剛切替機能を維持可能な被覆式ジャミング機構", 第37回日本ロボット学会学術講演会, 1D1-04, 東京, 2019年9月3-7日.
- 2) 恩田一生, 小澤悠, 渡辺将広, 高根英里, 多田隈建二郎, 昆陽雅司, 田所諭, "加圧により高剛性化するジャミング転移機構 —流体駆動式柔剛切替メカニズムの考案と具現化—", 日本機械学会ロボティクス・メカトロニクス講演会 2020, 1P2-H10, 金沢(オンライン開催), 2020年5月27日-29日.
- 3) 恩田一生, 小澤悠, 高橋知也, 渡辺将広, 多田隈建二郎, 昆陽雅司, 田所諭, "膜破損時にも柔剛切替機能を維持可能な被覆式ジャミンググリッパ機構 —基本保持特性の評価—", 日本機械学会ロボティクス・メカトロニクス講演会 2020, 2A2-I07, 金沢(オンライン開催), 2020年5月27日-29日.
- 4) 恩田一生, 渡辺将広, 高根英里, 多田隈建二郎, 昆陽雅司, 田所諭, "径方向多段構造を有する加圧式1次元ジャミング転移機構", 第38回日本ロボット学会学術講演会, 3J2-02, 2020年10月9-11日.
- 5) 金田侑, 恩田一生, 渡辺将広, 西谷誠治, 戸島亮, 高根英里, 多田隈建二郎, 昆陽雅司, 田所諭, "膜破損時の内容物飛散防止・漏出抑制を可能とする柔剛切替グリッパ機構", 第38回日本ロボット学会学術講演会, 1G3-02, 2020年10月9-11日.
- 6) 釧持優人, 恩田一生, 高根英里, 渡辺将広, 金田侑, 西谷誠治, 戸島亮, 多田隈建二郎, 昆陽雅司, 田所諭, "磁性ピンアレイ・膜袋複合グリッパ機構 —柔軟膜内全域への磁気伝搬を可能とする把持メカニズム—", 第21回計測自動制御学会システムインテグレーション部門講演会, 2E2-10, pp. 1822-1826, 福岡(オンライン開催), 2020年12月16-18日.
- 7) 恩田一生, 釧持優人, 高橋景虎, 吉本悠人, 佐竹陽一, 渡辺将広, 多田隈建二郎, 昆陽雅司, 田所諭, "流体素子内包型柔剛切替メカニズム ~封入人工筋の収縮力と復元力による駆動効果~", 計測自動制御学会東北支部研究集会第332回, 332-2, 2021年5月26日(水).
- 8) 高橋景虎, 釧持優人, 恩田一生, 阿部一樹, 渡辺将広, 多田隈建二郎, 昆陽雅司, 田所諭, "可変長柔剛切替機構", 第39回日本ロボット学会学術講演会, 2B3-03, 2021年9月8日-11日.
- 9) 恩田一生, 釧持優人, 高橋景虎, 渡辺将広, 阿部一樹, 渡辺哲陽, 多田隈建二郎, 昆陽雅司, 田所諭, "流体素子内包型可変特性線状メカニズム —封入ベローズの伸縮変形による駆動効果—", 日本機械学会ロボティクス・メカトロニクス講演会 2022, 2P1-A08, 札幌, 2022年6月1日-4日.
- 10) 清水翔也, 佐野峻輔, 釧持優人, 恩田一生, 高橋知也, 阿部一樹, 渡辺将広, 多田隈理一郎, 多田隈建二郎, 昆陽雅司, 田所諭, "反射型駆動ハンド機構", 第40回日本ロボット学会学術講演会, 4K3-10, 2022年9月5日-9日.
- 11) 高橋景虎, 恩田一生, 阿部一樹, 渡辺将広, 多田隈建二郎, 昆陽雅司, 田所諭, "伸縮・揺動の2軸の柔剛切替が可能な線状メカニズム", 日本機械学会ロボティクス・メカトロニクス講演会 2023, 1A1-F15, 名古屋, 2023年6月28日-7月1日.
- 12) 清水翔也, 恩田一生, 佐野峻輔, 阿部一樹, 渡辺将広, 多田隈理一郎, 多田隈建二郎, 昆陽雅司, 田所諭, "反射型柔剛切替メカニズム —接触回数カウント受容体を身体表面露出させた特性可変機構—", 日本機械学会ロボティクス・メカトロニクス講演会 2023, 1A1-H26, 名古屋, 2023年6月28日-7月1日.
- 13) 渡辺将広, 恩田一生, 佐野峻輔, 多田隈建二郎, 田所諭, "細索状体の形状を強固に保持可能なワイヤ結束機構", 日本機械学会ロボティクス・メカトロニクス講演会 2023, 1A2-F16, 名古屋, 2023年6月28日-7月1日.
- 14) 恩田一生, 渡辺将広, 多田隈建二郎, 阿部一樹, 田所諭, "加圧により柔剛切替を可能とする多関節線状メカニズム —径方向膨張型加圧式1次元ジャミング機構における保持性能の評価—", 日本機械学会ロボティクス・メカトロニクス講演会 2023, 1P1-I21, 名古屋, 2023年6月28日-7月1日.
- 15) 栢分峻汰郎, 清水翔也, 恩田一生, 佐野峻輔, 阿部一樹, 渡辺将広, Josephine Galipon, 多田隈理一郎, 多田隈建二郎, 昆陽雅司, 田所諭, "反射型形状変化メカニズム —接触回数カウント受容体を身体表面露出させた形状可変機構—", 第41回日本ロボット学会学術講演会, 1C2-04, 2023年9月11日-14日.
- 16) 三井田陽和, 恩田一生, 渡辺将広, 阿部一樹, 多田隈建二郎, 昆陽雅司, 田所諭, "皿状ビーズを用いた柔剛切替線状機構 —高分解能と能動湾曲を可能とするビーズの実機具現化と保持トルク特性評価—", 第24回計測自動制御学会システムインテグレーション部門講演会, 1E5-11,

新潟，2023年12月14-16日。

## 論 文 目 録

氏 名	恩田 一生		
博士論文 Articulated Tube Mechanism to Enable Variable Stiffness by Positive-Pressurization (-加圧により柔剛切替を可能とする多関節線状メカニズムに関する研究-) <span style="float: right;">( 1 冊)</span>			
題 名	公表の方法	公表年月日	
Tube Mechanism With 3-Axis Rotary Joints Structure to Achieve Variable Stiffness Using Positive Pressure (加圧を用いて柔剛切替を実現する 3 軸回転ジョイント構造を有するチューブ機構) (Chapter I, Chapter II)	in IEEE Robotics and Automation Letters, vol. 9, no. 1, pp. 675-682, Jan. 2024.	2023 年 12 月 6 日	
Tube Mechanism to Achieve Positive-Pressurization Variable Stiffness by Lever and Wire (レバーとワイヤにより加圧式柔剛切替を達成するチューブ機構) (Chapter I, Chapter III)	in IEEE Robotics and Automation Letters.	Under Review	
Highly Articulated Tube Mechanism with Variable Stiffness and Shape Restoration Using a Pneumatic Actuator (空圧アクチュエータを使用した柔剛切替と形状復元を備えた関節を有するチューブ機構) (Chapter I, Chapter IV)	in IEEE Robotics and Automation Letter, vol. 7, no. 2, pp. 3664-3671, Apr. 2022.	2022 年 4 月 1 日	
Pneumatic Driven Hollow Variable Stiffness Mechanism Aiming Non-Contact Insertion of Telescopic Guide Tubes (入れ子式ガイドチューブの非接触推進を目指す空圧駆動の中空柔剛切替メカニズム) (Chapter V)	in 2021 IEEE 4th International Conference on Soft Robotics (RoboSoft), Fri5O.1, pp. 615-621, Apr. 2021.	2021 年 4 月 11 日	
参考論文	題 名	公表の方法	公表年月日
			冊数

備 考

- 1 論文題名(博士論文、参考論文)が外国語の場合は、活字体で記入し、日本語の訳文を括弧書きすること。
- 2 論文(博士論文、参考論文)が未公表の場合は、公表予定の方法及び時期を記入すること。
- 3 参考論文については、提出する論文についてのみその題名及び冊数を記入すること。